HOKKAIDO UNIVERSITY

Title	Hydrogenation of Carbon Dioxide over Doped Metal Oxide Catalysts
Author(s)	Shaikh, Nazmul Hasan Mohammad Dostagir
Degree Grantor	北海道大学
Degree Name	博士(理学)
Dissertation Number	甲第14690号
Issue Date	2021-09-24
DOI	https://doi.org/10.14943/doctoral.k14690
Doc URL	https://hdl.handle.net/2115/86888
Type	doctoral thesis
File Information	Dostagir.pdf

Hokkaido University Collection of Scholarly and Academic Papers : HUSCAP

Hydrogenation of Carbon Dioxide over Doped Metal Oxide Catalysts

(ドープ型金属酸化物触媒による二酸化炭素の水素化)

Shaikh Nazmul Hasan Mohammad Dostagir

Hokkaido University

北海道大学

2021

Table of Contents

1. General introduction 1

1.1 Background 1

1.2 CO_2 hydrogenation to methanol and CO 2

1.3 Thermodynamic consideration 4

1.4 Heterogeneous catalysts for CO_2 hydrogenation 5

1.5 Catalyst design 6

1.5.1 CO_2 hydrogenation to methanol 6

1.5.1.1 Cu based catalysts 6

1.5.1.2 Metal oxides as emerging catalysts for CO_2 hydrogenation to methanol 7

1.5.2 Reverse water gas shift reaction 11

1.6 Objective of this work 12

1.7 Outline of the thesis 13

2. Rh promoted In_2O_3 as a highly active catalyst for CO_2 hydrogenation to methanol 21

2.1 Introduction 22

2.2 Experimental method 24

2.2.1 Materials 24

2.2.2 Catalyst preparation 24

2.2.3 Catalyst characterization 25

2.2.4 Evaluation of catalytic activity 27

2.2.5 Equations 28

2.2.6 Theoretical calculations 28

2.3 Results and Discussion 30

2.3.1 Catalytic activity 30

2.3.2 Characterization 32

2.4 Conclusion 41

3. Co single atoms in ZrO_2 with inherent oxygen vacancies for selective hydrogenation of CO_2 to CO 45

3.1 Introduction.....46

3.2 Experimental method.....47

3.2.1 Catalyst Preparation.....47

3.2.2 Catalyst characterization 48

3.2.3 Evaluation of catalytic activity.....50

3.2.4 Theoretical calculations.....50

3.3 Results and discussion 51

3.3.1 Preparation and characterization of doped and impregnated Co catalysts on ZrO_2 51

3.3.2 Modeling the Co doped ZrO_2 surface and its interaction with CO_2 58

3.3.3 Catalytic activity for CO_2 hydrogenation 61

3.3.4 Elucidation of mechanism and active site in doped catalyst 64

3.4 Conclusion 70

4. Role of support in controlling CO_2 hydrogenation pathway.....75

4.1 Introduction.....76

4.2 Experimental method.....77

4.2.1 Catalyst Preparation.....77

4.2.2 Catalyst characterization 78

4.2.3 Evaluation of catalytic activity.....79

4.3 Results and discussions.....79

4.3.1 Catalytic activity.....79

4.3.2 Catalyst structure 81

4.3.3 Surface properties.....82

4.3.4 Mechanistic details 85

4.3.5 Discussion.....89

4.3.6 Significance of interface in impregnated catalysts.....90

4.4 Conclusion 91

5. Conclusion 95

List of Publications 99

Acknowledgement.....101

Chapter 1

General introduction

1.1 Background

The world has seen a massive growth in population and industrial production in the last century. Consequently, the demand for energy has risen exponentially. Fossil fuels have been the main source of energy supporting this growth. As a result, the carbon dioxide (CO_2) released from fossil fuels has been accumulating in the atmosphere. At the starting of 20^{th} century, the concentration of CO_2 in atmosphere was 295 ppm. As of May 2021, this value has increased by 40% to become 414 ppm.[1] The excess anthropogenic CO_2 has a warming effect on the planet. According to Intergovernmental Panel on Climate Change (IPCC), the emission of green-house gases such as CO_2 is the main reason behind global warming.[2] This increase in CO_2 concentration in the atmosphere is already affecting the environment. For example, the increased uptake of CO_2 by oceans is causing their acidification and threatening marine life.[3] It is now high time to adopt drastic measures to prevent a manmade climate catastrophe. Governments around the globe have pledged to reduce the emission of carbon dioxide in the atmosphere. For example, Japan has set up a goal to become carbon neutral until 2050 and achieve a net zero CO_2 emission.[4]

One way to reduce the CO_2 emission is to use CO_2 as a chemical feedstock through a process known as carbon capture and utilization (CCU). Currently, a large part of energy demand is fulfilled by fossil fuels. One of the main sources of energy is gasoline range hydrocarbons, which are derived from fossil fuels. A majority of carbon

based chemicals (for example, benzene, toluene, xylene, methanol, ethylene, propylene) are also derived from fossil fuels. Therefore, use of CO_2 to produce fuels and chemicals would result in a substantial reduction of CO_2 emission from fossil fuels. For example, it has been estimated that if fuels and chemicals were only produced from CO_2 in 2018, almost 14.2 Gt of CO_2 emission could be avoided, which was 42% of total CO_2 emission from the combustion of oil, gas and coal in 2018.[5,6] Hence, production of compounds that are important for chemical industry and in energy sector from CO_2 is highly important.

1.2 CO_2 hydrogenation to methanol and CO

CO_2 can be converted to various industrially important chemicals (Figure 1.1).[7] Among chemicals, urea production is the largest consumer of CO_2. Almost 190 Mt of urea is produced per year utilizing 120 Mt of CO_2.[8] CO_2 is also utilized in the synthesis of formic acid, salicylic acid and carbonate polymers, whose combined production demand is 0.86 Mt per annum.[9,10] However, production of these chemicals cannot help energy sector (for example: use of fossil fuel in industry and transport) to be carbon neutral and brings up additional problems. For example, in case of nitrogen containing fertilizers, they produce N_2O gas, which has 300 time more potential as a greenhouse gas than CO_2.[11] Among the CO_2 derived products, methanol and CO are two of the most important precursors as they are used in both energy sector and in chemical industry.

The global production of methanol is 135 Mt $year^{-1}$.[6] Methanol is largely consumed as formaldehyde, which is used for the production of resins, plastics, paints, pesticides, and pharmaceuticals.[12] Acetic acid produced from carbonylation of methanol is consumed for the production of vinyl acetate. Dimethyl ether (DME) made by dehydration of methanol is used as fuel and fuel blend.[13] Ethylene and propylene, which are the precursors for plastics can be produced via methanol-to-olefins (MTO)

process. Methanol-to-gasoline (MTG) is a process used for producing gasoline range fuels. Aromatics such as benzene-toluene-xylene (BTX) can be obtained from methanol. Another important use of methanol is the storage and transportation of H_2. Moreover, methanol is used in large volume as solvent for various chemical transformations. Therefore, efficient production of methanol from direct CO_2 hydrogenation is of great interest.

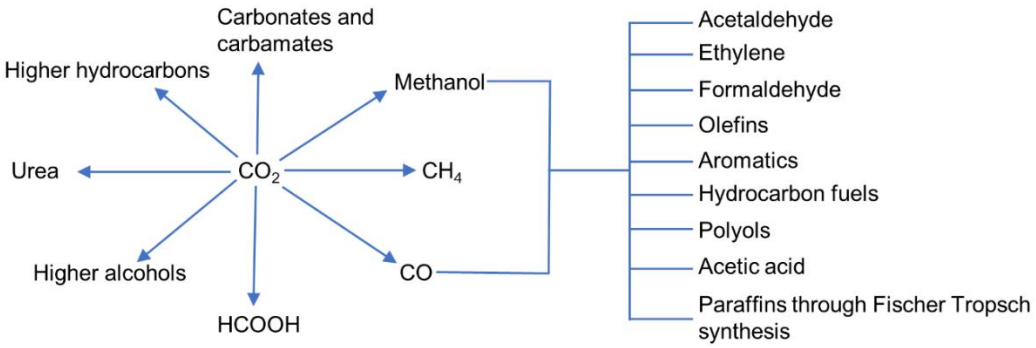

Figure 1.1: Pathways for formation of value-added product directly from CO_2 and through methanol and CO as intermediate precursors.

CO is also a versatile chemical building unit and it can be converted to various important molecules. Syngas, a mixture of CO and H_2, is used to produce fuels and olefins via Fischer-Tropsch synthesis (FTS).[14–16] This process has already been commercialized and is economically viable.[15] Syngas is also used for the production of higher alcohols, which have high applicability as fuels and fuel blender, hydrogen carrier, precursors, and reagents for the production of detergents and plasticizers.[17–19]

Methanol and CO can be used both in the energy sector and in the chemical industry. They are used in the production of liquid fuels, which can decrease the use of fossil fuels. Synthesis of many important fine and bulk chemicals also includes methanol and CO as precursors. In order to produce all those industrially important

products directly from CO_2, methanol and/or CO need to be synthesized from CO_2 as the initial product. Therefore, it is important to study CO_2 hydrogenation to methanol and CO.

1.3 Thermodynamic consideration

Thermodynamic stability of CO_2 is high owing to the highest oxidation state of carbon in CO_2. Figure 1.2 shows the Gibbs free energy of formation of CO_2 and products derived from CO_2 hydrogenation. All products are less stable than CO_2. This means that a substantial amount of energy is required for the CO_2 hydrogenation reaction. This is why, in thermochemical process, elevated temperature is helpful for CO_2 conversion.

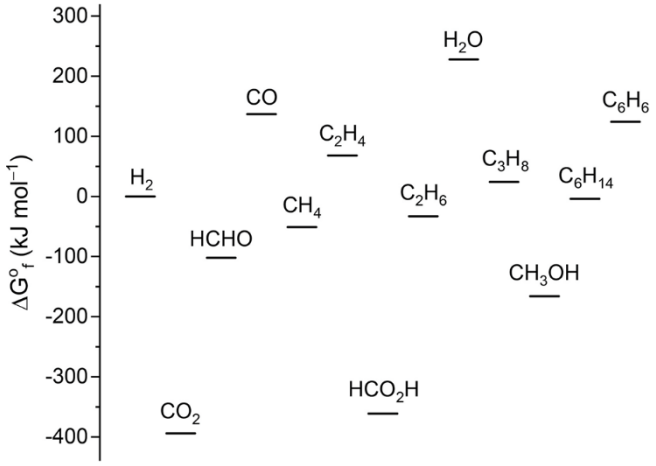

Figure 1.2: Plot showing Gibbs free energy for formation for CO_2 and chemicals derived from its hydrogenation. Reprinted with permission form ref. (6). Copyright 2020 American Chemical Society.

CO production from CO_2, known as reverse water gas shift (RWGS) reaction (Equation 1.1), is endothermic while methanol and methane formation (Equation 1.2 and 1.3 respectively) are exothermic in nature.[20] This means that RWGS reaction is favored at higher temperature while methanol and methane formation are favored at lower temperature. In addition, higher pressure tends to favor the formation of methanol

and methane while change in pressure should not have any influence over the RWGS reaction.

$$CO_2 + H_2 \Leftrightarrow CO + H_2O \qquad \Delta H^{\circ}_{298K} = +41.2\ kJ\ mol^{-1} \quad (1.1)$$

$$CO_2 + 3H_2 \Leftrightarrow CH_3OH + H_2O \qquad \Delta H^{\circ}_{298K} = -49.5\ kJ\ mol^{-1} \quad (1.2)$$

$$CO_2 + 4H_2 \Leftrightarrow CH_4 + 2H_2O \qquad \Delta H^{\circ}_{298K} = -165.0\ kJ\ mol^{-1} \quad (1.3)$$

1.4 Heterogeneous catalysts for CO_2 hydrogenation

The high stability of CO_2 poses a challenge for its conversion to other products. Therefore, catalysts are required to lower the activation barrier for its hydrogenation. Several homogeneous catalysts such as transition metal complexes, frustrated Lewis acid-base pairs (FLPs), or N-heterocyclic carbenes (NHCs) show decent activity at mild reaction condition.[21–24] However, homogeneous catalysts are not suitable for production of chemicals in large volume due to the difficulties in their separation from reaction mixture and poor process economy. Therefore, research focus has been turned towards heterogeneous catalysts.

Heterogeneous catalysts can be applied for CO_2 conversion using electrochemical, photochemical and thermochemical processes.[6,16,25–30] In photochemical process, the efficiency is much lower than the current industrial demand. For electrochemical conversion, H_2 can be obtained directly from water, eliminating the requirement of external H_2 gas. However, the faradic efficiency is not sufficient for industrial scale application at present.[6] Thermochemical CO_2 reduction process has the potential for industrial application and is common in practice. Although from an environmental point of view, successful implementation of this technology would require H_2 from renewable sources, which would increase the cost of production, thermochemical conversions can still be economically viable. One such representative example is the "George Olah Renewable Methanol Plant" in Iceland.[31] H_2 required for

CO_2 hydrogenation to methanol is obtained by electrolysis of water. The energy to run both the water electrolysis and CO_2 hydrogenation systems comes from the local geothermal energy sources. This is the first plant for direct recycling of CO_2 to methanol converting ~5600 tons of CO_2 to methanol yearly.

1.5 Catalyst design

The pathway of CO_2 hydrogenation to C1 products (Scheme 1.1) is complicated because the desired products can undergo further hydrogenation. Therefore, controlling selectivity of a single product is the main concern in CO_2 hydrogenation reaction. Accordingly, design of a highly selective, stable, active, and inexpensive catalyst is important.

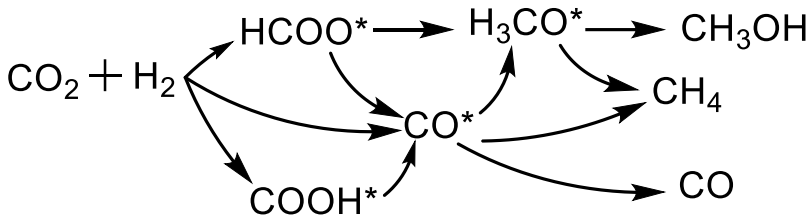

Scheme 1.1: Schematic representation of CO_2 hydrogenation pathway to C1 products.

1.5.1 CO_2 hydrogenation to methanol

1.5.1.1 Cu based catalysts

Since 1960s, after the discovery of Cu-ZnO catalyst for methanol production from syngas by Imperial Chemical Industries (ICI), Cu based catalysts were extensively studied for CO_2 hydrogenation to methanol.[6,32,33] The activity and selectivity of CO_2 hydrogenation to methanol over Cu based systems were found to be dependent on catalyst structure and nature of support. The good performance of current industrial catalyst, Cu-ZnO-Al_2O_3, was due to high dispersion of Cu species on ZnO and stability was enhanced by using Al_2O_3 as support.[6] It was suggested that the presence of stepped sites at the Cu surface was helpful for high activity and presence of $Zn^{\delta+}$ near the defect enhanced the stability of formate species.[34,35] As a result, methanol formation improved

via further hydrogenation of formate species. Kattel et al. showed that ZnCu bimetallic alloy underwent oxidation to form ZnO-Cu interfaces, which promoted the formate formation and subsequent formation of methanol.[36] Introduction of other oxides also improved the activity of Cu based systems.[6,29,37] ZrO_2 increased the stability of highly dispersed Cu species and helped to improve the activity by stabilizing intermediates at the interfacial sites.[38–40]

Although Cu based catalytic systems are inexpensive, they have several problems regarding stability, activity, and selectivity of CO_2 hydrogenation to methanol. When applied for direct CO_2 hydrogenation to methanol, competitive RWGS reaction also occurs and decreases methanol selectivity. Furthermore, in a CO_2 rich feed, the Cu-ZnO-Al_2O_3 catalyst deactivates rapidly.[41–43] Water, formed as a byproduct of CO_2 hydrogenation reaction, promotes sintering of Cu and reduces activity.[43–45] Huang et al. reported 34% activity loss of Cu-ZnO-Al_2O_3 catalyst after 720 h on stream due to oxidation of Cu^0 to Cu^{2+} and agglomeration of ZnO.[46] In addition, high coverage of the adsorbed species (for example: carbonates and formate) on the catalyst surface also slowed down the reaction at high CO_2 concentration.[47–51] In Cu/ZrO_2 and Cu/TiO_2 catalysts, the active sites were poisoned by the over stabilization of formate species.[52] Consequently, the mechanism for methanol formation gradually changes from formate mechanism to RWGS and CO hydrogenation mechanism. Therefore, while Cu based catalysts are commercially used for syngas conversion, their application for direct hydrogenation of CO_2 rich feed is not yet feasible.

1.5.1.2 Metal oxides as emerging catalysts for CO_2 hydrogenation to methanol

Recently, indium oxide (In_2O_3) was discovered as a stable and selective catalyst for direct CO_2 hydrogenation to methanol.[53] Since then, the research focus has shifted towards use of metal oxide based catalytic systems. The superiority of In_2O_3 is largely

attributed to the oxygen vacancies present on the surface that act as active sites for CO_2 adsorption.[54–58] In_2O_3 is a reducible oxide and oxygen vacancies can form on its surface by partial reduction under hydrogen atmosphere. Although oxygen vacancies on the reducible oxides were known to promote CO_2 hydrogenation, its ability to selectively hydrogenate CO_2 to methanol was not realized. Figure 1.3 shows the mechanism of methanol formation on the surface of In_2O_3.[54] Oxygen vacancy present on the surface can strongly adsorb CO_2. Heterolytic hydrogen dissociation happens over the neighboring partially reduced indium atoms forming In-H and In-O-H species. Transfer of hydride from indium to carbon of CO_2 produces formate species. Subsequent hydrogen dissociation and addition to carbon of formate species produces methanol and replenishes the oxygen defect. Further hydrogenation regenerates the active oxygen vacancy to complete the cycle. The main advantage of In_2O_3 catalyst is that it can suppress the competing RWGS reaction resulting in high selectivity of methanol. The formation of COOH (carboxyl) species (intermediate of RWGS reaction over In_2O_3 catalyst) from CO_2 and H_2 is endothermic and experiences a high energy barrier. In contrast, the formation of formate species (intermediate of methanol) is exothermic and experiences a low energy barrier.[54,58,59]

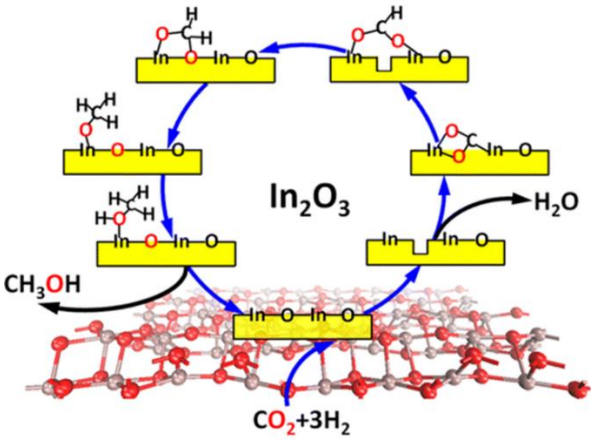

Figure 1.3: Mechanism of methanol formation over the surface of In_2O_3 during direct CO_2 hydrogenation. Reprinted with permission form ref. (54). Copyright 2013 American Chemical Society.

In 2015, first experimental work showcased the methanol formation over commercial In_2O_3 catalysts with a methanol selectivity of 55%.[60] Following year, Ramirez et al. demonstrated that controlled synthesis of In_2O_3 having high density of oxygen vacancy showed 100% methanol selectivity.[53] However, the activity of pure In_2O_3 was low and these seminal works were followed by extensive research to promote the activity. When In_2O_3 was supported over monoclinic ZrO_2, stability and activity were increased (Figure 1.4a).[53] The activity and stability of In_2O_3/ZrO_2 were better as compared to the commercial Cu-ZnO-Al_2O_3 (Figure 1.4b).[53] The influence of ZrO_2 was attributed to promotion of oxygen vacancy formation over In_2O_3 surface because of crystal mismatch between cubic In_2O_3 and ZrO_2. In addition, formation of solid solution between indium and zirconium and electronic transition from ZrO_2 to In_2O_3 were also reported a probable cause.[61–63] In a different work, when In_2O_3 was supported over Co metal, charge transfer from Co metal to In_2O_3 also led to creation of more oxygen vacancy and improved hydrogen dissociation over Co resulted in higher methanol productivity.[64]

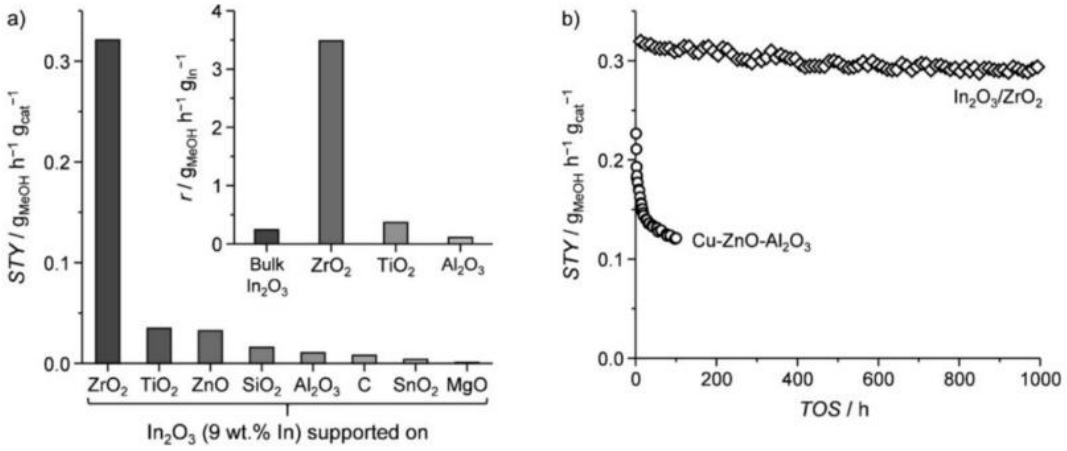

Figure 1.4: (a) Promotion of In_2O_3 by supporting it over different metal oxides. (b) Comparison of In_2O_3/ZrO_2 with commercial Cu-ZnO-Al_2O_3. Reproduced with permission from ref. (53). Copyright 2016 John Wiley and Sons.

Another strategy to promote the activity of In_2O_3 is the addition of noble metals. Rui et al. showed that having small Pd clusters on In_2O_3 can improve methanol productivity (Space time yield (STY) = 0.89 g_{MeOH} h^{-1} g_{cat}^{-1}).[65] Synergy between In_3Pd_2 and In_2O_3 phase was helpful to enhance the methanol formation.[66] Ramirez et al. showed that Pd clusters having nuclearity higher than 4 resulted an increase in the competing RWGS reaction and formation of intermetallic $Pd_2In_2O_4$ and $Pd_3In_2O_4$ clusters greatly improved the methanol formation (STY = 1.0 g_{MeOH} h^{-1} g_{cat}^{-1}).[67] Similarly, in presence of bimetallic RhIn and $RhIn_3$ alloy nanoparticles, formed by the decoration of reduced indium species over Rh metal, formate formation was enhanced.[68] As a result, methanol productivity increased (STY = 1.0 g_{MeOH} h^{-1} g_{cat}^{-1}). Although In_2O_3 offers good selectivity and stability, its cost is an issue in commercial application. Therefore, the search is still going on to find an inexpensive, selective, and active catalyst to replace the Cu-ZnO-Al_2O_3 catalyst used in industry.

Other metal oxide based catalysts have also emerged as a replacement of In_2O_3. Li et al. showed that a solid solution of ZnO-ZrO_2 can produce methanol from CO_2 hydrogenation with selectivity of 86-91% and an STY of 0.7 g_{MeOH} h^{-1} g_{cat}^{-1}.[69] It is worth mentioning that pure ZnO and ZrO_2 did not show any activity. The formation of solid solution produced oxygen vacancy on the surface, which increased CO_2 adsorption and stabilized formate species for subsequent hydrogenation to methanol.[69,70] In their next work, they investigated a series of solid solution catalysts and found out that CdO-ZrO_2 and Ga_2O_3-ZrO_2 catalysts also have high activity.[71] CdO-ZrO_2 showed a high STY of 0.85 g_{MeOH} h^{-1} g_{cat}^{-1} with methanol selectivity of 80%. In

these doped ZrO_2 catalysts, the interfacial site between Zn/Cd/Ga and neighboring Zr atom is the active site. While Zn/Cd/Ga helps in hydrogen dissociation, neighboring Zr atoms help to stabilize the formate intermediate and make it susceptible for further hydrogenation to methanol. Similarly, a combination of MnO_x and Co_3O_4 was helpful for methanol production under milder condition.[72] The interface of cobalt oxide and manganese oxide was suggested as the active site.

1.5.2 Reverse water gas shift reaction

Contrary to methanol formation, the RWGS reaction is endothermic in nature and is favored at higher temperatures. Moreover, as shown in scheme 1.1, CO can be intermediate for formation of methanol and methane. Therefore, the main challenge in RWGS reaction is to achieve high selectivity of CO by avoiding its further hydrogenation, especially at high CO_2 conversion. CO selectivity can be increased by tuning the adsorption strength of CO on the catalyst to facilitate its desorption without further hydrogenation. Careful design of catalyst to reduce CO adsorption without influencing CO_2 hydrogenation ability is necessary to maximize CO yield. One strategy is to alter the crystal structure of support to influence the electronic charge on supported metals. In Ru/TiO_2 catalysts, changing the support from rutile TiO_2 to anatase TiO_2 allowed electron transfer from Ru to support and resulted in formation of oxidized Ru species. This weakened the interaction of CO with Ru and decreased the chance of further CO hydrogenation.[73] Similar effect was observed on Ir/CeO_2, where due to strong metal-support interaction, partially oxidized Ir species were formed that were less capable of CO adsorption and its further hydrogenation.[74] Shielding the metal by creating an overlayer of support also reduced CO adsorption on metals. Forming an overlayer of reduced TiO_x over Ir particles in a Ir/TiO_2 catalyst weakened the adsorption of CO and improved CO selectivity.[75] In a PtCo/support catalyst system, changing the

support from TiO_2 to CeO_2 or ZrO_2 increased the adsorption of intermediates such as formate and methoxy at the interface and the selectivity of CH_4 increased because of total hydrogenation of the adsorbed species.[76] Therefore, tuning the adsorption of intermediates and CO is one of the key factors for achieving high CO selectivity in RWGS reaction.

Size of metal particles in a catalyst also has a significant influence on the selectivity of CO during CO_2 hydrogenation.[77–80] Large metal particles strongly adsorb CO on their surface. On large particles, the backdonation of electron from metal atoms to CO increases and as a result interaction of CO with metals becomes stronger. Consequently, hydrogenation of CO becomes easier to yield CH_4 as the primary product. In contrast, smaller metal particles interact weakly with CO, which promotes its desorption and increases selectivity. This effect is most pronounced in the presence of single atom catalysts (SAC). Chirstopher et al. showed that high CO selectivity was achieved over isolated Rh atoms due to facile desorption of CO from single atom.[81] In addition, SACs lack high density of dissociatively adsorbed hydrogen species present on nanoparticle surface and are only able to perform $2e^-$ redox cycle of CO_2 to CO.[82] However, the isolation of metal atoms is not the only factor and the interface of single metal atoms with oxide support also plays a crucial role in determining product selectivity. For example, in a Ru/CeO_2 single atom catalyst, CO was stabilized at the interface and methane was produced by its successive hydrogenation.[83] Therefore, better strategy is required for designing catalysts for RWGS reaction.

1.6 Objective of this work

In CO_2 hydrogenation, methanol and CO are the target products because methane is also thermodynamically stable and its upgradation is difficult. The main challenge in

producing methanol and CO is to obtain a single product stream with high selectivity in order to maximize the yield and avoid byproduct formation.

Specific to methanol synthesis, it is important to obtain high productivity for the process to be economical and scalable. Moreover, the catalyst should be stable for long term operation. With respect to CO synthesis, avoiding the subsequent hydrogenation of CO to methane and maintaining a high CO_2 conversion is required.

The overall objective of this thesis is to develop highly active and selective catalysts for CO_2 hydrogenation, while exploring the parameters and the underlying factors that influence the product selectivity. From the perspective of catalyst design, it is clear that conventional supported metal catalysts are not effective for selective CO_2 hydrogenation to methanol and CO. Oxide catalysts with interfacial sites are able to activate CO_2 and influence product selectivity. With that in mind, this thesis aims at designing metal oxide catalysts doped with transition metals for CO_2 hydrogenation. In doped oxides, dopant metal atoms are dispersed throughout the crystal matrix of the support oxide, which is expected to increase the stability of the dopants. In addition to investigating the activity of doped metal oxide catalysts, this thesis also focuses on understanding the contribution of support metal oxide in controlling the CO_2 hydrogenation selectivity and reaction pathway at the interfacial site.

1.7 Outline of the thesis

This thesis starts with a focus on the development of highly active In_2O_3 based catalysts for CO_2 hydrogenation to methanol (Chapter 2). While pure In_2O_3 shows high selectivity to methanol the productivity is low owing to poor CO_2 conversion. My strategy to overcome this issue was to incorporate transition metals in In_2O_3 structure. Among several transition metals tested, Rh showed the highest promotional effect. Thorough characterization was carried out to understand the nature of the active site

and the promotional effect of Rh atom. It was found that In_2O_3 catalyst having atomically dispersed Rh showed high methanol productivity without reducing the methanol selectivity. Rh single atom at the oxygen vacant site (Rh-V_o-In, V_o = oxygen vacancy) promoted the formation of formate intermediate. The formate readily hydrogenated to methanol with very high productivity. The interface between Rh and partially reduced In atoms stabilized the formate intermediate and further hydrogenation of formate by Rh atoms increased the methanol productivity.

In chapter 3, I used the strategy of oxygen vacancy formation near single metal atom for CO_2 activation to obtain CO as the primary product. By using a Co doped ZrO_2 catalyst oxygen vacancies were created near Co atoms through a mismatch of charge between cations. Using this catalyst, high selectivity of CO was achieved during CO_2 hydrogenation. The oxygen vacancy was helpful to increase CO_2 chemisorption. The interfacial site between Co and neighboring Zr atom were responsible to stabilize the formate intermediate, which then decomposed to CO selectively instead of undergoing further hydrogenation to produce methanol. The strong adsorption of CO_2 as compared to CO at the oxygen vacant interface helped in desorption of CO and prevented its further hydrogenation to CH_4. As a result, methane formation was suppressed and high CO selectivity (>95%) was achieved. The interfacial site between Co and Zr was the active site for the stabilization of formate intermediate and its conversion to CO.

Based on the results of chapters 2 and 3, it was clear that while the metal catalyst played a pivotal role in the reaction, the interface created by its interaction with support was crucial to determine product selectivity. To investigate the support effect over indium based catalyst, two different metal oxides doped with indium (In-ZrO_2 and In-TiO_2) were prepared and investigated for CO_2 hydrogenation (Chapter 4). I found that support has substantial influence on CO_2 hydrogenation mechanism and product

selectivity. The reducibility of support was one of the key factors. In-TiO_2 followed redox mechanism because of the high reducibility of TiO_2 and as a result, CO was produced. In contrast, due to the non-reducible nature of ZrO_2, In-ZrO_2 followed formate mechanism to produce methanol as the major product.

At the end, this work is summarized in Chapter 5 to draw insights on the role of interfacial sites for CO_2 hydrogenation to methanol and CO. My comments on the outlook and future research direction in this field are also added.

References

1. Mauna Lao Lab, Global Monitoring Laboratory - Carbon Cycle Greenhouse Gases, https://gml.noaa.gov/ccgg/trends/gl_trend.html, (accessed May 2021).
2. Global Warming of 1.5 ºC, https://www.ipcc.ch/sr15/, (accessed May 2021).
3. Ocean acidification, National Oceanic and Atmospheric Administration, https://www.noaa.gov/education/resource-collections/ocean-coasts/ocean-acidification, (accessed May 2021).
4. Japan's 2050 Carbon Neutral Goal, METI Ministry of Economy, Trade and Industry, https://www.meti.go.jp/english/policy/energy_environment/global_warming/roadmap/report/20201111.html, (accessed May 2021).
5. Petrolium, B. BP Statistical Review of World Energy Report, BP: London, U.K. 2019.
6. S. De, A. Dokania, A. Ramirez and J. Gascon, *ACS Catal.*, 2020, **10**, 14147–14185.
7. W. Li, H. Wang, X. Jiang, J. Zhu, Z. Liu, X. Guo and C. Song, *RSC Adv.*, 2018, **8**, 7651–7669.
8. S. M. Jarvis and S. Samsatli, *Renew. Sustain. Energy Rev.*, 2018, **85**, 46–68.
9. E. Alper and O. Yuksel Orhan, *Petroleum*, 2017, **3**, 109–126.
10. S. Ye, S. Wang, L. Lin, M. Xiao and Y. Meng, *Adv. Ind. Eng. Polym. Res.*, 2019, **2**, 143–160.
11. C. Hepburn, E. Adlen, J. Beddington, E. A. Carter, S. Fuss, N. Mac Dowell, J. C. Minx, P. Smith and C. K. Williams, *Nature*, 2019, **575**, 87–97.
12. M. Bertau, H. Offermanns, L. Plass, F. Schmidt and H. J. Wernicke, *Methanol: The basic chemical and energy feedstock of the future: Asinger's vision today*, Springer, Heidelberg, 2014.
13. T. A. Semelsberger, R. L. Borup and H. L. Greene, *J. Power Sources*, 2006, **156**, 497–511.
14. J. R. Regalbuto, *Science*, 2009, **325**, 822–824.

15. J. Bao, G. Yang, Y. Yoneyama and N. Tsubaki, *ACS Catal.*, 2019, **9**, 3026–3053.
16. F. Jiao, J. Li, X. Pan, J. Xiao, H. Li, H. Ma, M. Wei, Y. Pan, Z. Zhou, M. Li, S. Miao, J. Li, Y. Zhu, D. Xiao, T. He, J. Yang, F. Qi, Q. Fu and X. Bao, *Science*, 2016, **351**, 1065–1068.
17. J. J. Spivey and A. Egbebi, *Chem. Soc. Rev.*, 2007, **36**, 1514–1528.
18. X. Pan, Z. Fan, W. Chen, Y. Ding, H. Luo and X. Bao, *Nat. Mater.*, 2007, **6**, 507–511.
19. M. Gupta, M. L. Smith and J. J. Spivey, *ACS Catal.*, 2011, **1**, 641–656.
20. C. Jia, J. Gao, Y. Dai, J. Zhang and Y. Yang, *J. Energy Chem.*, 2016, **25**, 1027–1037.
21. S. Kar, J. Kothandaraman, A. Goeppert and G. K. S. Prakash, *J. CO_2 Util.*, 2018, **23**, 212–218.
22. N. Onishi, G. Laurenczy, M. Beller and Y. Himeda, *Coord. Chem. Rev.*, 2018, **373**, 317–332.
23. K. A. Grice, *Coord. Chem. Rev.*, 2017, **336**, 78–95.
24. K. Sordakis, C. Tang, L. K. Vogt, H. Junge, P. J. Dyson, M. Beller and G. Laurenczy, *Chem. Rev.*, 2018, **118**, 372–433.
25. D. Li, M. Kassymova, X. Cai, S. Q. Zang and H. L. Jiang, *Coord. Chem. Rev.*, 2020, **412**, 213262.
26. S. Yu, A. J. Wilson, G. Kumari, X. Zhang and P. K. Jain, *ACS Energy Lett.*, 2017, **2**, 2058–2070.
27. F. Y. Gao, R. C. Bao, M. R. Gao and S. H. Yu, *J. Mater. Chem. A*, 2020, **8**, 15458–15478.
28. S. Nitopi, E. Bertheussen, S. B. Scott, X. Liu, A. K. Engstfeld, S. Horch, B. Seger, I. E. L. Stephens, K. Chan, C. Hahn, J. K. Nørskov, T. F. Jaramillo and I. Chorkendorff, *Chem. Rev.*, 2019, **119**, 7610–7672.
29. E. C. Ra, K. Y. Kim, E. H. Kim, H. Lee, K. An and J. S. Lee, *ACS Catal.*, 2020, **10**, 11318–11345.
30. A. Álvarez, A. Bansode, A. Urakawa, A. V. Bavykina, T. A. Wezendonk, M. Makkee, J. Gascon and F. Kapteijn, *Chem. Rev.*, 2017, **117**, 9804–9838.
31. A. Goeppert, M. Czaun, J. P. Jones, G. K. Surya Prakash and G. A. Olah, *Chem. Soc. Rev.*, 2014, **43**, 7995–8048.
32. K. C. Waugh, *Catal. Today*, 1992, **15**, 51–75.
33. I. U. Din, M. S. Shaharun, M. A. Alotaibi, A. I. Alharthi and A. Naeem, *J. CO_2 Util.*, 2019, **34**, 20–33.
34. M. Behrens, F. Studt, I. Kasatkin, S. Kühl, M. Hävecker, F. Abild-Pedersen, S. Zander, F. Girgsdies, P. Kurr, B. L. Kniep, M. Tovar, R. W. Fischer, J. K. Nørskov and R. Schlögl, *Science*, 2012, **336**, 893–897.

35. S. Kuld, M. Thorhauge, H. Falsig, C. F. Elkjær, S. Helveg, I. Chorkendorff and J. Sehested, *Science*, 2016, **352**, 969–974.
36. S. Kattel, P. J. Ramírez, J. G. Chen, J. A. Rodriguez and P. Liu, *Science*, 2017, **355**, 1296–1299.
37. X. Jiang, X. Nie, X. Guo, C. Song and J. G. Chen, *Chem. Rev.*, 2020, **120**, 7984–8034.
38. K. Larmier, W. C. Liao, S. Tada, E. Lam, R. Verel, A. Bansode, A. Urakawa, A. Comas-Vives and C. Copéret, *Angew. Chemie Int. Ed.*, 2017, **56**, 2318–2323.
39. X. Fang, Y. Men, F. Wu, Q. Zhao, R. Singh, P. Xiao, T. Du and P. A. Webley, *J. CO_2 Util.*, 2019, **29**, 57–64.
40. S. Tada, S. Kayamori, T. Honma, H. Kamei, A. Nariyuki, K. Kon, T. Toyao, K. I. Shimizu and S. Satokawa, *ACS Catal.*, 2018, **8**, 7809–7819.
41. K. Klier, V. Chatikavanij, R. G. Herman and G. W. Simmons, *J. Catal.*, 1982, **74**, 343–360.
42. C. J. Schack, M. A. McNeil and R. G. Rinker, *Appl. Catal.*, 1989, **50**, 247–263.
43. M. Sahibzada, I. S. Metcalfe and D. Chadwick, *J. Catal.*, 1998, **174**, 111–118.
44. O. Martin and J. Pérez-Ramírez, *Catal. Sci. Technol.*, 2013, **3**, 3343–3352.
45. J. Wu, M. Saito, M. Takeuchi and T. Watanabe, *Appl. Catal. A Gen.*, 2001, **218**, 235–240.
46. B. Liang, J. Ma, X. Su, C. Yang, H. Duan, H. Zhou, S. Deng, L. Li and Y. Huang, *Ind. Eng. Chem. Res.*, 2019, **58**, 9030–9037.
47. F. Studt, M. Behrens, E. L. Kunkes, N. Thomas, S. Zander, A. Tarasov, J. Schumann, E. Frei, J. B. Varley, F. Abild-Pedersen, J. K. Nørskov and R. Schlögl, *ChemCatChem*, 2015, **7**, 1105–1111.
48. Y. Yang, C. A. Mims, D. H. Mei, C. H. F. Peden and C. T. Campbell, *J. Catal.*, 2013, **298**, 10–17.
49. T. S. Askgaard, J. K. Nørskov, C. V. Ovesen and P. Stoltze, *J. Catal.*, 1995, **156**, 229–242.
50. Q. Sun, C. W. Liu, W. Pan, Q. M. Zhu and J. F. Deng, *Appl. Catal. A Gen.*, 1998, **171**, 301–308.
51. L. C. Grabow and M. Mavrikakis, *ACS Catal.*, 2011, **1**, 365–384.
52. S. Kattel, B. Yan, Y. Yang, J. G. Chen and P. Liu, *J. Am. Chem. Soc.*, 2016, **138**, 12440–12450.
53. O. Martin, A. J. Martín, C. Mondelli, S. Mitchell, T. F. Segawa, R. Hauert, C. Drouilly, D. Curulla-Ferré and J. Pérez-Ramírez, *Angew. Chemie Int. Ed.*, 2016, **55**, 6261–6265.
54. J. Ye, C. Liu, D. Mei and Q. Ge, *ACS Catal.*, 2013, **3**, 1296–1306.
55. M. S. Frei, M. Capdevila-Cortada, R. García-Muelas, C. Mondelli, N. López, J. A. Stewart, D. Curulla Ferré and J. Pérez-Ramírez, *J. Catal.*, 2018, **361**, 313–321.

56. M. Dou, M. Zhang, Y. Chen and Y. Yu, *Comput. Theor. Chem.*, 2018, **1126**, 7–15.
57. S. Dang, B. Qin, Y. Yang, H. Wang, J. Cai, Y. Han, S. Li, P. Gao and Y. Sun, *Sci. Adv.*, 2020, **6**, 2060–2077.
58. J. Wang, G. Zhang, J. Zhu, X. Zhang, F. Ding, A. Zhang, X. Guo and C. Song, *ACS Catal.*, 2021, **11**, 1406–1423.
59. J. Ye, C. Liu and Q. Ge, *J. Phys. Chem. C*, 2012, **116**, 7817–7825.
60. K. Sun, Z. Fan, J. Ye, J. Yan, Q. Ge, Y. Li, W. He, W. Yang and C. J. Liu, *J. CO_2 Util.*, 2015, **12**, 1–6.
61. M. S. Frei, C. Mondelli, A. Cesarini, F. Krumeich, R. Hauert, J. A. Stewart, D. Curulla Ferré and J. Pérez-Ramírez, *ACS Catal.*, 2020, **10**, 1133–1145.
62. A. Tsoukalou, P. M. Abdala, A. Armutlulu, E. Willinger, A. Fedorov and C. R. Müller, *ACS Catal.*, 2020, **10**, 10060–10067.
63. C. Yang, C. Pei, R. Luo, S. Liu, Y. Wang, Z. Wang, Z. J. Zhao and J. Gong, *J. Am. Chem. Soc.*, 2020, **142**, 19523–19531.
64. A. Bavykina, I. Yarulina, A. J. Al Abdulghani, L. Gevers, M. N. Hedhili, X. Miao, A. R. Galilea, A. Pustovarenko, A. Dikhtiarenko, A. Cadiau, A. Aguilar-Tapia, J.-L. Hazemann, S. M. Kozlov, S. Oud-Chikh, L. Cavallo and J. Gascon, *ACS Catal.*, 2019, **9**, 6910–6918.
65. N. Rui, Z. Wang, K. Sun, J. Ye, Q. Ge and C. jun Liu, *Appl. Catal. B Environ.*, 2017, **218**, 488–497.
66. J. L. Snider, V. Streibel, M. A. Hubert, T. S. Choksi, E. Valle, D. C. Upham, J. Schumann, M. S. Duyar, A. Gallo, F. Abild-Pedersen and T. F. Jaramillo, *ACS Catal.*, 2019, **9**, 3399–3412.
67. M. S. Frei, C. Mondelli, R. García-Muelas, K. S. Kley, B. Puértolas, N. López, O. V. Safonova, J. A. Stewart, D. Curulla Ferré and J. Pérez-Ramírez, *Nat. Commun.*, 2019, **10**, 1–11.
68. M. M. J. Li, H. Zou, J. Zheng, T. S. Wu, T. S. Chan, Y. L. Soo, X. P. Wu, X. Q. Gong, T. Chen, K. Roy, G. Held and S. C. E. Tsang, *Angew. Chemie Int. Ed.*, 2020, **59**, 16039–16046.
69. J. Wang, G. Li, Z. Li, C. Tang, Z. Feng, H. An, H. Liu, T. Liu and C. Li, *Sci. Adv.*, 2017, **3**, 1–11.
70. S. Zhou and S. Li, *J. Phys. Chem. C*, 2020, **124**, 27467–27478.
71. J. Wang, C. Tang, G. Li, Z. Han, Z. Li, H. Liu, F. Cheng and C. Li, *ACS Catal.*, 2019, **9**, 10253–10259.
72. C. S. Li, G. Melaet, W. T. Ralston, K. An, C. Brooks, Y. Ye, Y. S. Liu, J. Zhu, J. Guo, S. Alayoglu and G. A. Somorjai, *Nat. Commun.*, 2015, **6**, 1–5.

73. X. Li, J. Lin, L. Li, Y. Huang, X. Pan, S. E. Collins, Y. Ren, Y. Su, L. Kang, X. Liu, Y. Zhou, H. Wang, A. Wang, B. Qiao, X. Wang and T. Zhang, *Angew. Chemie Int. Ed.*, 2020, **59**, 19983–19989.
74. S. Li, Y. Xu, Y. Chen, W. Li, L. Lin, M. Li, Y. Deng, X. Wang, B. Ge, C. Yang, S. Yao, J. Xie, Y. Li, X. Liu and D. Ma, *Angew. Chemie Int. Ed.*, 2017, **56**, 10761–10765.
75. Y. Zhang, Z. Zhang, X. Yang, R. Wang, H. Duan, Z. Shen, L. Li, Y. Su, R. Yang, Y. Zhang, X. Su, Y. Huang and T. Zhang, *Green Chem.*, 2020, **22**, 6855–6861.
76. S. Kattel, W. Yu, X. Yang, B. Yan, Y. Huang, W. Wan, P. Liu and J. G. Chen, *Angew. Chemie Int. Ed.*, 2016, **55**, 7968–7973.
77. A. Wang, J. Li and T. Zhang, *Nat. Rev. Chem.*, 2018, **2**, 65–81.
78. J. H. Kwak, L. Kovarik and J. Szanyi, *ACS Catal.*, 2013, **3**, 2449–2455.
79. J. H. Kwak, L. Kovarik and J. Szanyi, *ACS Catal.*, 2013, **3**, 2094–2100.
80. H. C. Wu, Y. C. Chang, J. H. Wu, J. H. Lin, I. K. Lin and C. S. Chen, *Catal. Sci. Technol.*, 2015, **5**, 4154–4163.
81. J. C. Matsubu, V. N. Yang and P. Christopher, *J. Am. Chem. Soc.*, 2015, **137**, 3076–3084.
82. M. M. Millet, G. Algara-Siller, S. Wrabetz, A. Mazheika, F. Girgsdies, D. Teschner, F. Seitz, A. Tarasov, S. V. Levchenko, R. Schlögl and E. Frei, *J. Am. Chem. Soc.*, 2019, **141**, 2451-2461.
83. Y. Guo, S. Mei, K. Yuan, D. J. Wang, H. C. Liu, C. H. Yan and Y. W. Zhang, *ACS Catal.*, 2018, **8**, 6203–6215.

Chapter 2

Rh promoted In_2O_3 as a highly active catalyst for CO_2 hydrogenation to methanol

Abstract

In search for a selective and stable catalytic system for CO_2 hydrogenation to methanol, In_2O_3 has emerged as a promising alternative to the current industrial catalyst, Cu-ZnO/Al_2O_3. However, the methanol productivity over pure In_2O_3 is low due to poor CO_2 conversion. This chapter focuses on promoting the activity of In_2O_3 to maximize methanol productivity. To increase the activity of In_2O_3, it was doped with transition metals from group 8, 9 and 10 of the periodic table. Among all the dopants used, Rh was found to be the most effective to increase the methanol productivity without altering the methanol selectivity. Rh doped catalyst showed a high space time yield (STY) of methanol of 1.0 $g_{MeOH}\ h^{-1}\ g_{cat}^{-1}$. Characterization showed that Rh atoms were atomically dispersed in the In_2O_3 crystal. Under reaction conditions, Rh atoms were stabilized through the electronic charge transfer from neighboring partially reduced In atoms, which increased the stability of catalyst. Under reaction condition, Rh atoms formed high density of oxygen vacancy near it and promoted the strong CO_2 chemisorption. The adsorbed CO_2 was hydrogenated to formate species that were intermediate for methanol formation.

2.1 Introduction

Among the valorization techniques of CO_2, direct CO_2 hydrogenation to methanol is attractive because methanol is produced in large quantities and is used as solvent and precursor to produce many bulk chemicals industrially.[1] In this process, exothermic methanol production (Equation 1.2) is accompanied by endothermic reverse water gas shift reaction (RWGS) (Equation 1.1).[1] The current industrial catalyst, Cu-ZnO/Al_2O_3, produces methanol from syngas (CO + H_2) containing small amount of CO_2 and deactivates rapidly in presence water formed as a byproduct.[2] Therefore, development of highly active, stable, and selective catalyst for direct CO_2 hydrogenation to methanol is important.

In search for a stable and selective catalyst, In_2O_3 has emerged as a promising alternative. In_2O_3 surface can promote methanol formation while suppressing RWGS reaction. Oxygen vacancy along with neighboring indium atoms over In_2O_3 surface was suggested as the active site for methanol production.[3] Oxygen vacancy can activate CO_2 while neighboring indium atoms can perform heterolytic hydrogen dissociation and hydrogenation of CO_2 to form formate species. Successive hydrogenation of formate then produces methanol. Methanol selectivity as high as 100% can be achieved over pure In_2O_3 at low temperature.[4] However, STY of methanol remains low due to low CO_2 conversion. Several studies have been directed to improve the activity, although the methanol productivity remains low.

One way to increase the STY of methanol was to increase the oxygen vacancy density over In_2O_3. Supporting In_2O_3 over ZrO_2 increased oxygen vacancy due to the tensile force generated because of the crystal mismatch between In_2O_3 (cubic) and ZrO_2 (monoclinic).[5] Another way was to increase the H_2 dissociation by introducing transition metals (specially, noble metals). While transition metal promoters could

effectively increase the methanol productivity, the activity was found to be dependent on the structure and the nature of the active site. For example, Li et al. showed that single atomic Pt^{n+} species helped in heterolytic H_2 dissociation that promoted methanol formation while Pt nanoparticle promoted RWGS reaction via homolytic dissociation of H_2.[6] Small clusters of Pd were found to be effective for methanol production via increasing hydrogen dissociation and spillover on the surface of In_2O_3.[7,8] On the other hand, synergy between Pd-In or Rh-In alloy with In_2O_3 enhanced methanol production.[9,10] Formation of low nuclearity clusters of In with Pd was the active site for the production of methanol with high STY of 1.01 $g_{MeOH}\ h^{-1}\ g_{cat}^{-1}$).[11]

From the above discussion it is clear that the structure and nature of the metal promoters have additional crucial influence on the catalytic activity of In_2O_3 besides increasing the formation of oxygen vacancies and hydrogen dissociation. Although several promotional strategies were employed, there is little information about the effect of a dopant in In_2O_3 for CO_2 hydrogenation to methanol. Use of dopants can ensure the formation of one type of active site (M-O-In). Achieving atomic dispersion using dopants will also ensure the highest utilization of the interfacial site. Therefore, In_2O_3 catalysts doped with different transition metals from groups 8, 9 and 10 of the periodic table were designed to find out the best promoter for In_2O_3 and to investigate the influence of atomically dispersed dopants on the catalytic activity. The results show that atomically dispersed Rh atoms in In_2O_3 are highly active to promote the CO_2 hydrogenation to methanol. Rh directly takes part in CO_2 activation and increased the intermediate formate formation apart from increasing oxygen vacancies and H_2 dissociation.

2.2 Experimental method

2.2.1 Materials

Indium nitrate ($In(NO_3)_3 \cdot 3H_2O$), rhodium nitrate (aqueous solution of $Rh(NO_3)_3$ (25 wt.%) and nitric acid (9 wt.%), iron nitrate ($Fe(NO_3)_3 \cdot 9H_2O$), nickel nitrate ($Ni(NO_3)_2 \cdot 6H_2O$), cobalt nitrate ($Co(NO_3)_2 \cdot 6H_2O$), ruthenium chloride ($RuCl_3 \cdot xH_2O$), hydrogen hexachloroplatinate ($H_2PtCl_6 \cdot 2H_2O$), zinc nitrate ($Zn(NO_3)_2 \cdot 6H_2O$), citric acid, sodium carbonate (Na_2CO_3) and silicon carbide (SiC) (β form, particle size 50 nm) were purchased from Fujifilm Wako Pure Chemical Corporation. Palladium nitrate ($Pd(NO_3)_3 \cdot 2H_2O$) was bought from Sigma Aldrich.

2.2.2 Catalyst preparation

The In_2O_3 based doped oxide catalysts were prepared by using a sol–gel method in the presence of citric acid. A typical procedure to obtain the Rh-1.3-In_2O_3 catalyst is as follows: $In(NO_3)_3 \cdot 3H_2O$ (4.75 mmol) and $Rh(NO_3)_3$ (0.062 mmol) were added to a beaker containing 30 mL of distilled water along with 5 mmol of citric acid. The beaker was placed over a hot plate maintained at 130 °C and stirred until a foaming gel was formed. The gel was then dried by placing the beaker in an oven maintained at 130 °C for 5 h. The resulting composite was crushed and calcined at 500 °C for 3h to obtain the final catalyst. Other catalysts were prepared by changing the amount or type of the second metal precursor. The catalysts were named as M-X-In_2O_3, where X is the atom% of M with respect to the total metal content (M + In) of the catalyst and M represents the type of dopant metal (Fe, Ru, Co, Rh, Ni, Pd, or Pt) [$X = (M/(M+In)) \times 100\%$]. Undoped In_2O_3 was produced using the same method in the absence of dopant precursors.

For catalyst synthesis using coprecipitation method, 0.1 g/mL Na_2CO_3 solution was added dropwise to a 30 mL aqueous solution of $In(NO_3)_3 \cdot 3H_2O$ (4.75 mmol) and $Rh(NO_3)_3$ (0.062 mmol) under vigorous stirring until the pH became 9. After aging for

1 h under stirring condition, the precipitate was centrifuged and washed thoroughly with water. It was dried at 130 °C in an oven for 12 h followed by calcination at 500 °C for 3 h. The catalyst was named as Rh-1.3-In_2O_3 CP.

For catalyst prepared using wet impregnation, an equivalent amount of Rh present on the surface of Rh-1.3-In_2O_3 was loaded on In_2O_3. In a typical procedure, In_2O_3 (0.5 g, prepared by sol-gel method) was dispersed in 30 mL of water followed by the addition of $Rh(NO_3)_3$ (20 μL of 0.0491 g mL^{-1} aqueous solution) and the mixture was kept under stirring at room temperature for 30 minutes. Water was evaporated under reduced pressure and then the powder was dried at 130 °C for 12 h followed by calcination at 500 °C for 3h. This catalyst was named as Rh/In_2O_3 WI.

2.2.3 Catalyst characterization

X-ray diffraction (XRD) was measured with Rigaku MiniFlex using CuKα X-ray (λ = 1.54 Å) operating at 40 kV and 20 mA. X-ray photoelectron spectroscopy (XPS) was performed with JEOL JPS-9010MC instrument. Charge correction was made by adjusting the external carbon peak to 284.6 eV. High-angle annular dark-field scanning transmission electron microscopy (HAADF-STEM) images were obtained in a JEOL JEM-ARM200F atomic resolution electron microscope at an acceleration voltage of 200 kV equipped with EDS detector EX-24221M1G5T. Temperature programmed reduction (TPR) of the catalysts were carried out in the presence of a H_2 / Ar mixture (H_2 = 5%) on a BELCAT II instrument equipped with a TCD. Prior to the measurement, the catalysts were pretreated at 150 °C for 1 hour under an Ar flow. Measurements were done at a total flow rate of 50 mL min^{-1} with a ramp rate of 10 °C min^{-1} . CO pulse chemisorption was also performed on the BELCAT II at 50 °C. Prior to the measurement, the samples were reduced under a H_2 flow at 200 °C for 1 h. Calculations were done considering the stoichiometric ratio of Rh : CO = 1 : 2 because the Rh single

atom binds with two CO molecules.[12] The CO_2 temperature programmed desorption (CO_2 TPD) experiment was performed on the BELCAT II instrument equipped with a BELMass gas mass spectrometer. Prior to the measurement, the samples were pretreated either with Ar or with a mixture of CO_2 : H_2 (1 : 4) at 300 °C for 30 min. The sample was then cooled to room temperature under a gas flow and then He was used to purge the sample cell for 30 min. In TPD analysis under a He flow, the temperature was increased by 10 °C min^{-1}. For formic acid TPD, formic acid was first impregnated on the catalyst in a hexane solution followed by drying at room temperature. The TPD analysis was carried out under a He flow and the temperature was increased by 10 °C min^{-1}.

X-ray absorption fine structure (XAFS) measurements at the Rh K-edge of the Rh-1.3-In_2O_3 (fresh and used) and $Rh(acac)_3$ samples were performed at the Stanford Synchrotron Radiation Light Source (SSRL) at beamline 4-1. This beamline is an unfocused, 20-pole, 2-Tesla wiggler side station with a vertical collimating mirror. The samples were prepared via pressing 70 mg of the catalyst into a pellet approximately 7 mm in diameter. The pellet was then placed between two layers of Kapton tape and held in the beamline at a 45 degree angle in the direction of the fluorescence Lytle detector. XAS data were collected from 22 984 to 24 081 eV (∼14.9 Å−1 in k-space) on both the sample and Rh metal reference foil simultaneously. In order to improve the signal to noise ratio, four scans (11 minutes each) were collected, and then aligned and merged using the Rh foil spectrum collected simultaneously for each scan. The samples were scanned simultaneously in transmission and fluorescence detection modes using ion chambers (filled with argon) and the Lytle detector, respectively.

2.2.4 Evaluation of catalytic activity

The catalytic activity for CO_2 hydrogenation was evaluated in a stainless-steel packed bed flow system (Figure 2.1). Products were analyzed using an online GC (Shimadzu, GC 8A) equipped with two columns (Porapak Q and molecular sieve) and a TCD. The gas line from the outlet of the reactor to the inlet of the GC was heated at 150 °C to prevent condensation of methanol and H_2O. Typically, 200 mg of catalyst (mixed with an equal amount of silicon carbide (SiC)) was loaded into the reactor and held in place by quartz wool. A thermocouple was inserted into the reactor to measure the catalyst bed temperature. Prior to the reaction, the catalyst was pretreated under 0.5 MPa Ar for 1 h at 300 °C. Then the reactor was cooled to 50 °C under Ar and pressurized under reaction conditions using a mixture of H_2, CO_2 and Ar having the ratio H_2 : CO_2 : Ar = 4 : 1 : 1. After the system pressure became stable, the reactor temperature was increased to a desired value. Reactions at a space velocity (SV) higher than 30,000 mL h^{-1} g^{-1} were carried out by lowering the amount of catalyst and maintaining the same gas flow rate.

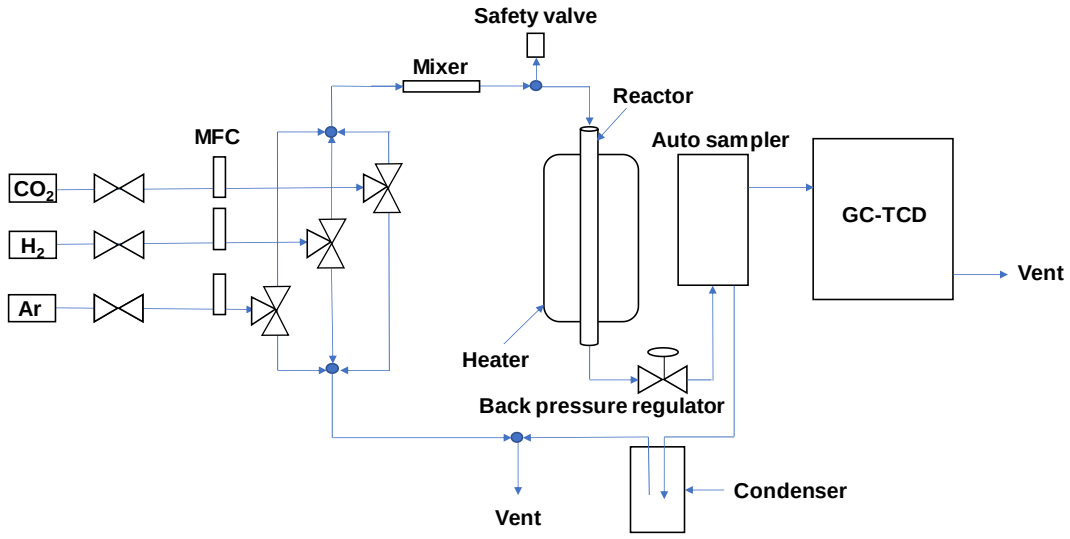

Figure 2.1: Schematic representation of reaction set up.

2.2.5 Equations

CO_2 conversion, selectivity of CO, CH_3OH and CH_4 and STY of CH_3OH were calculated using the following equations.

CO_2 conversion:

$$X_{(CO_2)} = \left(\frac{nCO_{out} + nCH_3OH_{out} + nCH_{4\,out}}{nCO_{2\,out} + nCO_{out} + nCH_3OH_{out} + nCH_{4\,out}}\right) \times 100\% \quad (2.1)$$

CO and CH_3OH selectivity

$$S_{(CO)} = \left(\frac{nCO_{out}}{nCO_{out} + nCH_3OH_{out} + nCH_{4\,out}}\right) \times 100\% \quad (2.2)$$

$$S_{(CH_3OH)} = \left(\frac{nCH_3OH_{out}}{nCO_{out} + nCH_3OH_{out} + nCH_{4\,out}}\right) \times 100\ \% \quad (2.3)$$

$$S_{(CH_4)} = \left(\frac{nCH_{4out}}{nCO_{out} + nCH_3OH_{out} + nCH_{4\,out}}\right) \times 100\ \% \quad (2.4)$$

STY:

$$STY_{(product)} = \left(\frac{SV \times [CO_2] \times X_{(CO_2)} \times S_{(product)} \times M_{(product)}}{22400}\right) \quad (2.5)$$

Where $nCO_{2\,out}$, nCO_{out}, nCH_3OH_{out}, nCH_{4out} are moles of CO_2, CO and CH_3OH calculated from GC analysis. SV is space velocity in mL h^{-1} g^{-1}, $[CO_2]$ is the concentration of CO_2 present in the feed gas mixture in %, and $M_{(product)}$ is molecular weight of respective product. STY of CH_3OH is reported in g_{MeOH} h^{-1} g_{cat}^{-1}.

2.2.6 Theoretical calculations

Gaussian 16 rev. A.03 program was used for density functional theory (DFT) calculation and initially a $In_{24}O_{36}$ cluster was built to qualitatively evaluate the chemical reactions on In_2O_3 (110) surface, where the initial geometry was the same as that of crystal In_2O_3. The DFT calculations for Rh doping on the surface were performed by using the PBE functional with the density fitting approximation.[13–15] Basis sets were def2-SVP for the central three metal atom sites that were potential Rh doping sites; 6-

31+G(d) for O atoms surrounding the three metal atoms; 3-21+G for other O atoms; LanL2DZ for In atoms in vicinal positioning to O atoms with the 6-31+G(d) basis set; LanL2MB for other In atoms.[16–20] This combination was used to decrease the number of basis as much as possible so that the self-consistent field calculations converged within acceptable time (*ca.* one week using an Intel Xeon Gold 6142 processor). Suitable effective core potential (ECP) was applied for Rh and In atoms. Empirical dispersion was included by Grimme's D3 function.[21] Spin multiplicity was optimized, and the self-consistent field solution was re-optimized with the *stable=opt* option to find the most stable electronic state in all calculations. The material had three possible sites for Rh (M_1 to M_3 in Figure 2.10a), locating at the center of the model. After replacing one In atom with Rh, orientation of the three metal sites and surrounding O atoms was optimized, where other atoms were frozen to preserve the crystal structure. The *loose* level of geometry optimization [root mean square (RMS) force < 0.001667 a.u., RMS displacement < 0.006667 a.u.] was used to decrease calculation time. Error in electronic energy due to use of the *loose* option was less than 0.1 kJ mol^{-1}, which was accurate enough to discuss the Rh sites.

Other calculations were performed after reducing the number of atoms to 40 at the PBE0-D3 level of theory with the *tight* level of geometry optimization (RMS force < 0.00045 a.u., RMS displacement < 0.0012 a.u.), and zero-point vibration energy was involved in the energy calculations.[22,23] Basis sets were slightly improved, compared to that employed for the 60-nuclei system. The In atom at the central light blue atom, corresponding to M_3 in Fig. 2.10a, was replaced with Rh when effect of doping was evaluated. To calculate the removal energy of lattice oxygen, oxygen atoms surrounding M_3 (In or Rh) were removed by the following Equation 2.6:

$$MO_x + H_2 \rightarrow MO_{x-1} + V_o + H_2O \quad (2.6)$$

For the evaluation of CO_2 activation, CO_2 was located above the left (M_2) and the central light blue metal (M_3) atoms after removing a designated number of lattice oxygen atoms around M_3. In the transition state calculations, only one imaginary frequency vibration and intrinsic reaction coordinates (IRC) that connect expected substrates and products were confirmed.

2.3 Results and Discussion

2.3.1 Catalytic activity

The doped indium oxide catalysts were prepared by sol-gel by using citric acid as the chelating agent. After polymerization of gel, it was calcined at 500 °C to obtain the doped oxides. For initial screening all doped catalysts were prepared with 5 atom % metal doping in In_2O_3. The catalytic activity of transition metal doped In_2O_3 catalysts along with pure In_2O_3 was evaluated at 270 °C, 5 MPa and 30,000 mL h^{-1} g_{cat}^{-1} space velocity (SV) (Figure 2.2a). This condition was chosen as the lower temperature and higher pressure favors methanol formation. At this condition, pure In_2O_3 showed 70% methanol selectivity with 3.7 % CO_2 conversion. The methanol STY was 0.18 g_{MeOH} h^{-1} g_{cat}^{-1}. This result was in line with previously reported activity of pure In_2O_3. Among the doped catalysts, Fe and Ru doped In_2O_3 increased the methanol selectivity in comparison to pure In_2O_3 (87% and 79% respectively). However, the CO_2 conversion was low resulting lower STY. Pt doped In_2O_3 catalyst produced CO as major product instead of methanol. Co, Ni, Pd and Rh dopants showed increased CO_2 conversion without major change in methanol selectivity. Rh doped catalyst surpassed all other catalysts and high CO_2 conversion (10%) was achieved with a methanol selectivity of 71%. As a result, the STY of methanol was 0.52 g_{MeOH} h^{-1} g_{cat}^{-1}, which was 2.9 times higher than that of pure In_2O_3.

Next, In_2O_3 catalysts with different amount of Rh were tested to identify optimum Rh loading (Figure 2.2b). Catalyst containing Rh loading as low as 0.64 atom% with respect to total metal content showed 1.8 time higher STY of methanol than pure In_2O_3. Rh loading of 1.3 atom% was enough to obtain high methanol productivity. Increasing the loading beyond 1.3 atom% did not increase the methanol STY. Different methods of catalyst preparation were also compared to access their influence on activity. (Figure 2.2c). Catalyst prepared by sol-gel method showed the highest activity when compared with catalysts prepared by co-precipitation and impregnation methods. It was determined that presence of higher concentration of Rh atoms on the surface of sol-gel catalyst was the reason behind its high activity *(vide infra)*.

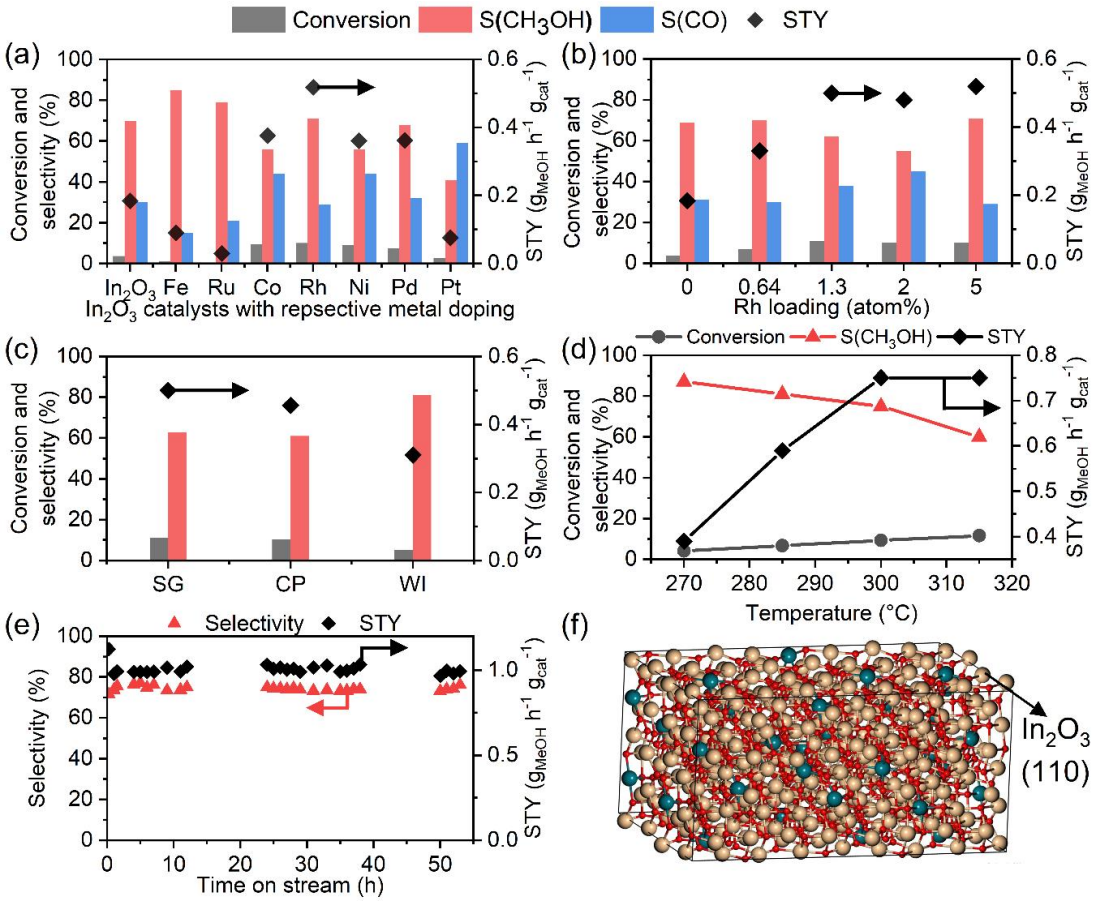

Figure 2.2: (a) Screening of different metal promoters for CO_2 hydrogenation (reaction conditions: M-5-In_2O_3, 270 °C, 5 MPa, 30,000 mL h^{-1} g_{cat}^{-1}, and H_2/CO_2 = 4); (b) optimization of Rh loading (reaction conditions: Rh-*X*-In_2O_3, 270 °C, 5 MPa, 30,000 mL h^{-1} g_{cat}^{-1}, and

H_2/CO_2 = 4); (c) comparison of Rh-1.3-In_2O_3 catalysts prepared using different methods. SG, CP and WI represent sol–gel, co-precipitation and wet impregnation methods, respectively (reaction conditions: 270 °C, 5 MPa, 30,000 mL h^{-1} g_{cat}^{-1}, and H_2/CO_2 = 4); (d) effect of temperature on methanol production from CO_2 (reaction conditions: Rh-1.3-In_2O_3, 5 MPa, 45,000 mL h^{-1} g_{cat}^{-1}, and H_2/CO_2 = 4); (e) evaluation of methanol selectivity and STY over time on stream (reaction conditions: Rh-1.3-In_2O_3, 300 °C, 5 MPa, 60,000 mL h^{-1} g_{cat}^{-1}, and H_2/CO_2 = 4); (f) graphical representation of Rh doped into the In_2O_3 (110) plane (blue for Rh, light brown for In and red for the oxygen atom, respectively).

Optimization of reaction condition was performed using Rh-1.3-In_2O_3 catalyst. Figure 2.2d shows the effect of temperature on methanol selectivity and STY. At 270 °C (under 5 MPa and 45,000 mL h^{-1} g_{cat}^{-1} space velocity) methanol selectivity was 87% with a STY of 0.39 g_{MeOH} h^{-1} g_{cat}^{-1} and CO_2 conversion of 4.2%. Increasing temperature had a positive effect on the STY until 300 °C. The CO_2 conversion increased from 4.2% to 9.3% with a methanol selectivity of 75% when the reaction temperature was increased from 270 °C to 300 °C. As a result, the STY increased from 0.39 to 0.75 g_{MeOH} h^{-1} g_{cat}^{-1}. Further increase in temperature promoted the competing RWGS reaction and the methanol selectivity decreased (Figure 2.2d). The best result was obtained at 300 °C, 60,000 mL h^{-1} g_{cat}^{-1} SV and 5 MPa pressure. At this condition, the methanol STY was 1.0 g_{MeOH} h^{-1} g_{cat}^{-1}, which is one of the highest reported so far under comparable reaction condition (Figure 2.2e). The catalyst stability was checked for 50 h under this condition and no change in STY or methanol selectivity was observed.

2.3.2 Characterization

Having confirmed the high activity and stability of Rh doped In_2O_3 catalysts, they were thoroughly characterized to understand the promotional effect of Rh. Citric acid based sol-gel method was used to prepare mixed oxide with Rh and In to avoid heterogeneity in the distribution of Rh atoms. Because of the formation of mixed oxide,

it is expected that the Rh atoms were doped throughout the In_2O_3 crystal (Figure 2.2f) and some Rh atoms were present on the surface. The amount of Rh present on the surface was calculated using CO as probe molecule. The amount of CO adsorbed on the surface of the catalyst prepared by citric acid based sol-gel method was 76 μL g^{-1}. In comparison, CO adsorption over catalysts prepared using co-precipitation (70 μL g^{-1}) and wet impregnation (48 μL g^{-1}) was lower. Furthermore, the surface Rh/In ratio calculated from XPS was higher for sol-gel catalyst (0.018) as compared to co-precipitated catalyst (0.012). Therefore, the higher activity of sol-gel catalyst in comparison to co-precipitated and impregnated catalyst can be explained by higher exposed Rh present on the surface.

Undoped In_2O_3 had a cubic crystal structure with crystallite size of 15-20 nm (Figure 2.3a). The crystal structure and size did not change after any amount of Rh doping. Diffraction peaks for Rh nanoparticles were not detected in XRD analysis before and after the reaction. With increasing the Rh loading, the 222 peak of In_2O_3 shifted towards higher 2θ value (Figure 2.3b). This shifting was caused by the decrease in the interplanar distance as a result of replacement of In^{3+} (0.8 Å) with Rh^{3+} having smaller ionic radius (0.66 Å).[24] Consequently, a gradual decrease in the lattice parameter value was also observed (Table 2.1). Hence, it can be concluded that doping of Rh in In_2O_3 crystal happened without the formation of Rh clusters.

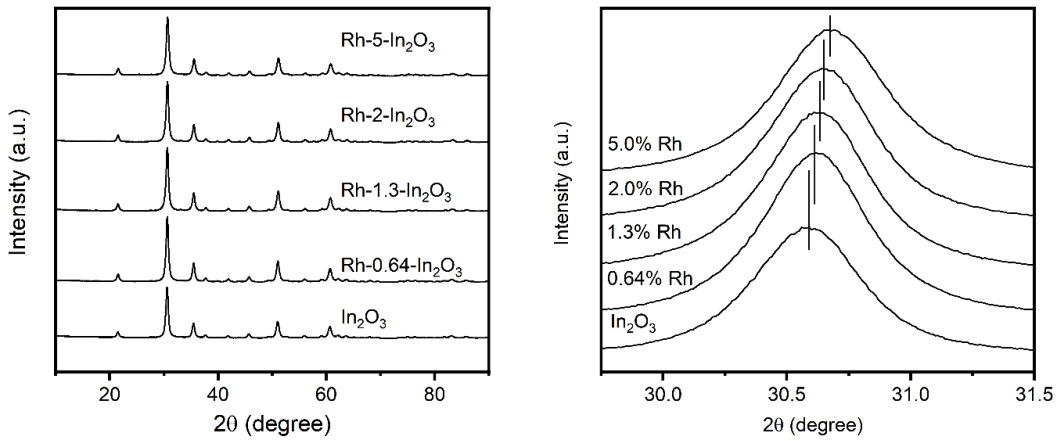

Figure 2.3: (a) XRD of Rh doped In_2O_3 catalysts and (b) shifting of In_2O_3 (222) peak as a result of doping of Rh.

Table 2.1: XRD analysis of (222) peak for In_2O_3 and Rh-X-In_2O_3 catalysts.

Rh mol %	2θ (degree)	d spacing (Å)	Lattice parameter (a) (Å)
0	30.57	2.921	10.1186
0.64	30.60	2.918	10.1082
1.3	30.61	2.917	10.1048
2	30.63	2.915	10.0978
5	30.66	2.912	10.0875

Figure 2.4a and 2.4e show the HAADF-STEM images for fresh and used Rh-1.3-In_2O_3 catalysts. No Rh nanoparticles were detected in both the fresh and used catalysts. Although atomic resolution was attained, individual Rh atoms could not be identified because of the similar brightness of Rh and In atoms in the HAADF-STEM analysis. Nevertheless, Rh was uniformly distributed in the catalyst as observed in the EDX analysis (Figure 2.4b-d and f-h).

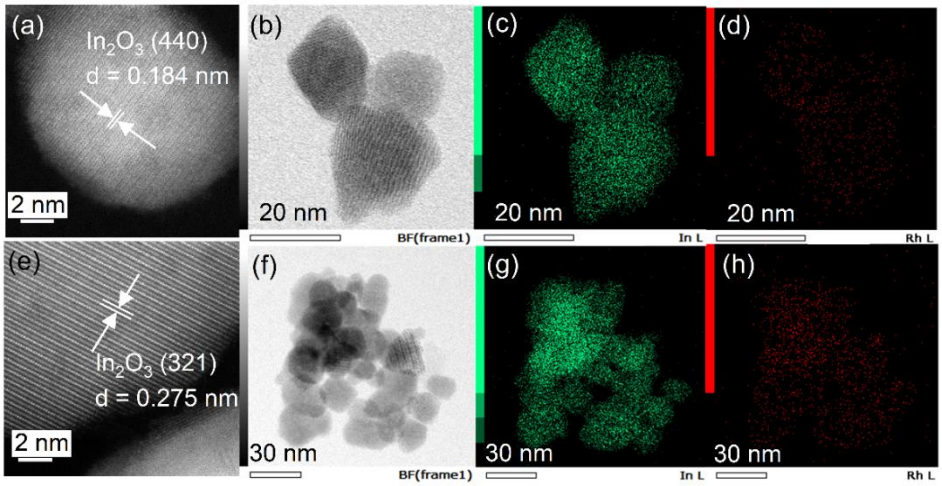

Figure 2.4: HAADF-STEM images for fresh (a) and used (e) catalysts. EDX mapping for fresh (b, c, d) and used (f, g, h) catalysts.

XAFS analysis was carried out to understand the local structure around Rh atoms. The Rh K-edge in the X-ray absorption near edge structure (XANES) region for fresh and used Rh-1.3-In_2O_3 was at a lower energy than for Rh foil. The adsorption edge for used catalyst was slightly lower than that for the fresh catalysts (Figure 2.5a). The fitting for the extended X-ray absorption fine structure (EXAFS) was done by replacing one In atom with Rh in the In_2O_3 cubic crystal (Figure 2.5b). The results of the fitting are shown in Table 2.2. For fresh catalyst, in the first coordination shell, Rh-O bonding was detected with a coordination number of 6.1 ± 0.7 and bond length of 2.05 ± 0.01 Å. This bond length was lower than the expected In-O bond length due to lattice contraction as observed in the XRD.[25] Rh-In coordination distances were 3.30 ± 0.01 Å and 3.38 ± 0.03 Å for second and the third coordination shell respectively. The Rh-In distances were also slightly short as compared to the expected In-In distances indicating the replacement of In with Rh atoms.[26] In the used catalyst, the Rh-O coordination number in the first shell was slightly lower (5.2 ± 0.6). The lower coordination number was the result of reduction of surface Rh atoms under

hydrogenation condition. Moreover, metallic Rh-Rh bonding was not observed in both the fresh and used catalysts (Figure 2.5c). These results in association with HAADF-STEM and XRD results suggest that Rh atoms are atomically dispersed in In_2O_3 crystal matrix (Figure 2.2f).

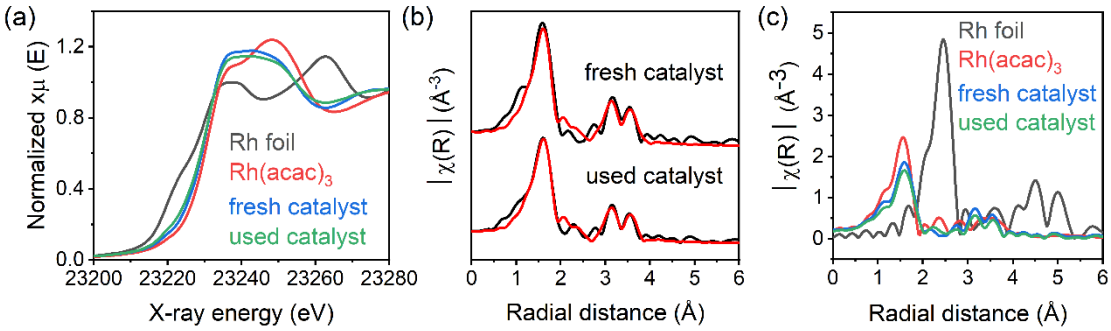

Figure 2.5: (a) XANES and (b) EXAFS spectra of fresh and used Rh-1.3-In_2O_3 catalysts. Black and red lines in EXAFS spectra represent the data and fitting using Rh doped model, respectively. (c) EXAFS spectra of fresh and used Rh-1.3-In_2O_3 along with reference materials ($Rh(acac)_3$ and Rh foil).

Table 2.2: Results of fitting of the EXAFS spectra for fresh and used Rh-1.3-In_2O_3 catalysts and $Rh(acac)_3$ used as reference.

Sample	Fresh[a]	After reaction[a]	$Rh(acac)_3$
N_{Rh-O}	6.1±0.7	5.2±0.6	6.4±0.9
R_{Rh-O} (Å)	2.05±0.01	2.05±0.01	1.99±0.01
$\sigma^2_{Rh-O} \times 10^3$ (Å^2)	5±1	4±1	2±2
$\Delta E_{0\ Rh-O}$ (eV)	7.0±1.3	8.3±1.2	7.9±1.9
$N_{Rh-In/Rh}$	5.3±1.8	5.3±1.8	-
$R_{Rh-In/Rh}$ (Å)	3.30±0.01	3.30±0.02	-
$\sigma^2_{Rh-In/Rh} \times 10^3$ (Å^2)	8±2	9±3	-
$\Delta E_{0\ Rh-In/Rh}$ (eV)	7.0±1.3	8.3±1.2	-
$N_{Rh-In/Rh}$	4.5±2.7	3.0±2.5	-
$R_{Rh-In/Rh}$ (Å)	3.82±0.03	3.83±0.03	-
$\sigma^2_{Rh-In/Rh} \times 10^3$ (Å^2)	8±4	7±5	-
$\Delta E_{0\ Rh-In/Rh}$ (eV)	7.0±1.3	8.3±1.2	-
Reduced χ^2	249	199	9433
R-factor	0.0086	0.0094	0.0022

XPS analysis was carried out to understand the chemical state of surface Rh and neighboring In atoms. The analysis of Rh 3d XPS showed prominent Rh $3d_{5/2}$ peak at 308.7 eV, which is indicative of the presence of Rh^{3+} species (Figure 2.6a).[27,28] A small peak around 307.2 eV appeared for Rh with a chemical state close to zero due to the partial reduction of surface Rh species during XPS analysis. For the used catalyst, the prominent peak appeared at 307.0 eV was assigned to presence of $Rh^{\delta-}$ (Figure 2.6b). This slight negative state of reduced Rh atoms was present because of the electronic charge transfer from partially reduced In atoms. The formation of partially reduced In atoms was also detected in the MNN spectra of the used catalyst (Figure 2.6c). The shoulder peak appeared in between the expected binding energy for In^{3+} and In^0 representing the formation of partially reduced In species.[29] This kind of strong metal-support interaction has been previously reported for TiO_2 and ZnO supported Rh catalysts to stabilize the Rh atoms, which are prone to sinter under hydrogenation condition.[30,31]

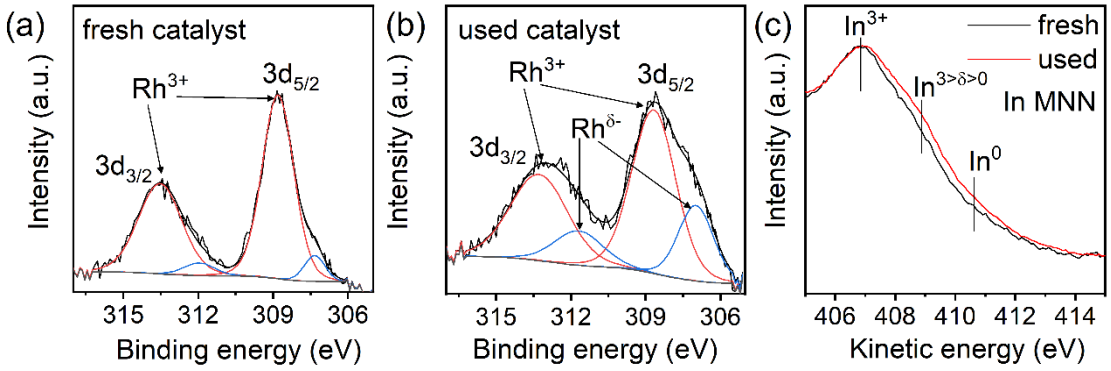

Figure 2.6: (a and b) Rh 3d XPS analysis of fresh and used Rh-1.3-In_2O_3 catalysts. (c) In MNN XPS spectra of fresh and used catalysts. The used catalyst was analyzed after 10 h of reaction.

The formation of partially reduced In and reduced Rh species suggests removal of oxygen and creation of oxygen vacancy. This was investigated in the H_2 TPR analysis (Figure 2.7). Pure In_2O_3 showed a small H_2 consumption peak around 160 °C indicating creation of oxygen vacancy on the surface.[4] On Rh-1.3-In_2O_3 catalyst, a peak

at 95 °C appeared along with a tail extended towards higher temperature. The main peak was assigned to reduction of surface Rh species and the tail was assigned to further formation of oxygen vacancies. Theoretically, 0.0408 mmol g^{-1} of H_2 was required to reduce 0.0068 mmol g^{-1} of Rh atoms present on the surface of the catalyst. Experimental H_2 consumption in TPR analysis was 0.067 mmol g^{-1}, which was 1.6 times higher than expected theoretical H_2 consumption for only reduction of Rh. This extra hydrogen was consumed to create oxygen vacancy on the surface.

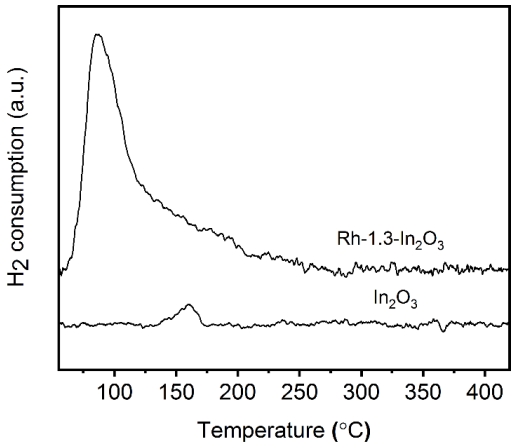

Figure 2.7: H_2 TPR analysis of Rh-1.3-In_2O_3 and pure In_2O_3.

The formation of oxygen vacancy was also observed in the O 1s XPS spectra. Figure 2.8 shows the O 1s XPS spectra of pure In_2O_3, fresh Rh-1.3-In_2O_3 and used Rh-1.3-In_2O_3 catalysts. In the XPS spectra, lattice oxygen atoms near an oxygen vacancy were assigned to the peak at 530.9 eV ($O_{near\ vacancy}$) and oxygen in surface hydroxyl (O-H) groups were assigned to the peak at 532 eV, which can also form because of creation of oxygen vacancy under hydrogenation atmosphere. Increase in proportion of these two peaks indicated the generation of oxygen vacancy. Cumulative of these two peaks was termed as O_{defect}. The amount of O_{defect} for pure In_2O_3 was 38% (Figure 2.8a) which did not change for the fresh Rh-1.3-In_2O_3 catalyst (Figure 2.8b) because Rh^{3+} replaced In^{3+} with a similar coordination number. After reaction for 1h (Figure 2.8c), O_{defect} increased to 43% and did not change after reaction of 10 h (Figure 2.8d).

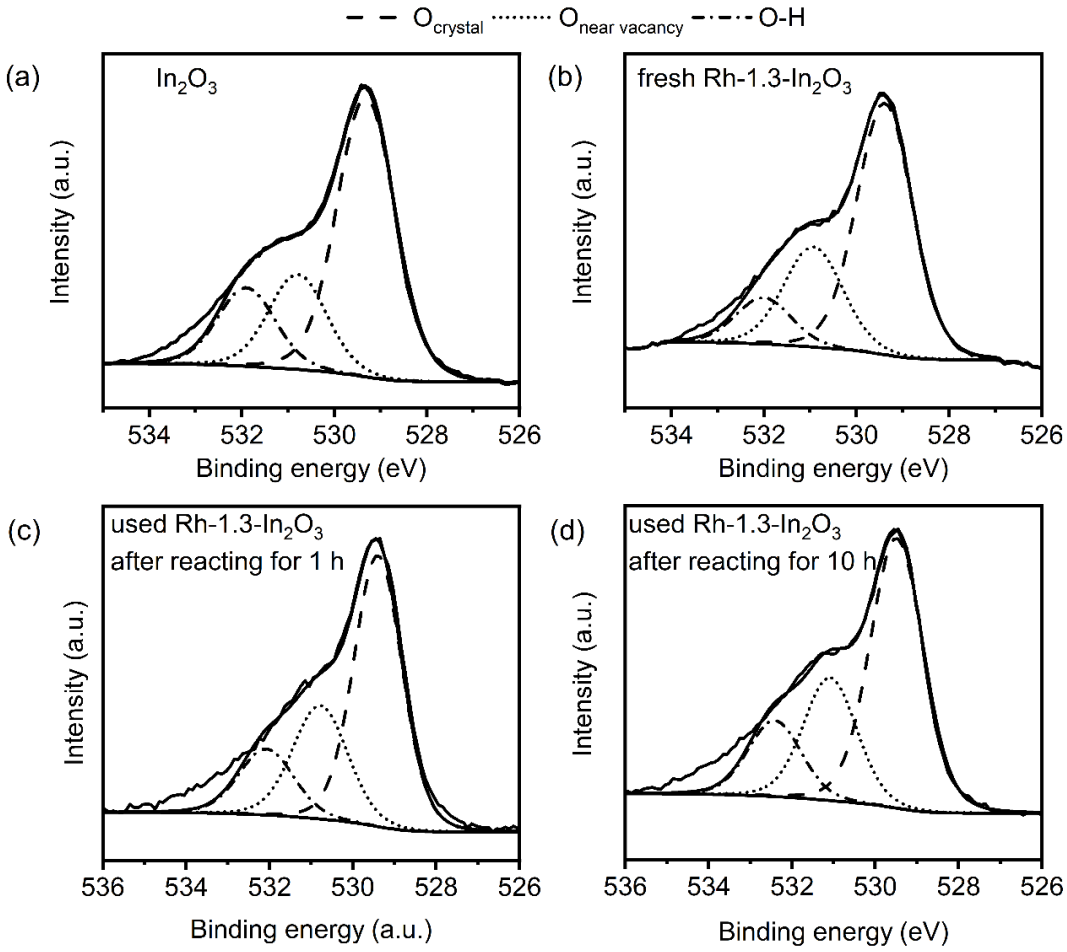

Figure 2.8: O 1s XPS of (a) pure In_2O_3, (b) fresh Rh-1.3-In_2O_3, (c) used Rh-1.3-In_2O_3 (after reacting for 1 h) and (d) used Rh-1.3-In_2O_3 (after reacting for 10 h).

The effect of oxygen vacancy on CO_2 adsorption was studied by TPD of pre-adsorbed CO_2 (Figure 2.9a). During TPD of CO_2, the desorption peak above 400 °C was assigned to chemisorbed CO_2 on the oxygen vacancy site of In_2O_3.[11,32,33] The amount of chemisorbed CO_2 increased for Rh-1.3-In_2O_3 indicating that inclusion of Rh helped in CO_2 adsorption.

Next, the TPD analysis was performed after pretreating the Rh-1.3-In_2O_3 catalyst under reaction condition (300 °C, 0.1 MPa, CO_2: H_2 = 1:4) (Figure 2.9b, red line showing the evolution of CO_2). One prominent peak appeared at 270 °C instead of the chemisorbed CO_2. It is speculated that this peak appeared because of the decomposition of formate, which is an intermediate for methanol formation. In the TPD spectra of a

sample containing pre-adsorbed formic acid over the surface of Rh-1.3-In_2O_3 (Figure 2.9b, green line), a similar peak appeared at the same temperature (270 °C) confirming the presence of formate.

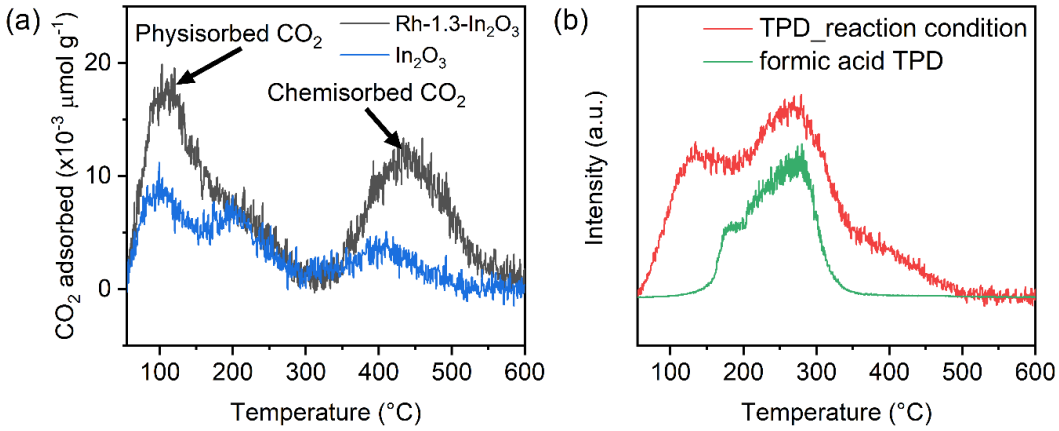

Figure 2.9: (a) CO_2 TPD profile over different catalysts. (b) TPD profile of Rh-1.3-In_2O_3 after treating under reaction condition (red line) and after impregnating formic acid (green line) showing the evolution of CO_2.

DFT calculations were carried out to understand the role of Rh doping in more detail. An $In_{24}O_{36}$ cluster model with atomic arrangement similar to 110 plane of In_2O_3 was used as the model. This structure was chosen because the 110 plane was reported as the most active for CO_2 hydrogenation (Figure 2.10). Doping of Rh at M3 site resulted in an average Rh-O bond length of 2.05 Å, which was similar to the Rh-O bond distance observed in EXAFS analysis. Under hydrogenation condition, incorporation of Rh atoms created high density of oxygen vacancy which promoted the CO_2 adsorption. Next hydrogen dissociation happened over Rh site and transfer of one H atom from Rh to C of CO_2 produced formate with low activation barrier (59 kJ mol^{-1}). These results are consistent with experimental observations that in the presence of Rh atoms, oxygen vacancies are increased leading to enhanced CO_2 adsorption and formate formation as an intermediate to methanol.

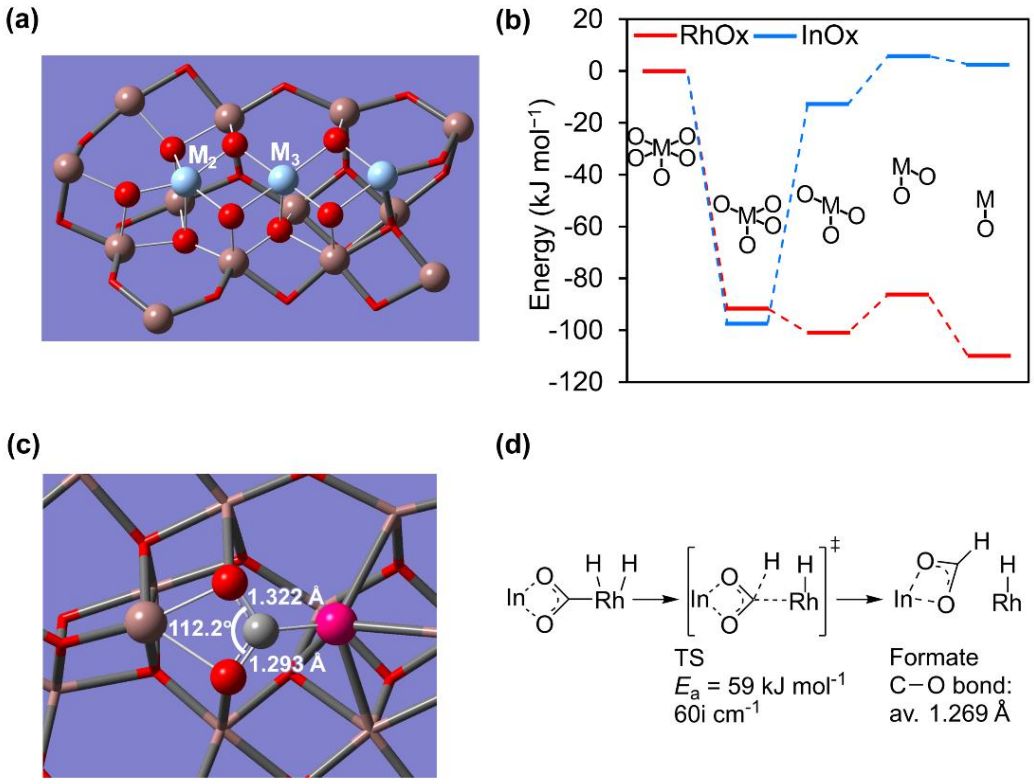

Figure 2.10: Model for evaluating oxygen vacancy formation and CO_2 activation. (a) structure of this system, (b) the removal of lattice oxygen around surface Rh or In ($MO_x + H_2 \rightarrow MO_{x-1} + V_{\ddot{O}} + H_2O$), (c) CO_2 adsorption on RhO site and (d) reduction of the CO_2, where only the important centers are depicted. Gray: C; pink purple: Rh. Basis sets: light blue metal atoms: def2-SVP; O atoms shown as red balls: 6-31++G(d); In atoms shown as brown balls: LanL2DZ; O atoms depicted as red stick: 3-21+G. The 6-31++G(d) basis set was applied for additional atoms (CO_2 and H_2).

2.4 Conclusion

In conclusion, among transition metals from group 8, 9 and 10 of periodic table, Rh was highly effective for increasing methanol productivity over In_2O_3. Rh was atomically dispersed and did not sinter under hydrogenation condition due to electronic charge transfer with neighboring partially reduced In atoms. Rh loading of as low as 1.3 atom% (0.96 wt%) was enough to achieve high methanol productivity. A stable STY of 1.0 g_{MeOH} h^{-1} $gcat^{-1}$ was achieved over Rh-1.3-In_2O_3 catalyst, which is one of

the highest till date. The promotional role of Rh was attributed to three factors – creation of oxygen vacancy, increase in strong CO_2 adsorption and promotion of formate formation. Under reaction condition, reduction of Rh atoms created oxygen vacancies around themselves. As a result, neighboring In atoms were also partially reduced. These oxygen vacancies along with Rh and partially reduced In atoms promoted strong CO_2 chemisorption and formate formation. The high methanol productivity under industrially relevant condition clearly points out the advantages of atomically dispersed Rh in In_2O_3 catalysts having oxygen vacancy close to Rh atoms. Therefore, this chapter shows that oxygen vacancy is one of the keys to improve the CO_2 adsorption and conversion. By doping of a suitable transition metal, the density of oxygen vacancy on In_2O_3 can be enhanced. Consequently, the oxygen vacancy at the interface of the two metals can be utilized to achieve selective products with high yield from CO_2. This leads to higher CO_2 adsorption and improved methanol yield while maintaining the high selectivity towards methanol.

References

1. J. Zhong, X. Yang, Z. Wu, B. Liang, Y. Huang and T. Zhang, *Chem. Soc. Rev.*, 2020, **49**, 1385–1413.
2. M. B. Fichtl, D. Schlereth, N. Jacobsen, I. Kasatkin, J. Schumann, M. Behrens, R. Schlögl and O. Hinrichsen, *Appl. Catal. A Gen.*, 2015, **502**, 262–270.
3. J. Ye, C. Liu, D. Mei and Q. Ge, *ACS Catal.*, 2013, **3**, 1296–1306.
4. O. Martin, A. J. Martín, C. Mondelli, S. Mitchell, T. F. Segawa, R. Hauert, C. Drouilly, D. Curulla-Ferré and J. Pérez-Ramírez, *Angew. Chemie Int. Ed.*, 2016, **55**, 6261–6265.
5. M. S. Frei, C. Mondelli, A. Cesarini, F. Krumeich, R. Hauert, J. A. Stewart, D. Curulla Ferré and J. Pérez-Ramírez, *ACS Catal.*, 2020, **10**, 1133–1145.
6. Z. Han, C. Tang, J. Wang, L. Li and C. Li, *J. Catal.*, 2021, **394**, 236–244.
7. J. Ye, C. J. Liu, D. Mei and Q. Ge, *J. Catal.*, 2014, **317**, 44–53.
8. N. Rui, Z. Wang, K. Sun, J. Ye, Q. Ge and C. jun Liu, *Appl. Catal. B Environ.*, 2017, **218**, 488–497.

9. J. L. Snider, V. Streibel, M. A. Hubert, T. S. Choksi, E. Valle, D. C. Upham, J. Schumann, M. S. Duyar, A. Gallo, F. Abild-Pedersen and T. F. Jaramillo, *ACS Catal.*, 2019, **9**, 3399–3412.
10. M. M. Li, H. Zou, J. Zheng, T. Wu, T. Chan, Y. Soo, X. Wu, X. Gong, T. Chen, K. Roy, G. Held and S. C. E. Tsang, *Angew. Chemie*, 2020, **132**, 16173–16180.
11. M. S. Frei, C. Mondelli, R. García-Muelas, K. S. Kley, B. Puértolas, N. López, O. V. Safonova, J. A. Stewart, D. Curulla Ferré and J. Pérez-Ramírez, *Nat. Commun.*, 2019, **10**, 1–11.
12. R. Lang, T. Li, D. Matsumura, S. Miao, Y. Ren, Y. T. Cui, Y. Tan, B. Qiao, L. Li, A. Wang, X. Wang and T. Zhang, *Angew. Chemie Int. Ed.*, 2016, **55**, 16054–16058.
13. J. P. Perdew, K. Burke and M. Ernzerhof, *Phys. Rev. Lett.*, 1997, **78**, 1396.
14. J. P. Perdew, K. Burke and M. Ernzerhof, *Phys. Rev. Lett.*, 1996, **77**, 3865–3868.
15. B. I. Dunlap, *J. Chem. Phys.*, 1983, **78**, 3140–3142.
16. P. J. Hay and W. R. Wadt, *J. Chem. Phys.*, 1985, **82**, 299–310.
17. W. R. Wadt and P. J. Hay, *J. Chem. Phys.*, 1985, **82**, 284–298.
18. P. J. Hay and W. R. Wadt, *J. Chem. Phys.*, 1985, **82**, 270–283.
19. R. Ditchfield, W. J. Hehre and J. A. Pople, *J. Chem. Phys.*, 1971, **54**, 720–723.
20. R. Gulde, P. Pollak and F. Weigend, *J. Chem. Theory Comput.*, 2012, **8**, 4062–4068.
21. S. Grimme, J. Antony, S. Ehrlich and H. Krieg, *J. Chem. Phys.*, 2010, **132**, 154104.
22. J. P. Perdew, M. Ernzerhof and K. Burke, *J. Chem. Phys.*, 1996, **105**, 9982–9985.
23. C. Adamo and V. Barone, *J. Chem. Phys.*, 1999, **110**, 6158–6170.
24. R. D. Shannon, *Acta Crystallogr. Sect. A*, 1976, **32**, 751–767.
25. D. Bruce Buchholz, Q. Ma, D. Alducin, A. Ponce, M. Jose-Yacaman, R. Khanal, J. E. Medvedeva and R. P. H. Chang, *Chem. Mater.*, 2014, **26**, 5401-5411.
26. C. A. Hoel, J. F. Gaillard and K. R. Poeppelmeier, *J. Solid State Chem.*, 2010, **183**, 761–768.
27. A. Bueno-López, I. Such-Basáñez and C. Salinas-Martínez De Lecea, *J. Catal.*, 2006, **244**, 102–112.
28. Y. Kwon, T. Y. Kim, G. Kwon, J. Yi and H. Lee, *J. Am. Chem. Soc.*, 2017, **139**, 17694–17699.
29. K. D. B. J. F. Moulder, W. F. Stickle, P. E. Sobol, *Handbook of X-ray Photoelectron Spectroscopy*, Minnesota, 1992.
30. R. Lang, T. Li, D. Matsumura, S. Miao, Y. Ren, Y. T. Cui, Y. Tan, B. Qiao, L. Li, A. Wang, X. Wang and T. Zhang, *Angew. Chemie Int. Ed.*, 2016, **55**, 16054–16058.
31. M. K. Samantaray, V. D'Elia, E. Pump, L. Falivene, M. Harb, S. Ould Chikh, L. Cavallo and J. M. Basset, *Chem. Rev.*, 2020, **120**, 734–813.

32. P. Gao, S. Li, X. Bu, S. Dang, Z. Liu, H. Wang, L. Zhong, M. Qiu, C. Yang, J. Cai, W. Wei and Y. Sun, *Nat. Chem.*, 2017, **9**, 1019–1024.
33. C. Y. Chou and R. F. Lobo, *Appl. Catal. A Gen.*, 2019, **583**, 117144.

Chapter 3

Co single atoms in ZrO_2 with inherent oxygen vacancies for selective hydrogenation of CO_2 to CO

Abstract

Chapter 2 showed that the atomic interface between single atomic Rh and In_2O_3 along with oxygen vacancy was important for methanol synthesis via formate intermediate. In this chapter, the concept of interfacial site with oxygen vacancy was applied to CO_2 hydrogenation to CO. This chapter shows that a catalyst with Co single atom in ZrO_2 having inherent oxygen vacancy is selective for the transformation of CO_2 to CO. The CO selectivity over these doped catalysts was higher than 95%. Due to the charge imbalance between Co^{2+} and Zr^{4+}, oxygen vacancies were formed near Co atoms. These oxygen vacancies improved CO_2 adsorption. Mechanistic study suggested that, first, CO_2 was hydrogenated to formate intermediate followed by its decomposition to CO instead of forming methanol via further hydrogenation. Methane formation was suppressed because CO adsorption was less favorable than CO_2 adsorption. Interfacial site between Co single atom and ZrO_2 having oxygen vacancy was found to be important for formate stabilization and weak CO adsorption leading to high CO selectivity.

3.1 Introduction

Among the C1 products obtained from reductive valorization of CO_2, CO is a versatile precursor for synthesis of several value added chemicals. Syngas, a mixture of CO and H_2 is widely used for the synthesis of many industrially important chemicals including alcohols, organic acids and hydrocarbons.[1–7] The reductive recycling of CO_2 to CO, also known as reverse water gas shift reaction (RWGS) (Equation 1.1) is an endothermic reaction.

The primary challenge in RWGS reaction is to achieve high CO selectivity because exothermic methanol and methane formation reactions (Equations 1.2 and 1.3) also happen simultaneously, especially at lower temperature. Therefore, significant efforts have been devoted towards designing catalysts for maximizing selectivity and understanding the underlying mechanism of CO formation.[8–10] Moreover, metal nanoparticles in conventional supported metal catalysts strongly adsorb CO formed via RWGS reaction. As a result, CO cannot desorb easily and the chance of further hydrogenation of CO to methane or methanol increases. Consequently, a better strategy in catalyst design is required.

In chapter 2, it was seen that design of catalysts with interfacial sites containing oxygen vacancies is a promising strategy for preparing highly active catalyst for CO_2 hydrogenation.[11,12] The oxophilic nature of oxygen vacancy promotes CO_2 adsorption and activates it for the hydrogenation by adjacent metal atoms resulting in high activity.[13] The oxygen vacant sites tend to stabilize the reaction intermediates such as formate and methoxy species and as a result, deep hydrogenation of CO_2 to CH_3OH and CH_4 was promoted.[14–16] Similarly, in a ZnO-ZrO_2 solid solution catalyst, methanol was formed via the hydrogenation of formate species stabilized at the interfacial site having oxygen vacancy.[16] Therefore, catalysts with isolated metal atoms adjacent to

oxygen deficient interface tend to produce CH_3OH and CH_4 selectively because the further hydrogenation of intermediates stabilized over the oxophilic interface is easier. In contrast, this chapter shows that high CO_2 hydrogenation activity along with high CO selectivity can be achieved by atomically dispersed Co atoms in ZrO_2 crystal through doping. It was speculated that if formate species were formed at the interfacial site of Co single atom and neighboring Zr atom and the further hydrogenation of formate to methanol is suppressed, then the formate species can decompose to CO. In this way, the selectivity of CO via CO_2 hydrogenation will be high, suppressing the formation of side product.

In this chapter, Co doped ZrO_2 catalysts were synthesized to form atomically dispersed Co atoms with oxygen vacancies and were applied for CO_2 hydrogenation under varying reaction conditions. The oxygen vacancies were formed due to the charge imbalance between Co^{2+} and Zr^{4+}. *Operando* diffuse reflectance infrared Fourier transform spectroscopy (DRIFTS) analysis was carried out to understand the reaction mechanism. DFT calculation was used to clarify the effect of Co doping on oxygen vacancy formation and its effect on CO_2 activation. The structure and property of active sites are elucidated in the view of the change in selectivity from methanol to CO to methane.

3.2 Experimental method

3.2.1 Catalyst Preparation

Cobalt doped ZrO_2 catalysts were prepared using co-precipitation method. A typical process to obtain Co-10-ZrO_2 is as follows. $Co(NO_3)_2.6H_2O$ (3 mmol, 0.87 g) and zirconyl nitrate (27 mmol, 7.2 g) were dissolved in a round bottomed flask containing 150 mL of water. NH_4OH solution was added dropwise to the metal solution under vigorous stirring until the pH became 9. The solution was aged for 1 h under

stirring condition. The precipitate was washed with water until the pH became 7. The precipitate was dried at 150 °C for 5h. The final catalyst was obtained after calcination at 500 °C for 3 h (ramp rate of 2 °C min^{-1}). Catalysts were named as Co-X-ZrO_2, where X is the atom % of Co with respect of total metal content (Co + Zr). Other catalysts with different Co loading were prepared by changing the amount of the precursors. Undoped ZrO_2 was prepared using the same method in the absence of Co precursor.

For comparison, Co impregnated on ZrO_2 catalyst was prepared with 10 atom % Co using the following method. ZrO_2 (1.2 g), prepared as per above method, was dispersed in 30 mL H_2O followed by the addition of $Co(NO_3)_2.6H_2O$ (0.29 g). The mixture was stirred at room temperature for 1 h. Water was evaporated under reduced pressure and then the powder was dried at 150 °C for 12 h followed by calcination at 500 °C for 3 h. This catalyst was named as Co/ZrO_2.

3.2.2 Catalyst characterization

XRD pattern was measured with Rigaku MiniFlex using CuKα X-ray (λ = 1.54 Å) operating at 40 kV and 20 mA. N_2 adsorption isotherms were measured at −196 °C using a Belsorp mini analyzer. Prior to the adsorption, all samples were degassed under vacuum at 120 °C for 2 h. Surface area was calculated by using BET theory between the relative pressure range 0.05 to 0.35 in the N_2 adsorption isotherm.[17] XPS was performed with JEOL JPS-9010MC instrument. Charge correction was done by adjusting the carbon peak to 284.6 eV. HAADF-STEM images were obtained in a JEOL JEM-ARM200F atomic resolution electron microscope at an acceleration voltage of 200 kV equipped with EDS detector EX-24221M1G5T. H_2 TPR of catalysts was carried out in presence of H_2-Ar mixture (H_2 = 5%) in a BELCAT II instrument equipped with a TCD detector. Prior to measurement, catalysts were pretreated at 150 °C for 1 h under Ar flow. Measurements were done at a total flow rate of 50 mL min^{-1}

with ramp rate of 10 °C min^{-1}. CO_2 TPD experiment was performed in the BELCAT II instrument equipped with BELMass gas mass spectrometer. Prior to measurement, the samples were pretreated under Ar at 340 °C for 30 min followed by CO_2 adsorption at room temperature for 30 min. After purging with He for 30 min, TPD was performed with a ramp rate of 10 °C min^{-1}. For formic acid decomposition experiment, formic acid was first impregnated on the catalyst in a hexane solution followed by drying at room temperature. The TPD of this catalyst was carried out under same condition used for CO_2 TPD.

XAFS measurements were carried out at BL9C beamline of photon Factory at the Institute for Material Structure Science in High Energy Accelerator Research Organization. (KEK-IMSS-PF)(Proposal No.2019P18). The X-rays emitted from 2.5 GeV storage ring operating at 450mA were monochromatized by a Si(111) double crystal monochromator. X-ray beam was focused, and higher harmonics were rejected by a bent cylindrical mirror. The incident and transmitted X-rays were monitored by 17 cm and 34 cm long ionization chambers filled with N_2. The samples were diluted with boron nitride and pressed into pellets with appropriate thickness. The presence of large amount of ZrO_2 caused severe absorption and limited edge height to 0.1-0.2. XAFS analysis was carried out using the REX package programs.[18] The amplitude and the phase functions were derived from FEFF calculation.[19] Additional analysis was done using Athena software using standard parameters.[20]

DRIFTS experiments were done using a Perkin Elmer Spectrum 100 FTIR spectrometer equipped with MCT detector cooled with liquid N_2. The catalyst was first pretreated under He at 280 °C for 30 min. One spectrum of catalsyt was recorded as background under He before flowing reactant gases (H_2:CO_2 = 4). Final IR spectrum of the adsorbed species was obtained by substracting the background spectrum of the

catalsyt. For operando experiment, the gas exiting the DRIFTS cell was fed to an online GC equipped with a molecular sieve column and a TCD. CO adsorption DRIFTS experiments were done at room temperature. Prior to the CO adsorption at room temperature, the catalyst was reduced under H_2 at 450 °C for 1 h.

3.2.3 Evaluation of catalytic activity

Catalytic activity for CO_2 hydrogenation was evaluated in a stainless-steel packed bed flow reactor system as shown in Chapter 2 (Figure 2.1). In a typical reaction, 450 mg of catalyst was loaded into the reactor and held in place by quartz wool. Prior to reaction, the catalyst was pretreated under 0.5 MPa Ar for 1 h at 300 °C. Then the reactor was cooled to 50 °C under Ar and pressurized to reaction condition using a mixture of H_2, CO_2 and Ar having the ratio H_2:CO_2:Ar = 4:1:1. After the system pressure was stable, reactor temperature was increased to desired value. Total flow rate was 75 mL min^{-1} to maintain space velocity at 10,000 mL h^{-1} g^{-1}. Reactions at space velocity higher than 30,000 mL h^{-1} g^{-1} were carried out by reducing the amount of catalyst and increasing the flow rate. CO_2 conversion, selectivity of CO, CH_3OH and CH_4, space time yield (STY) of CH_3OH and CO were calculated using Equations 2.1 to 2.5 stated in Chapter 2. STY of CO is reported in μmol g^{-1} s^{-1}.

3.2.4 Theoretical calculations

DFT calculations were carried out by using the Generalized gradient approximation (GGA)[21] with Perdew-Burke-Ernzerhof (PBE) functional implemented in the Vienna *ab initio* simulation package (VASP).[22] The DFT + U approach with a value of U = 4.0 eV was used in this calculation. The calculated lattice parameters for tetragonal ZrO_2 are a = b = 3.66 Å and c = 5.19 Å, which is consistent with the experimental value a = b =3.64 Å and c = 5.27 Å.[23]

The ZrO_2(101) surface with (2 × 3 × 2) element unit cell was chosen as the slab model with a vacuum spacing of 15 Å to separate the slabs. The computational model

of the Co doped ZrO_2 catalyst (Co-ZrO_2) was created by replacing one Zr atom at the top layer of ZrO_2(101) surface with one Co atom**.** The bottom layer was fixed to represent the bulk state and the other layers were fully relaxed. The forces tolerance on all unconstrained atoms were converged to 0.03 eV/Å. An energy cut-off of 400 eV and 3 × 3 × 1 k-point grid gave reliable converged results for total energies and forces. The threshold of SCF convergence was set to 10^{-4} eV. All calculations were spin polarized. The adsorption energy was calculated by Equation (3.1)

$$E_{ads} = E_{mol/slab} - E_{mol} - E_{slab} \quad (3.1)$$

where $E_{mol/slab}$, E_{mol} and E_{slab} correspond to the total energy of adsorbate on slab model, the energy of the isolated molecule in gas phase and surface substrate, respectively.

The oxygen vacancy formation energy (E_f) was calculated using Equation 3.2 as follows

$$E_f = E_{sur-vac} + E_{H_2O} - (E_{sur} + E_{H_2}) \quad (3.2)$$

where $E_{sur-vac}$, E_{H2O}, E_{H2}, E_{sur} are the total energy of the surface with one oxygen vacancy, the energy of gas water, hydrogen molecule, and surface without oxygen vacancy, respectively.

3.3 Results and discussion

3.3.1 Preparation and characterization of doped and impregnated Co catalysts on ZrO_2

Co doped ZrO_2 catalysts were prepared via co-precipitation method and were named as Co-X-ZrO_2 (X = atom % of Co with respect to total metal content Co+Zr; X = 1, 5, 10, 15, 50). For comparison, one catalyst was also prepared via impregnation method containing 10 atom% Co loading.

All catalysts were first characterized to determine the physical structure and chemical state of doped catalysts. The physical morphology of catalysts did not change

due to Co doping as observed in the N_2 adsorption analysis (Figure 3.1). In XRD pattern analysis, pure ZrO_2 showed diffraction patters for both monoclinic (*m*-ZrO_2) and tetragonal (*t*-ZrO_2) polymorphs (Figure 3.2a). Doping of Co changed the *m*-ZrO_2 phase to *t*-ZrO_2 due to incorporation of Co in the ZrO_2 crystal matrix. For doped catalysts with Co loading of 1-15 atom%, formation of CoO or Co_3O_4 was not observed. In Co-50-ZrO_2 and impregnated catalysts, diffraction for Co_3O_4 was observed. For catalysts with loading of 1-15 atom%, the (101) reflection of t-ZrO_2 gradually shifted to higher 2θ value with increase in Co loading (Figure 3.2b). This was caused by the reduction in interplanar distance in ZrO_2 because of incorporation of smaller Co^{2+} (0.74 Å) in place of Zr^{4+} (0.84 Å).[24] This also led to a gradual decrease in lattice parameter value. The change of *m*-ZrO_2 to *t*-ZrO_2 and gradual decrease in interplanar distance and lattice parameter with increasing Co loading suggests homogeneous doping of Co atoms in the ZrO_2 crystal matrix.

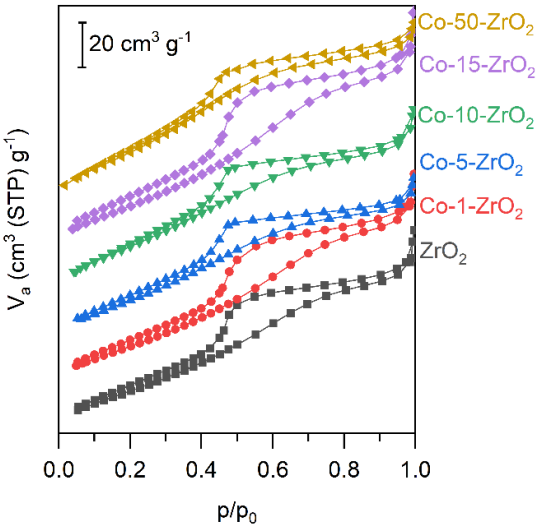

Figure 3.1: N_2 adsorption isotherms of Co-X-ZrO_2 catalysts.

Figure 3.2c shows the Co K-edge XANES spectra for all catalysts along with reference materials. The edge position of doped catalysts with Co loading of 1-15 atom% was at 7722 eV, which was assignable to Co^{2+} species. Co-50-ZrO_2 showed the

edge position at 7726 eV due to presence of Co^{3+} in Co_3O_4 (observed in XRD). Figure 3.2d shows the pre-edge region of the XANES spectrum. The height of the pre-edge peak around 7710 eV was related to 1s to 3d electronic transition, which was less favorable in the presence of centrosymmetry, for example in the case of CoO and $Co(CH_3COO)_2$. A larger pre-edge peak was observed for Co-50-ZrO_2 and impregnated catalyst because of the absence of centrosymmetry in Co_3O_4 due to its tetrahedral structure. The pre-edge peaks for doped catalysts (X = 1-15 atom%) were larger than CoO and $Co(CH_3COO)_2$ indicating that Co was not present in a centrosymmetric crystal structure, which is expected when it is homogeneously doped in ZrO_2. Figure 3.2e shows the EXAFS region for Co-10-ZrO_2 catalyst. The noise in EXAFS region was high due to the large background absorbance of ZrO_2. However, the EXAFS profile for Co-10-ZrO_2 differed from that of CoO and Co_3O_4. The Co-O bond distance of Co-10-ZrO_2 after curve fitting was 1.88 Å, smaller than Co-O in CoO (Table 3.1). The peak at 2.71 Å was assigned as the Co-Zr interaction although the bond length was short. From XAFS analysis, it was concluded that, in doped catalysts, Co atoms were divalent in nature and did not resemble the structure of CoO or Co_3O_4.

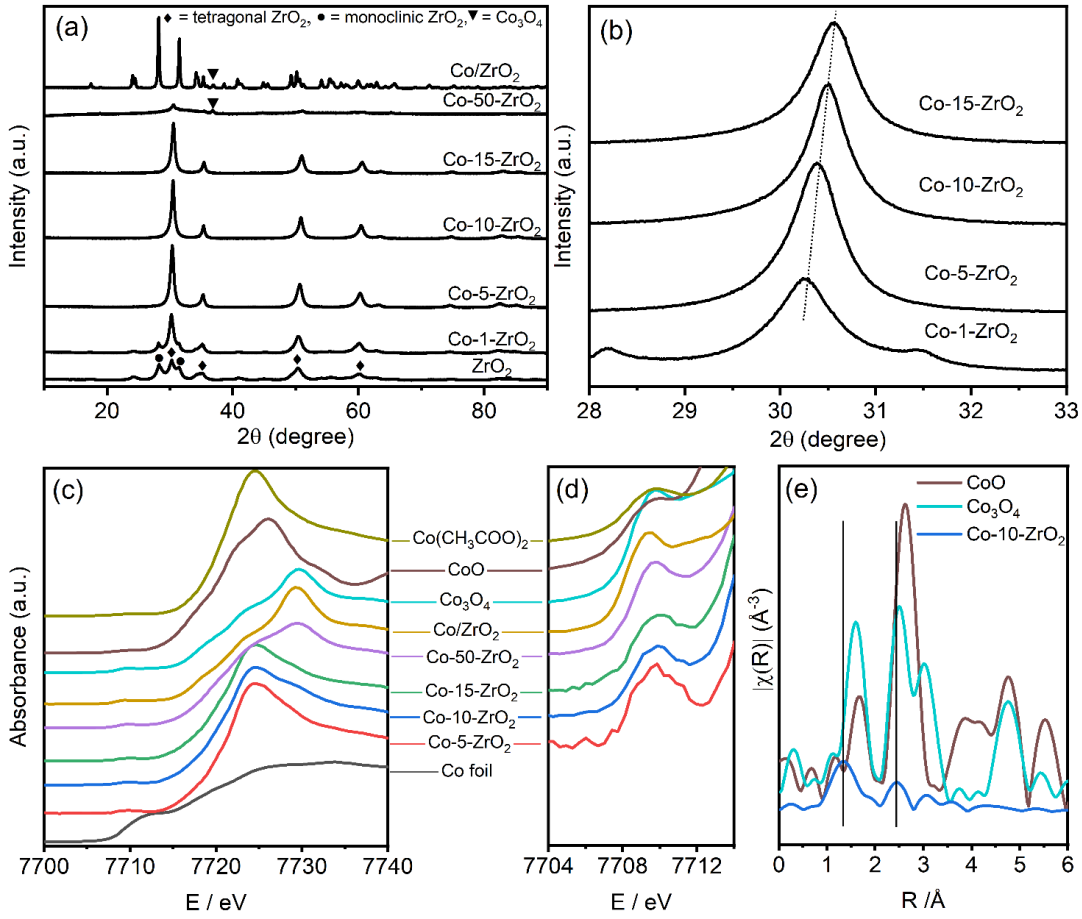

Figure 3.2: (a) XRD patterns of CO-X-ZrO_2 and Co/ZrO_2 catalysts. (b) Shifting of (101) plane of *t*-ZrO_2 as a result of doping of Co. (c) XANES spectrum of doped and impregnated catalysts along with standard Co compounds. (d) Expanded spectra showing the pre-edge region for Co XANES spectrum. (e) Fourier transform of EXAFS region for Co-10-ZrO_2 catalyst and reference Co oxides.

Table 3.1: Co-ordination number and radial distance for the first coordination sphere Co-O in Co-10-ZrO_2 in comparison to CoO, Co_3O_4 and Co-50-ZrO_2. S^2 = 0.83 which was determined by using FEFF.

Sample	N (corrected)	R (Å)	σ
CoO	6	2.12	0.078
Co_3O_4	6	1.94	0.054
Co-10-ZrO_2	2.4	1.88	0.06
Co-50-ZrO_2	4.4	1.92	0.066

Further characterization of Co-10-ZrO_2 catalyst and its comparison with impregnated catalyst was performed to understand the nature of the Co atoms in doped catalyst. Figure 3.3 shows the HAADF-STEM images of both the catalysts. For doped catalyst, a uniform crystal structure was observed, and Co particles or clusters were not observed (Figure 3.3a). Although atomic resolution was attained, single Co atoms were not observed because both Co and Zr appear with similar brightness owing to their similar atomic weight. In EDX mapping, homogeneous distribution of Co atoms was observed (Figure 3.3b, c). On the other hand, Co_3O_4 particles over ZrO_2 were observed for impregnated catalyst (Figure 3.3d). In this catalyst, Co atoms were confined to Co_3O_4 particle (Figure 3.3e, f).

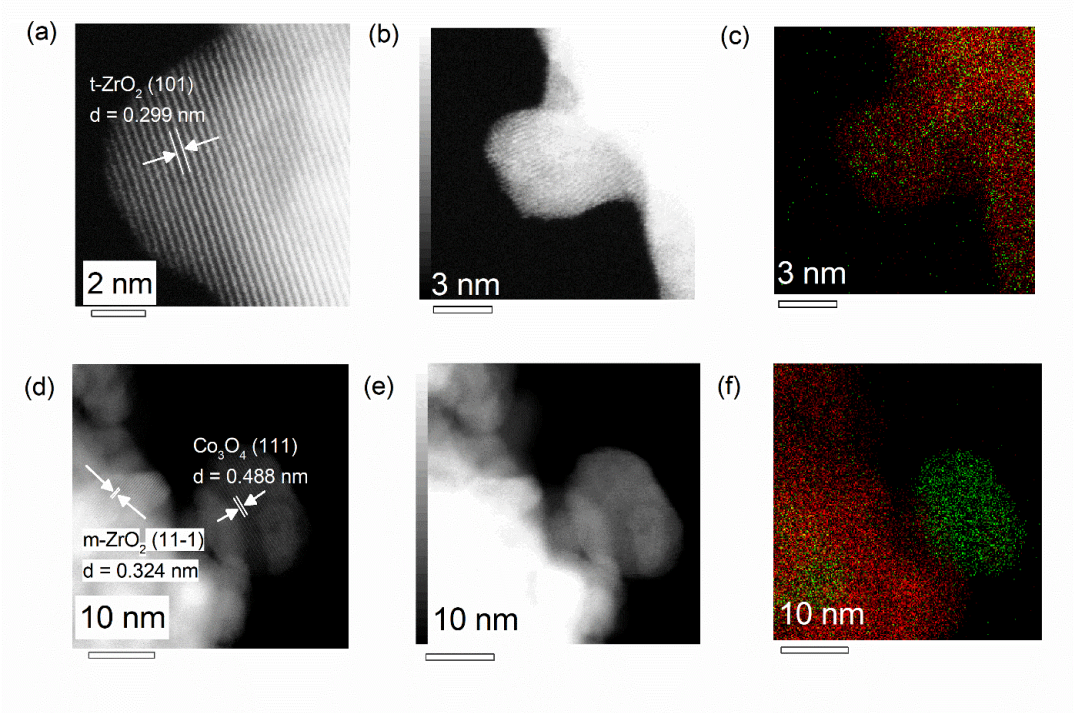

Figure 3.3: HAADF-STEM analysis of (a) Co-10-ZrO_2 and (d) Co/ZrO_2. EDX mapping of Co and Zr in Co-10-ZrO_2 (b,c) and (e,f) 10% Co/ZrO_2. Red and green colors in EDX mapping signify Zr and Co, respectively.

In the H_2-TPR analysis, pure ZrO_2 did not show any reduction feature due to its irreducible nature (Figure 3.4a). Impregnated Co/ZrO_2 catalysts showed two reduction

features owing to the presence of Co_3O_4 particles. The peak around 360 °C appeared because of the reduction of Co^{3+} to Co^{2+} and the peak around 540 °C was for reduction of Co^{2+} to Co^0. For doped Co-10-ZrO_2 catalyst, no prominent reduction feature was observed below 600 °C. Reduction features above 600 °C suggest the presence of highly dispersed Co species interacting strongly with the support.[25–26]

CO adsorption at room temperature using DRIFTS analysis after reducing the catalyst at 450 °C provided further information about the nature of Co species (Figure 3.4b). For both the doped and impregnated catalysts, broad peaks around 2174 and 2116 cm^{-1} were observed and assigned to gaseous CO.[27] Peaks at 2030 and 1973 cm^{-1} (shoulder) appeared for impregnated Co/ZrO_2 catalyst. These peaks were the characteristics of the adsorbed CO species in linear and bridging fashions over metallic Co.[28–31] No such peaks of adsorbed CO species were observed for doped Co-10-ZrO_2 catalyst because isolated Co atoms bound to oxygen atoms were known to have poor ability to bind CO.[32] These results confirmed the atomic dispersion of Co in doped catalyst.

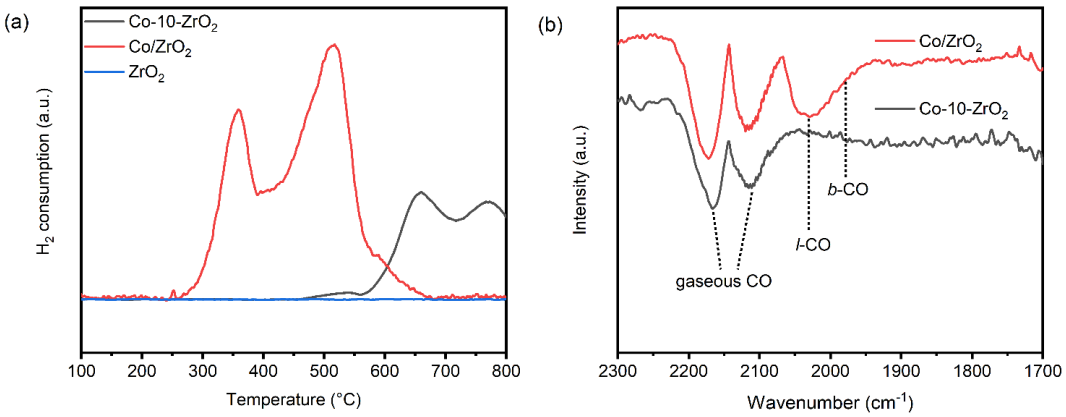

Figure 3.4: (a) H_2 TPR spectra of different catalysts. (b) CO DRIFTS over Co-10-ZrO_2 (black line) and Co/ZrO_2 (red line) showing gaseous CO and adsorbed CO in linear and bridge fashion (*l*-CO and *b*-CO respectively).

XPS analysis was carried out to understand the chemical environment around the Co atoms (Figure 3.5a). In Co 2p XPS analysis, $2p_{3/2}$ peak at 781.0 eV and satellite at 786.0 eV suggest the presence of Co^{2+} species.[33,34] The mismatch between oxidation states of Co^{2+} and Zr^{4+} created a charge imbalance in the crystal. This mismatch can be neutralized by creating oxygen vacancy near to Co atoms.[35] In O1s XPS spectra, the peak at 532 eV increased with increasing Co loading (Figure 3.5b). This peak ($O_{vacancy}$) was assigned as the oxygen atoms near oxygen vacancy site and oxygen atoms as O-H groups on the surface.[36,37] As shown in Chapter 2, CO_2 adsorption can be favorable over such oxygen vacancies. In the CO_2 TPD analysis (Figure 3.5c), the desorption feature in the low temperature region (100-300 °C) was assigned to physisorbed and weakly adsorbed CO_2 species. The desorption peak at 320 °C was assigned to chemisorbed CO_2 species. The intensity of this peak increased with increasing Co loading. Moreover, a linear co-relation was observed for increase in oxygen vacancy and chemisorbed CO_2 amount with increasing Co loading (Figure 3.5d). Therefore, it was concluded that doping of Co in ZrO_2 led to the formation of oxygen vacancy near Co atoms due to charge imbalance in the crystal structure. As a result, CO_2 chemisorption improved over the surface.

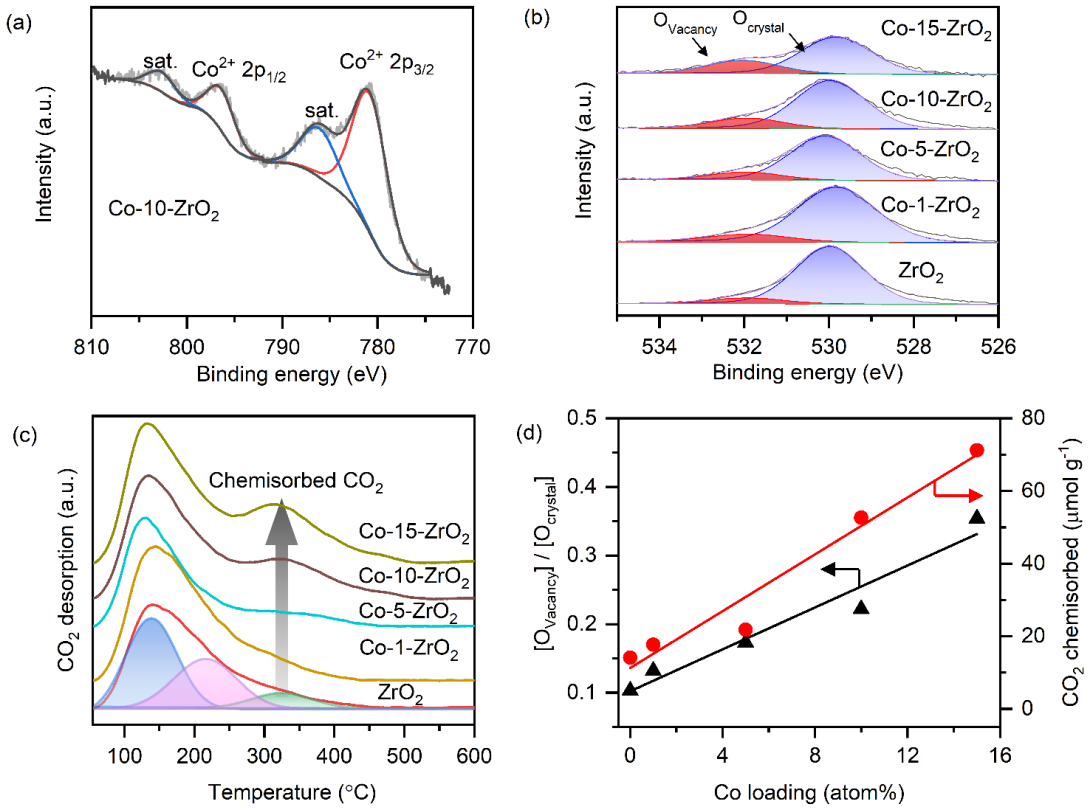

Figure 3.5: (a) Co 2p XPS spectrum for Co-10-ZrO_2 showing divalent nature of Co atoms after doping. (b) O1s XPS spectra for doped Co-X-ZrO_2 catalysts. (c) CO_2 TPD spectra showing increase in chemisorbed CO_2 amount at higher Co loading. (d) Correlation of Co loading with ratio of peaks in O1s XPS spectrum $[O_{vacancy}]/[O_{crystal}]$ and chemisorbed CO_2 amount, respectively.

3.3.2 Modeling the Co doped ZrO_2 surface and its interaction with CO_2

In order to understand the effect of Co doping on the generation of oxygen vacancy in ZrO_2 in more detail, DFT calculation was carried out. For doped catalysts, only *t*-ZrO_2 was observed in XRD and the 101 facet of *t*-ZrO_2 is reported to be the most stable one, both theoretically[38] and experimentally[39]. Therefore, the 101 facet of *t*-ZrO_2 was chosen as the computational model. Co doped ZrO_2 model was created by replacing one Zr of the top layer with Co atom.

Figure 3.6 shows the optimized structures of ZrO_2 and Co doped ZrO_2. As compared to perfect ZrO_2, the Co doped ZrO_2 without oxygen vacancy (Figure 3.6, Co-

ZrO_2) was slightly distorted. Zr atom on the surface of perfect ZrO_2 was coordinated with 7 O atoms whereas Co atom in Co-ZrO_2 was coordinated with 5 O atoms. This imbalance in co-ordination number between Co and Zr would likely create an oxygen vacancy. To simulate this, O atoms were removed from two possible sites, vo1 and vo2 (circled in Figure 3.6). The formation of oxygen vacancy over perfect ZrO_2 was endothermic while over Co-ZrO_2 it was exothermic. Over perfect ZrO_2, the formation energies of oxygen vacancies at the surface and subsurface layers were 3.20 eV and 2.7 eV respectively. The oxygen vacancy formation energy decreased to -1.17 eV and -1.45 eV for Co-ZrO_2_vo1 and Co-ZrO_2_vo2, respectively. Therefore, doped Co atoms strongly favored oxygen vacancy formation in ZrO_2. This observation is in line with experimental results.

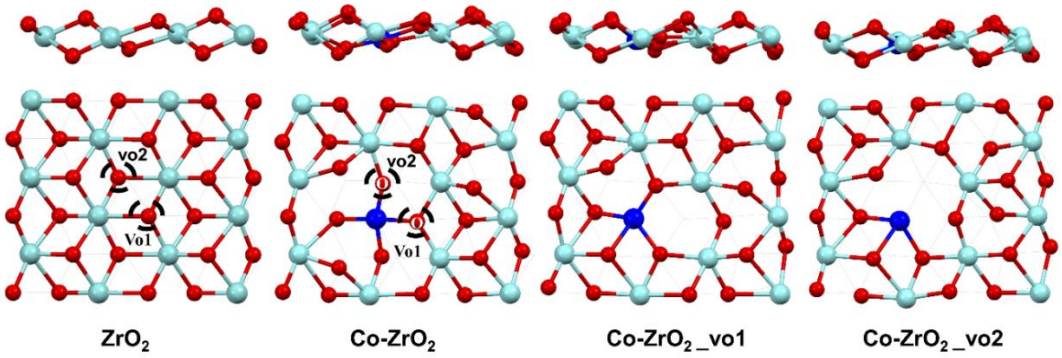

Figure 3.6: The side and top views for optimized ZrO_2 and Co-ZrO_2 surfaces with and without oxygen vacancies (denoted as Co-ZrO_2_v*x*, where *x* = o1, o2). The atoms at top layer and the second layer were represented by ball and stick, respectively. The other atoms were omitted for clarity. The dashed circle represents the position of oxygen vacancy. The Zr, O and Co atoms were represented in cyan, red and blue colors, respectively.

The influence of Co doping and the presence of oxygen vacancy on CO_2 adsorption was also investigated using DFT calculation. Two type of vacancies, Co-ZrO_2_vo1 and Co-ZrO_2_vo2 would competitively exist in the system as the formation

energies for both the vacancies were similar. Hence, both the geometries were considered for CO_2 adsorption study. The most stable geometries for CO_2 adsorption in linear and carbonate fashion are shown in Figure 3.7a and 3.7b, respectively. For linear adsorption, there was no significant change in adsorption energy for all models. On the other hand, CO_2 adsorption in carbonate fashion was more stable than linear fashion. Over perfect ZrO_2 surface, the carbonate formation energy was -0.62 eV. The stability did not increase in the presence of only Co atom without oxygen vacancy (Figure 3.7b, Co-ZrO_2, -0.25 eV). The formation energies of carbonate were decreased to -1.16 eV for Co-ZrO_2_vo1 and -1.37 eV for Co-ZrO_2_vo2. The C atom of CO_2 interacted with lattice oxygen and the two O atoms of CO_2 interacted with unsaturated metal atoms at the oxygen vacancy site. These results of improved CO_2 adsorption in presence of oxygen vacancy support the experimental results.

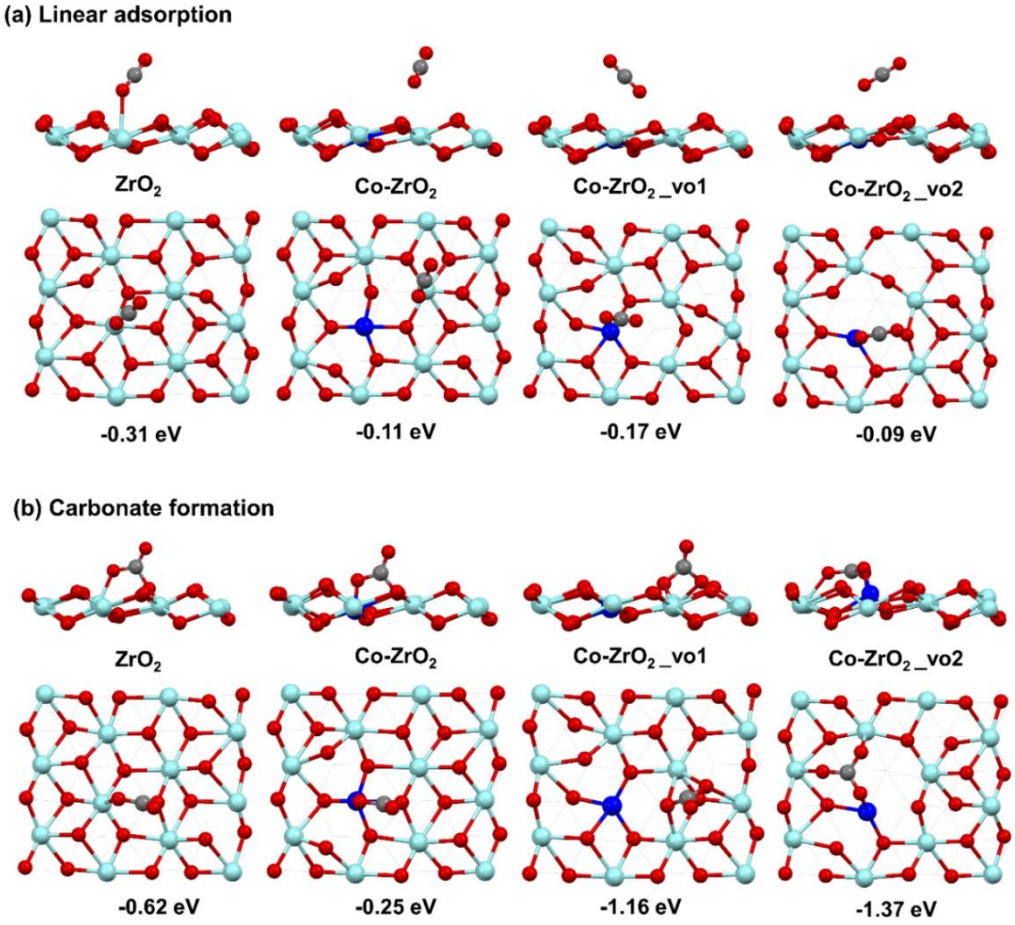

Figure 3.7: The most stable geometry for (a) linearly adsorbed CO_2 molecule and (b) formation of carbonate species on ZrO_2 and the surrounding of Co atom in Co-ZrO_2, Co-ZrO_2_vo1, and Co-ZrO_2_vo2. The atoms at top layer and the second layer were represented by ball and stick, respectively. The other atoms were omitted for clarity. The corresponding adsorption energies for CO_2 molecule is shown at the bottom of each geometry. The Zr, O, Co and C atoms were represented in cyan, red, blue and gray colors, respectively.

3.3.3 Catalytic activity for CO_2 hydrogenation

CO_2 hydrogenation activity of all catalysts was analyzed in a stainless-steel fixed bed reactor. In the presence of undoped ZrO_2, at 340 °C and 3 MPa, CO_2 conversion was 1.8% with 100% CO selectivity (Figure 3.8a). In case of doped catalysts, the activity increased with increasing Co loading without any significant drop in selectivity. Co-10-ZrO_2 showed the highest STY of CO of 3.8 μmol g^{-1} s^{-1} with 19% CO_2 conversion and 97% CO selectivity and the rest being methanol. Both Co-50-ZrO_2 and Co/ZrO_2 contained Co_3O_4 and produced methane as the main product. Therefore, catalysts with single atom Co in ZrO_2 network favored CO formation over methanol and methane.

The product selectivity was influenced by reaction temperature (Figure 3.8b). Methanol selectivity was increased at lower temperature because of the exothermic nature of the methanol formation reaction. At 280 °C, methanol selectivity was 29% along with 71% CO. CO formation was prominent at the temperature range of 300-360 °C. Methane started to form at 380 °C and at 420 °C, CO selectivity was 84% and methane selectivity was 16%. Introduction of Co single atoms to ZrO_2 crystal is prone towards methanol and CO formation at lower temperature while at higher temperature, methane was formed via total hydrogenation of CO_2.

The selectivity of CO was not influenced by any other reaction parameters such as pressure, space velocity and H_2 to CO_2 ratio. Under ambient pressure, the CO_2

conversion was 9.8% with 100% CO selectivity (Figure 3.8c). Changing the pressure to 4 MPa increased the conversion to 21% along with 96% CO selectivity. Similarly, changing the space velocity from 5000 to 60,000 mL h^{-1} g_{cat}^{-1} did not change the CO selectivity, which remained above 95% under all space velocity (Figure 3.8d). Changing the H_2 to CO_2 ration also did not change the selectivity (Figure 3.8e).

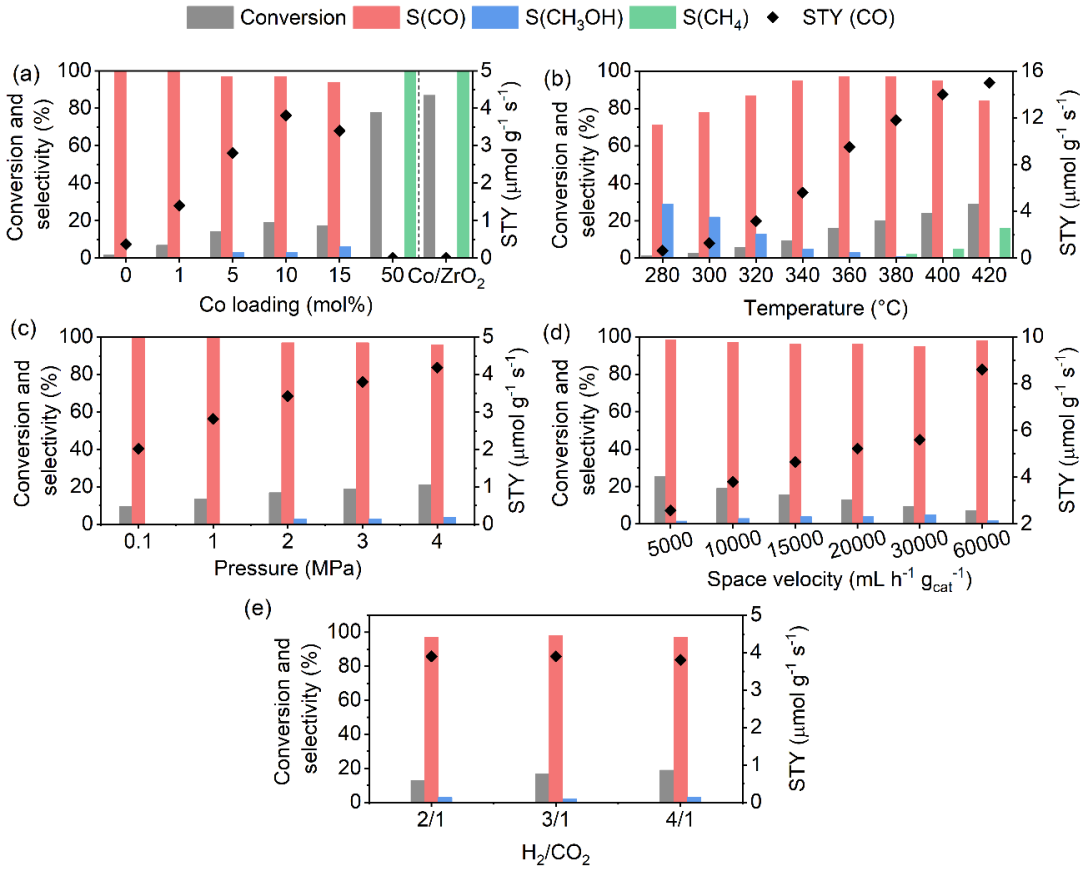

Figure 3.8: (a) Effect of Co loading on catalytic activity of doped (Co-X-ZrO_2) and impregnated catalysts (Reaction condition: 340 °C, 10,000 mL h^{-1} g^{-1}, 3 MPa, H_2:CO_2 = 4:1), (b) Effect of temperature (Reaction condition: 30,000 mL h^{-1} g^{-1}, 3 MPa, H_2:CO_2 = 4:1), (c) Effect of pressure (Reaction condition: 340 °C, 10,000 mL h^{-1} g^{-1}, H_2:CO_2 = 4:1), (d) Effect of space velocity (Reaction condition: 340 °C, 3 MPa, H_2:CO_2 = 4:1), (e) Effect of H_2 to CO_2 ratio (Reaction condition: 340 °C, 3 MPa, 10,000 mL h^{-1} g^{-1}) on the activity and product selectivity for Co-10-ZrO_2 catalyst.

The catalyst stability was checked for Co-10-ZrO_2 catalyst under the condition of 340 °C, 3 MPa and 10,000 mL h^{-1} g_{cat}^{-1} (Figure 3.9a). The catalytic activity was stable without drop in CO selectivity or CO_2 conversion. The XRD of used catalyst was same as the fresh one (Figure 3.9b). XPS spectra showed the presence of Co^{2+} and formation of Co^0 was not observed (Figure 3.9c). As a result, the relative percentage of oxygen vacancy remained similar in the used catalyst as compared to the fresh catalyst (18%) (Figure 3.9d). This was in accordance with H_2 TPR spectra (Figure 3.4a), which showed that Co species were not reduced at the temperature used for the reaction. This suggests the high stability of the catalyst.

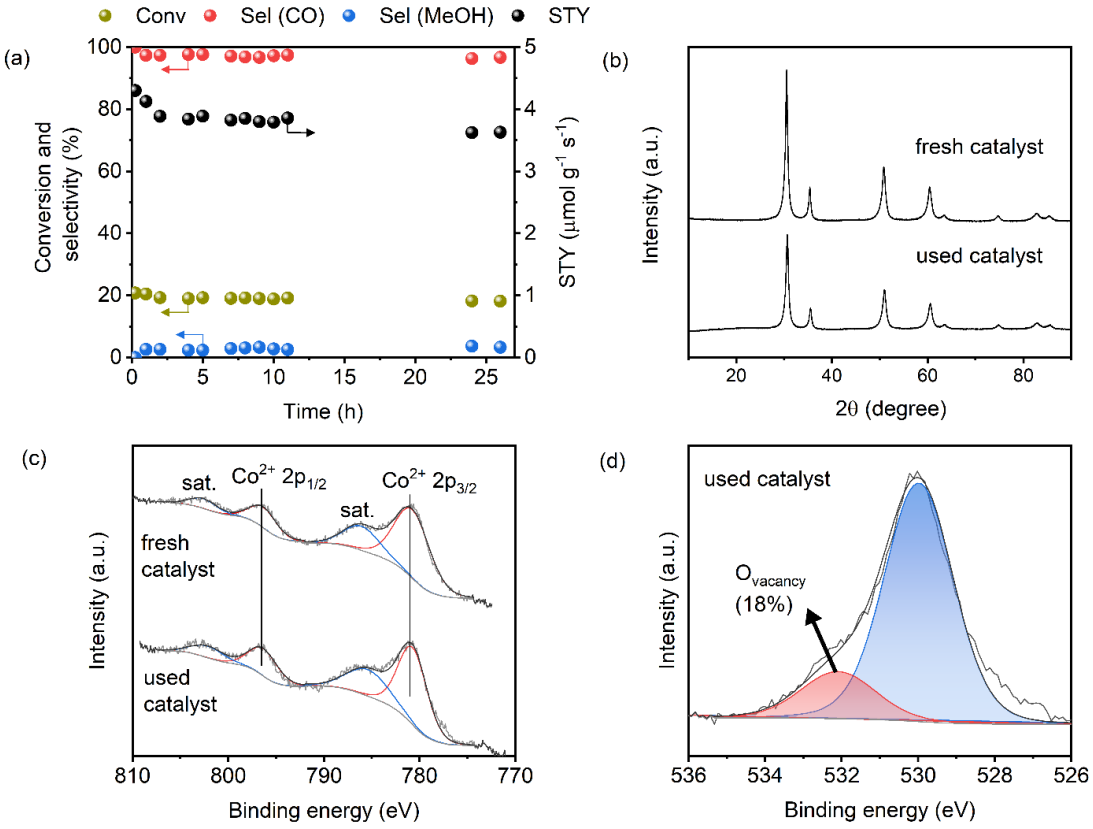

Figure 3.9: (a) Long-term reaction over Co-10-ZrO_2. Reaction condition: 340 °C, 3 MPa, 10,000 mL h^{-1} g^{-1}, H_2:CO_2 = 4:1, (b) XRD of fresh and used Co-10-ZrO_2 catalyst, (c) Co 2p XPS of fresh and used catalysts and (d) O 1s XPS of used Co-10-ZrO_2 catalyst.

3.3.4 Elucidation of mechanism and active site in doped catalyst

Operando DRIFTS analysis was carried out to understand the reaction mechanism. Co-10-ZrO_2 was pretreated under He at 280 °C for 30 minutes in the IR cell. After pretreatment, reactant gases (H_2:CO_2 = 4:1) were fed at 280 °C followed by stepwise increase in temperature. Several species were detected in DRIFTS spectra at 280 °C (Figure 3.10a). Peaks at 2972, 2882, 2740, 1585, 1384 and 1365 cm^{-1} were assigned as bidentate formate species ($HCOO^*$).[16,40–42] Peaks at 1632, 1221 cm^{-1} were assigned to bicarbonate species (HCO_3^*) and peaks around 1518, 1458, and 1423 cm^{-1} were assigned to carbonate species (CO_3^*).[42–44] At 300 °C, bicarbonate disappeared and carbonate species decreased, and formate increased. Formate was the dominant surface species at 340 °C. During IR measurement, CO formation was simultaneously analyzed by online GC (Figure 3.10b). CO formation rate was proportional to increase in formate species in IR as the temperature increased. Hence, it can be speculated that the formation of CO follows the formate pathway. It is worth mentioning that formate is also an intermediate for methanol formation.[45]

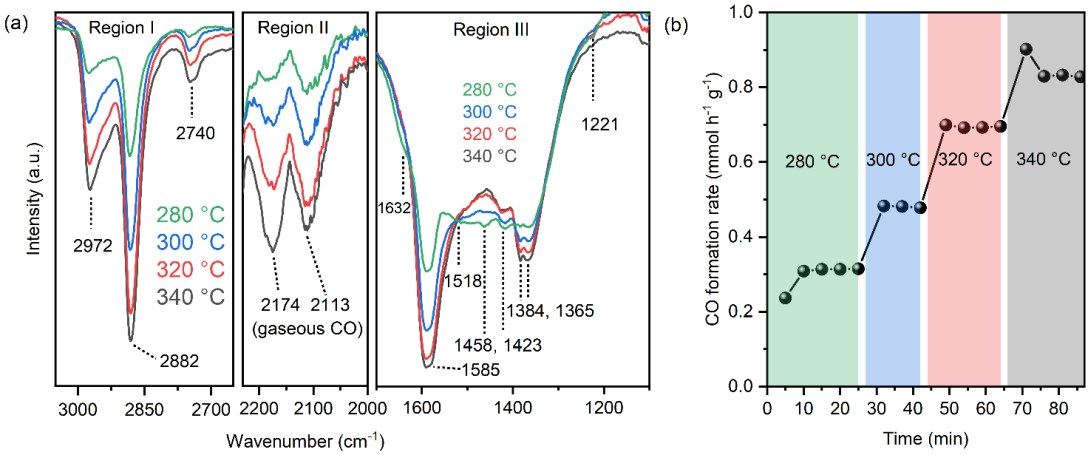

Figure 3.10: Operando DRIFTS experiment over Co-10-ZrO_2 catalyst. (a) IR spectrum recorded at different temperature. Three regions were shown where "Region I" shows the spectrum in the range of 3050-2650 cm^{-1} (showing formate species), "Region II" shows the range 2230-2000 cm^{-1} (showing gaseous CO) and "Region III" shows the range 1700-1100 cm^{-}

[1] (showing formate, bicarbonate and carbonate species). The y-axis scale is different for each region for clarity. (b) Formation rate of CO during the DRIFTS experiment. Reaction condition: 0.1 MPa, 280 – 340 °C, H_2:CO_2 = 4:1.

The following experiment was carried out to understand the relation between formate and CO formation. In the DRIFTS cell, a mixture of CO_2 and H_2 were flown over Co-10-ZrO_2 catalyst at 340 °C for 30 min. Gas flow was changed to He and the temperature was reduced rapidly to room temperature under He to retain all the species on the catalyst surface. After flushing for several minutes, the gas was changed to H_2 and the temperature was increased while recording the IR spectrum (Figure 3.11). Adsorbed species such as bicarbonates, carbonates reduced rapidly with increasing temperature (Figure 3.11a). In contrast, the intensity of the formate peak was stable until 300 °C. Above 300 °C, the formate peak intensity decreased fast. Methoxy species appeared in the temperature range of 100-300 °C (Figure 3.11b). When the same experiment was performed in TPD instrument, the evolution of CO gas started over 300 °C, which was consistent with formate decomposition (Figure 3.12). Formation of methoxy below 300 °C, rapid decomposition of formate above 300 °C along with formation of CO is in line with the selectivity pattern of products with temperature in Figure 3.8b. These experiments prove that formate was the intermediate for both CO and methanol formation.

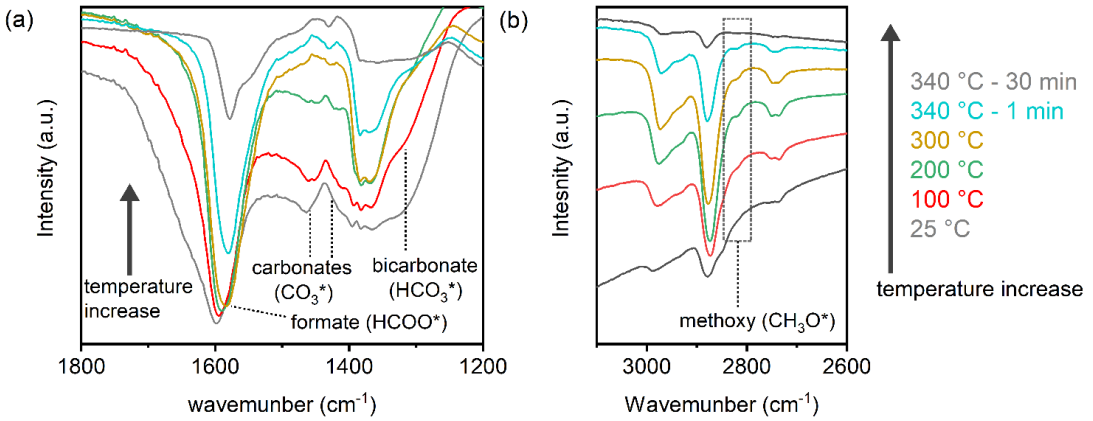

Figure 3.11: Evolution of different species (formed *in situ*) with temperature over Co-10-ZrO_2. (a) Evolution of formate along with carbonate and bicarbonate species and (b) evolution of methoxy species (shown in dotted box).

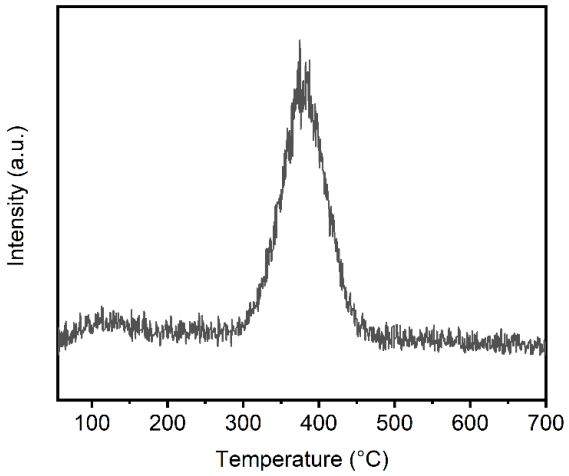

Figure 3.12: Mass profile of CO in TPD experiment of Co-10-ZrO_2 after pretreating the catalyst under reaction condition (340 °C, 0.1 MPa and H_2:CO_2 = 4:1).

To understand the nature of the active site capable of converting formate to CO, in situ DRIFTS spectra for Co-10-ZrO_2 and pure ZrO_2 were compared (Figure 3.13a). Pure ZrO_2 showed enough activity for CO formation that formate species were observed in IR spectra. Over ZrO_2 formate appeared at lower wavenumber (10-20 cm^{-1}) as compared to Co-10-ZrO_2. Formate is known to bond to two Zr atoms over ZrO_2 to form a stable structure (Zr-O-Zr like active site).[16,42,46] The increase in wavenumber of formate species over the surface of Co-10-ZrO_2 could be a result of bonding of one O

atom of formate with Co^{2+} instead of Zr^{4+} indicating an active site similar to Co-O-Zr for formate stabilization. Similar shifting has been reported when formate was stabilized at the interfacial site of In_2O_3/ZrO_2, where both In and Zr atoms were involved for formate stabilization.[47]

Figure 3.13b shows the evolution of CO gas during the decomposition of pre-adsorbed formic acid over ZrO_2 and Co-10-ZrO_2 surface. CO was the primary product during formic acid decomposition over both materials. For ZrO_2, one broad peak appeared at 350 °C. In contrast, two peaks appeared for Co-10-ZrO_2. The lower temperature peak at 325 °C (shown in red) was assigned to the formate decomposition over Co-O-Zr site whereas the higher temperature peak at 350 °C (shown in blue, same temperature for formate decomposition over ZrO_2) was assigned to the formate decomposition over Zr-O-Zr site. These experiments prove that, over the surface of Co doped ZrO_2, Co-O-Zr site is responsible for the stabilization of formate and its conversion to CO.

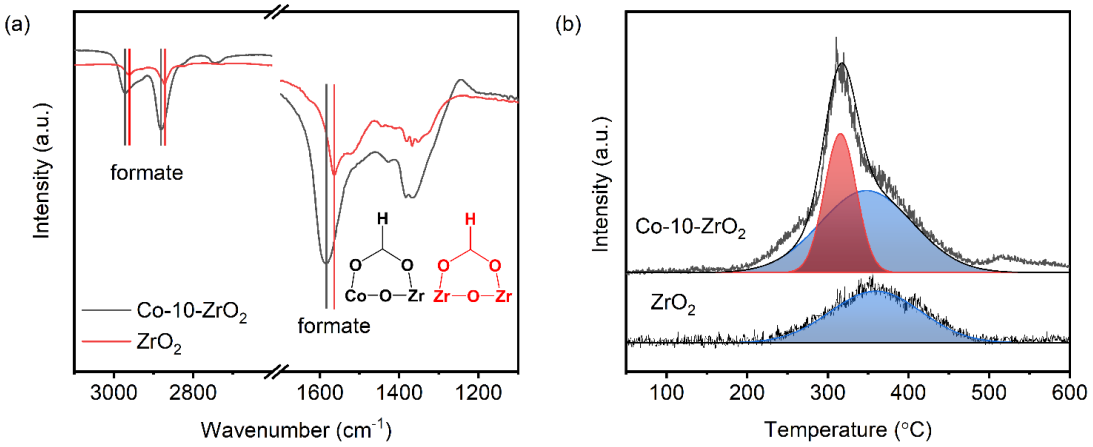

Figure 3.13: (a) Comparison of peak positions of formate species over Co-10-ZrO_2 and ZrO_2 during *in situ* DRIFTS study. Reaction condition: 340 °C, 0.1 MPa, H_2:CO_2 = 4:1. (b) Formic acid decomposition to CO over ZrO_2 and Co-10-ZrO_2. Red and blue regions showed the fitting for Co-10-ZrO_2.

In situ DRIFTS analysis was also carried out over impregnated Co/ZrO_2 catalyst (Figure 3.14a). The peak position of formate was at the same wavelength as for Co-10-ZrO_2 catalyst. Moreover, formate species did not form over impregnated Co/SiO_2 catalyst (Figure 3.14b). This suggests that, even in the impregnated Co/ZrO_2 catalyst, formate was able to form at the interfacial site of Co-O-Zr. Although formate formed at the interface over the impregnated catalyst, CO selectivity was low because of further hydrogenation of CO to methane over the metallic Co surface. Over the surface of Co-10-ZrO_2, subsequent hydrogenation of CO was not possible leading to high CO selectivity. On the other hand, CO was strongly adsorbed over the surface of impregnated catalyst and methane formation was favorable via CO hydrogenation. Adsorption of CO was only observed for impregnated catalyst containing metallic Co in DRIFTS analysis (Figure 3.4b).

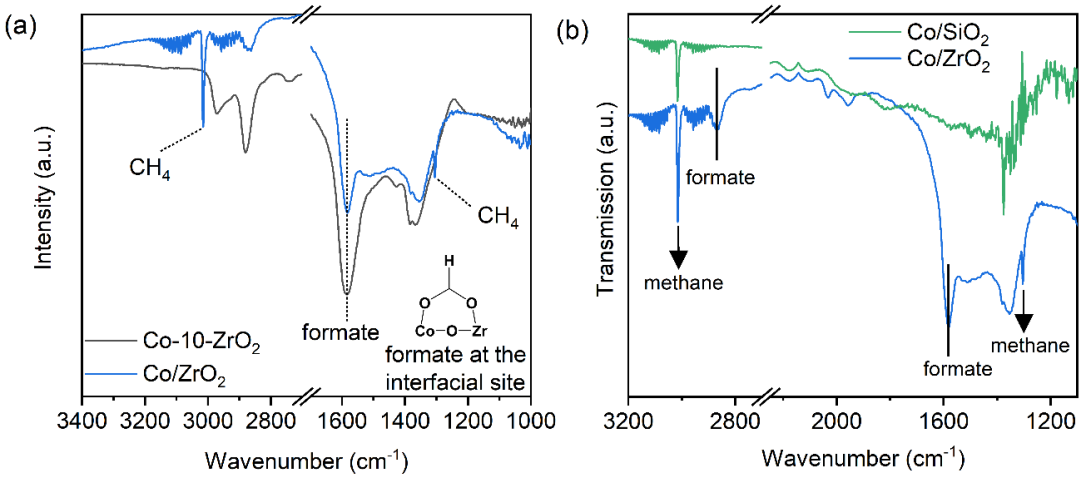

Figure 3.14: Comparison of *in situ* DRIFTS spectra over (a) Co-10-ZrO_2 and Co/ZrO_2 and (b) Co/ZrO_2 and Co/SiO_2. Reaction condition: 340 °C, 0.1 MPa, H_2:CO_2 = 4:1.

To understand the CO adsorption behavior of Co-10-ZrO_2 surface, DFT study was carried out. Figure 3.15 shows the optimized geometries of CO adsorption. Adsorption energies for CO on pure ZrO_2, Co-ZrO_2, Co-ZrO_2_vo1 and Co-ZrO_2_vo2 were calculated to be -0.62, -0.93, -0.53 and -0.82 eV, respectively. Although CO could

bind either to Zr or to Co atom, the adsorption over Co was favorable. On the surface of Co-ZrO_2 without oxygen vacancy (Figure 3.15, Co-ZrO_2), CO adsorption energy was -0.93 eV and CO_2 adsorption energy in carbonate mode was -0.25 eV (Figure 3.7b, Co-ZrO_2). Hence, without oxygen vacancy, CO adsorption is stronger than CO_2 adsorption, which would slow down the RWGS reaction and poison the active site. However, on the Co-ZrO_2 surface with oxygen vacancy, the CO adsorption energy was lower than CO_2 adsorption energy in carbonate mode (CO adsorption, Figure 3.15, Co-ZrO_2_ov1 and Co-ZrO_2_ov2 vs CO_2 adsorption, Figure 3.7b, Co-ZrO_2_ov1 and Co-ZrO_2_ov2). Therefore, in presence of oxygen vacancy, CO_2 would replace CO to make a way for the next catalytic cycle. Therefore, oxygen vacancy helps to prevent strong adsorption of CO over Co single atom.

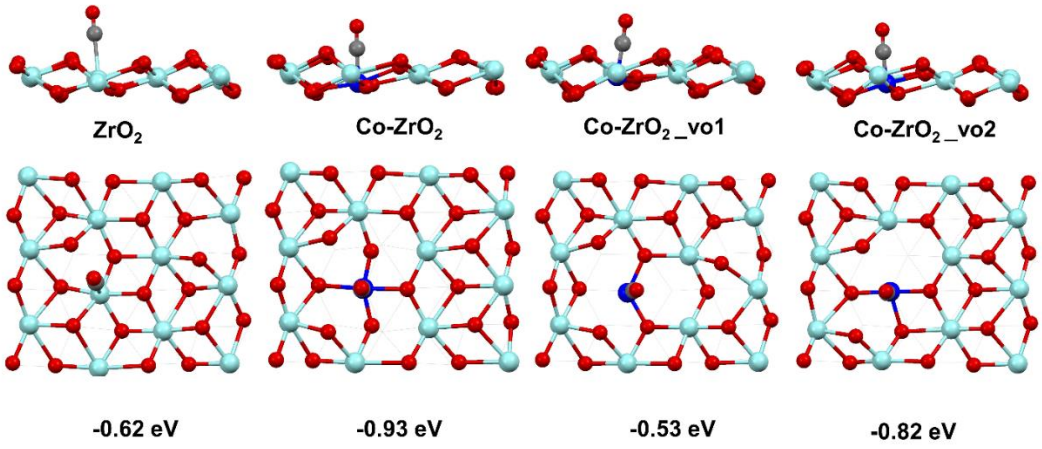

Figure 3.15: The most stable geometries for CO adsorption on ZrO_2, and Co-ZrO_2 surfaces. The atoms at top layer and the second layer were represented by ball and stick, respectively. The other atoms were omitted for clarity. The corresponding adsorption energies for CO molecule is shown at the bottom of each geometry. The Zr, O, Co and C atoms were represented in cyan, red, blue and gray colors, respectively.

Based on these observations, the following reaction mechanism for CO_2 hydrogenation over the surface of Co-10-ZrO_2 was proposed (Figure 3.16). Because of

doping of Co^{2+} in ZrO_2, oxygen vacancies are formed due to charge imbalance in the crystal lattice. The oxygen vacancy promotes CO_2 adsorption as carbonate species. Co single atom does H_2 dissociation followed by transfer of H to C of carbonate to form the formate species at the interfacial site. Selective decomposition of formate to CO occurs followed by removal of H_2O molecule. CO molecule does not undergo further hydrogenation because CO_2 replaces CO at the active site and the next cycle continues.

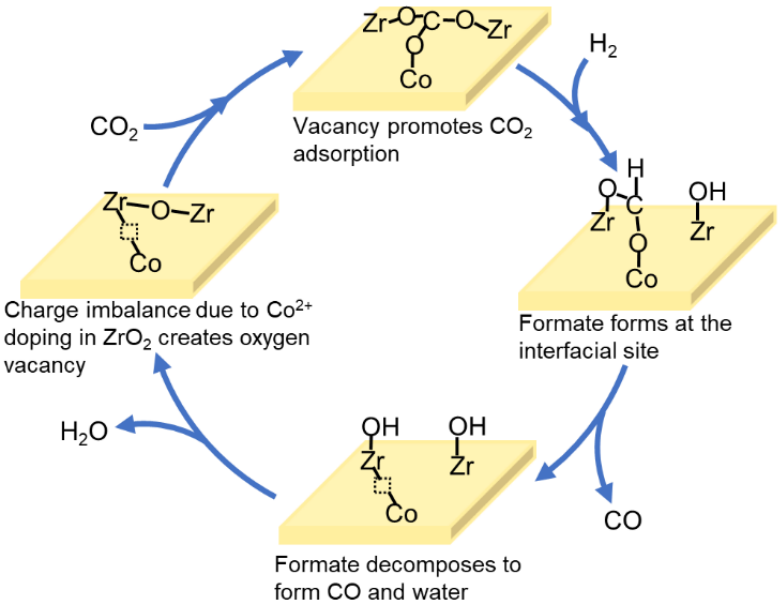

Figure 3.16: Schematic representation of reaction mechanism of CO formation from CO_2 over the Co doped ZrO_2 surface.

3.4 Conclusion

This chapter shows that single atom sites close to an oxygen vacancy can be active for CO formation from CO_2. Doping of cobalt in ZrO_2 catalysts created oxygen vacancies near Co atoms as a result of charge imbalance between Co^{2+} and Zr^{4+} in the ZrO_2 crystal. Doped catalysts containing Co single atom produced CO with selectivity more than 95%. In situ and operando DRIFTS analysis showed that formate was the intermediate for CO production. Atomically dispersed Co in association with neighboring Zr atom favored decomposition of formate to CO at temperatures above

300 °C. Presence of oxygen vacancy near Co single atom hampered the adsorption and further hydrogenation of CO leading to high CO selectivity. DFT calculations confirmed that Co doping in ZrO_2 leads to the formation of oxygen vacancies, which are necessary for CO_2 adsorption and formate formation.

References

1. J. Bao, G. Yang, Y. Yoneyama and N. Tsubaki, *ACS Catal.*, 2019, **9**, 3026–3053.
2. Y. Li, W. Gao, M. Peng, J. Zhang, J. Sun, Y. Xu, S. Hong, X. Liu, X. Liu, M. Wei, B. Zhang and D. Ma, *Nat. Commun.*, 2020, **11**, 1–8.
3. W. Z. Li, J. X. Liu, J. Gu, W. Zhou, S. Y. Yao, R. Si, Y. Guo, H. Y. Su, C. H. Yan, W. X. Li, Y. W. Zhang and D. Ma, *J. Am. Chem. Soc*, 2017, **139**, 2267–2276.
4. J. Qi, J. Finzel, H. Robatjazi, M. Xu, A. S. Hoffman, S. R. Bare, X. Pan and P. Christopher, *J. Am. Chem. Soc.*, 2020, **142**, 14178–14189.
5. S. Lyu, L. Wang, Z. Li, S. Yin, J. Chen, Y. Zhang, J. Li and Y. Wang, *Nat. Commun.*, 2020, **11**, 1–8.
6. J. Li, Y. He, L. Tan, P. Zhang, X. Peng, A. Oruganti, G. Yang, H. Abe, Y. Wang and N. Tsubaki, *Nat. Catal.*, 2018, **1**, 787–793.
7. P. Munnik, P. E. De Jongh and K. P. De Jong, *J. Am. Chem. Soc.*, 2014, **136**, 7333–7340.
8. W. Wang, S. Wang, X. Ma and J. Gong, *Chem. Soc. Rev.*, 2011, **40**, 3703–3727.
9. S. De, A. Dokania, A. Ramirez and J. Gascon, *ACS Catal.*, 2020, **10**, 14147–14185.
10. A. Jangam, S. Das, N. Dewangan, P. Hongmanorom, W. M. Hui and S. Kawi, *Catal. Today*, 2020, **358**, 3–29.
11. A. Parastaev, V. Muravev, E. Huertas Osta, A. J. F. van Hoof, T. F. Kimpel, N. Kosinov and E. J. M. Hensen, *Nat. Catal.*, 2020, **3**, 526–533.
12. S. Kattel, P. Liu and J. G. Chen, *J. Am. Chem. Soc*, 2017, **139**, 9739–9754.
13. J. Ye, C. Liu, D. Mei and Q. Ge, *ACS Catal.*, 2013, **3**, 1296–1306.
14. J. Wang, C. Tang, G. Li, Z. Han, Z. Li, H. Liu, F. Cheng and C. Li, *ACS Catal.*, 2019, **9**, 10253–10259.
15. Y. Wang, Z. Chen, P. Han, Y. Du, Z. Gu, X. Xu and G. Zheng, *ACS Catal.*, 2018, **8**, 7113–7119.
16. J. Wang, G. Li, Z. Li, C. Tang, Z. Feng, H. An, H. Liu, T. Liu and C. Li, *Sci. Adv.*, 2017, **3**, 1–11.
17. S. Brunauer, P. H. Emmett and E. Teller, *J. Am. Chem. Soc*, 1938, **60**, 309–319.

18. Y. Wasawa, Ed., X-ray absorption fine structure for catalysis and surfaces, World Scientific, 1996.
19. J. J. Rehr and R. C. Albers, *Rev. Mod. Phys.*, 2000, **72**, 621–654.
20. B. Ravel and M. Newville, *J. Synchrotron Radiat.*, 2005, **12**, 537–541.
21. J. P. Perdew, K. Burke and M. Ernzerhof, *Phys. Rev. Lett.*, 1996, **77**, 3865–3868.
22. G. Kresse and J. Furthmüller, *Phys. Rev. B - Condens. Matter Mater. Phys.*, 1996, **54**, 11169–11186.
23. G. Teufer, *Acta Crystallogr.*, 1962, **15**, 1187–1187.
24. R. D. Shannon, *Acta Crystallogr. Sect. A*, 1976, **32**, 751–767.
25. H. Zhao and H. Lu, *React. Kinet. Catal. Lett.*, 2009, **97**, 289–293.
26. J. G. Chen and Y. H. Sun, *Stud. Surf. Sci. Catal.*, 2004, **147**, 277–282.
27. W. Li, Y. Liu, M. Mu, F. Ding, Z. Liu, X. Guo and C. Song, *Appl. Catal. B Environ.*, 2019, **254**, 531–540.
28. D. Song, J. Li and Q. Cai, *J. Phys. Chem. C*, 2007, **111**, 18970–18979.
29. N. Kumar, K. Jothimurugesan, G. G. Stanley, V. Schwartz and J. J. Spivey, *J. Phys. Chem. C*, 2011, **115**, 990–998.
30. J. Scalbert, I. Clémençon, P. Lecour, L. Braconnier, F. Diehl and C. Legens, *Catal. Sci. Technol.*, 2015, **5**, 4193–4201.
31. J. A. Singh, N. Yang, X. Liu, C. Tsai, K. H. Stone, B. Johnson, A. L. Koh and S. F. Bent, *J. Phys. Chem. C*, 2018, **122**, 2184–2194.
32. K. Khivantsev, A. Biancardi, M. Fathizadeh, F. Almalki, J. L. Grant, H. N. Tien, A. Shakouri, D. A. Blom, T. M. Makris, J. R. Regalbuto, M. Caricato and M. Yu, *ChemCatChem*, 2018, **10**, 736–742.
33. D. Lee, Q. X. Xia, J. M. Yun and K. H. Kim, *Appl. Surf. Sci.*, 2018, **433**, 16–26.
34. K. Hadjiivanov, V. Avreyska, G. Tzvetkov, P. Stefanov, C. Chupin, C. Mirodatos and T. S. Marinova, *Surf. Interface Anal.*, 2001, **32**, 175–178.
35. S. Jiang, R. Zhang, H. Liu, Y. Rao, Y. Yu, S. Chen, Q. Yue, Y. Zhang and Y. Kang, *J. Am. Chem. Soc*, 2020, **142**, 18.
36. Y.-X. Pan, C.-J. Liu, D. Mei and Q. Ge, *Langmuir*, 2010, **26**, 5551–5558.
37. V. P. Indrakanti, J. D. Kubicki and H. H. Schobert, in *Fuel Process. Technol.*, 2011, **92**, 805–811.
38. W. Xia, F. Wang, L. Wang, J. Wang and K. Chen, *Catal. Letters*, 2020, **150**, 150–158.
39. H. Y. T. Chen, S. Tosoni and G. Pacchioni, *J. Phys. Chem. C*, 2015, **119**, 10856–10868.
40. C. Schild, A. Wokaun and A. Baiker, *J. Mol. Catal.*, 1990, **63**, 243–254.
41. I. A. Fisher and A. T. Bell, *J. Catal.*, 1997, **172**, 222–237.
42. K. Pokrovski, K. T. Jung and A. T. Bell, *Langmuir*, 2001, **17**, 4297–4303.

43. E. M. Köck, M. Kogler, T. Bielz, B. Klötzer and S. Penner, *J. Phys. Chem. C*, 2013, **117**, 17666–17673.
44. K. D. Dobson and A. J. McQuillan, *Langmuir*, 1997, **13**, 3392–3396.
45. S. Kattel, B. Yan, Y. Yang, J. G. Chen and P. Liu, *J. Am. Chem. Soc.*, 2016, **138**, 12440–12450.
46. S. T. Korhonen, M. Calatayud and A. Outi I Krause, *J. Phys. Chem. C*, 2008, **112**, 16096–16102.
47. T. Y. Chen, C. Cao, T. B. Chen, X. Ding, H. Huang, L. Shen, X. Cao, M. Zhu, J. Xu, J. Gao and Y. F. Han, *ACS Catal.*, 2019, **9**, 8785–8797.

Chapter 4

Role of support in controlling CO_2 hydrogenation pathway

Abstract

It is clear from Chapters 2 and 3 that both the nature of dopant and the nature of support/host oxide can influence the CO_2 hydrogenation activity and selectivity. In order to understand the role of the support in doped metal oxides, this chapter focuses on the designing indium doped mixed oxides with different supports. Two doped oxides, In-ZrO_2 and In-TiO_2, were prepared and the effect of the support was studied. It was found that the presence of Zr and Ti at the active site could control the mechanism and selectivity of CO_2 hydrogenation. In-ZrO_2 produced methanol as the major product, while In-TiO_2 produced CO as the only product. In-ZrO_2 followed formate pathway for methanol discussed in Chapter 2. However, CO production on In-TiO_2 followed redox mechanism without the involvement of any intermediate. This change in selectivity and mechanism was dictated by the reducible nature of the support.

4.1 Introduction

Support plays an important role in heterogeneous catalysis. In addition to stabilizing metal nanoparticles on the surface, support also helps in the formation of interfacial active sites, induces change in electronic property of metals via electronic charge transfer, and helps in the adsorption of substrate and intermediates.[1-9] Therefore, tuning the properties of support is an effective way to control activity and selectivity of reactions having complex mechanism such as CO_2 hydrogenation (Scheme 1.1, Chapter 1).[1]

In CO_2 hydrogenation, support plays a prominent role in adsorption/desorption behavior of intermediate species. For example, changing the support from TiO_2 to CeO_2 or ZrO_2 increased the adsorption of C,O-bound species (for example: CO_2^*, $HOCO^*$) and O-bound species (for example: $HCOO^*$ and CH_3O^*) at the interfacial sites of PtCo bimetallic nanoparticle and as a result, the selectivity changes from CO to CH_4.[9] When ZnO was used as support for Cu based catalysts for CO_2 hydrogenation, ZnO stabilized formate species as intermediate for methanol production.[10,11] In contrast, when TiO_2 or ZrO_2 was used as support, the active sites were poisoned because of over stabilization of formate species.[12,13] This chapter investigates the role of support as an integral part of the active site for CO_2 hydrogenation over In based catalysts.

For In_2O_3 catalyst, In-V_o-In (V_o = oxygen vacancy) has been suggested as the active site, which can strongly adsorb CO_2 and can stabilize the formate intermediate.[4] Only ZrO_2 support has been reported to promote the stability and the activity of In_2O_3.[14] Several studies have investigated the reasons for promotional effect of ZrO_2. Ramirez et al. proposed the generation of oxygen vacancy over the surface of In_2O_3 because of the mismatch between crystal structures of In_2O_3 (cubic) and ZrO_2 (monoclinic).[15] Another reasoning is that electronic transition from ZrO_2 to In_2O_3 improved the oxygen

vacancy formation.[16] Muller et al. showed that a solid solution between In and Zr is formed because of the disintegration of In_2O_3 over the surface of ZrO_2 and promoted methanol formation.[17] In contrast, Han et al. drew an opposite conclusion that interfacial site of In and Zr was active for CO formation via formate decomposition.[18] Therefore, the behavior of interfacial site between indium and support material remains elusive.

This chapter shows that CO_2 hydrogenation selectivity and pathway at the interfacial site of indium and support material was controlled by the nature of the support material. Two catalysts, indium doped ZrO_2 and TiO_2 (In-ZrO_2 and In-TiO_2) were prepared, and the effect of the support was studied. ZrO_2 and TiO_2 were chosen because they are widely used in CO_2 hydrogenation and they are distinct in terms of their reducibility. The In-ZrO_2 produced methanol as the major product and In-TiO_2 showed CO as the only product. Presence of ZrO_2 promoted formate formation over the surface while TiO_2 favored redox mechanism without involving any reaction intermediate.

4.2 Experimental method

4.2.1 Catalyst Preparation

Indium nitrate ($In(NO_3)_3 \cdot 3H_2O$), zirconyl nitrate ($ZrO(NO_3)_2 \cdot 2H_2O$), aqueous titanium chloride solution (aqueous solution of 20% $TiCl_3$ containing 5% HCl) and citric acid were purchased from Fujifilm Wako Pure Chemical Corporation. Indium doped catalysts were prepared using a sol-gel method in the presence of citric acid. A typical procedure to obtain In-ZrO_2 and In-TiO_2 catalysts is as follows: $In(NO_3)_3 \cdot 3H_2O$ (1 mmol) and $ZrO(NO_3)_2.2H_2O$ (9 mmol) or $TiCl_3$ (9 mmol) solution were added to a beaker containing 60 mL of H_2O along with 10 mmol of citric acid. The beaker was placed on a hot plate maintained at 150 °C and stirred until a foaming gel was formed.

The gel was then dried in an oven maintained at 150 °C for 5 h. The resulting composite was crushed and calcined at 500 °C for 3 h (ramp rate: 2 °C min^{-1}) to obtain the final catalyst. In both the catalysts, the indium metal content was kept 10 atom% with respect to total metal content [In /(In + Zr (Ti)) = 0.1].

4.2.2 Catalyst characterization

XRD was measured with Rigaku MiniFlex using CuKα X-ray (λ = 1.54 Å) operating at 40 kV and 20 mA. XPS was performed with JEOL JPS-9010MC instrument. Charge correction was made by adjusting the external carbon peak to 284.6 eV. H_2 TPR of catalysts were carried out in presence of H_2-Ar mixture (H_2 = 5%) in a BELCAT II instrument equipped with a TCD detector. Prior to measurement, catalysts were pretreated at 200 °C for 1 hour under Ar flow. Measurements were done at a total flow rate of 50 mL min^{-1} with ramp rate of 10 °C min^{-1}. CO_2 TPD expreminet was performed in the BELCAT II instrument. Prior to measurement, the samples were pretreated with He at 200 °C for 1 h. The sample was then cooled to room temperature and then CO_2 was used to purge the sample sell for 30 min followed by He flow for another 30 min. In TPD analysis under He flow, temperature was increased by 10 °C min^{-1}. For formic acid TPD, formic acid was first impregnated on the catalyst in a hexane solution followed by washing with hexane to remove the physisorbed formic acid and was dried at room temperature. The TPD analysis was carried out under He flow and temperature was increased by 10 °C min^{-1}. DRIFTS were recorded in a Perkin Elmer Spectrum 100 FTIR spectrometer equipped with MCT detector cooled with liquid N_2. The catalyst was first pretreated in He at 300 °C for 30 min. One spectrum was recorded for only catalyst. Next, the reactant gases started to flow (H_2:CO_2 = 4) and specta were recorded with different time interval. Final spectrum of the adsorbed species was yielded after correction with the spectrum of only catalyst.

4.2.3 Evaluation of catalytic activity

Catalytic activity for CO_2 hydrogenation was evaluated in a stainless-steel packed bed flow reactor system (Figure 2.1, Chapter 2). Products were analyzed using an online GC (Shimadzu, GC 8A) equipped with two columns – Porapak Q and Molecular Sieve and a TCD detector. Gas line from the outlet of the reactor to the inlet of the GC was heated at 150 °C to prevent condensation. Typically, 200 mg of catalyst was loaded into the reactor and held in place by quartz wool. A thermocouple was inserted into the reactor to measure catalyst bed temperature. Prior to reaction, the catalyst was pretreated under 0.5 MPa Ar for 1 h at 300 °C. Then the reactor was cooled to 50 °C under Ar and pressurized to reaction condition using a mixture of H_2 and CO_2 having the ratio H_2:CO_2 = 4:1. After the system pressure was stable, reactor temperature was increased to desired value. Total flow rate was 100 mL min^{-1} to maintain space velocity at 25,000 mL h^{-1} g^{-1}. CO_2 conversion, selectivity of CO, CH_3OH and CH_4, space time yield (STY) of CH_3OH and CO were calculated using Equations 2.1 to 2.5 stated in Chapter 2.

4.3 Results and discussions

4.3.1 Catalytic activity

Catalytic activity of doped and pure oxides was checked at 300 °C, 5 MPa and 25,000 mL h^{-1} g_{cat}^{-1} space velocity (SV) (Figure 4.1). Pure In_2O_3 showed methanol selectivity of 74% and CO selectivity of 24% along with small amount of methane (2%) (Figure 4.1a). In-ZrO_2 catalyst produced methanol with a selectivity of 59%. CO selectivity was 37% and rest was methane (4%). In contrast, CO was the only product in the presence of In-TiO_2. CO_2 conversion over pure ZrO_2 and TiO_2 was negligible. This result indicates that catalytic activity of In-M_xO_y (M_xO_y = ZrO_2 and TiO_2) catalysts was derived from the indium doping while the reaction mechanism depended on the

nature of the support. The doped oxide catalysts showed higher activity in both CO and methanol formation than pure In_2O_3 (Figure 4.1b).

Methanol synthesis from CO_2 is exothermic and RWGS reaction is endothermic in nature. Therefore, reaction temperature can influence the selectivity of these products. In the presence of In-ZrO_2, methanol selectivity increased at lower temperatures as expected (Figure 4.1c). Although methanol remained as major product over In-ZrO_2, the methanol selectivity was lower than that over pure In_2O_3. However, in the presence of In-TiO_2, CO was the only product at all temperatures investigated.

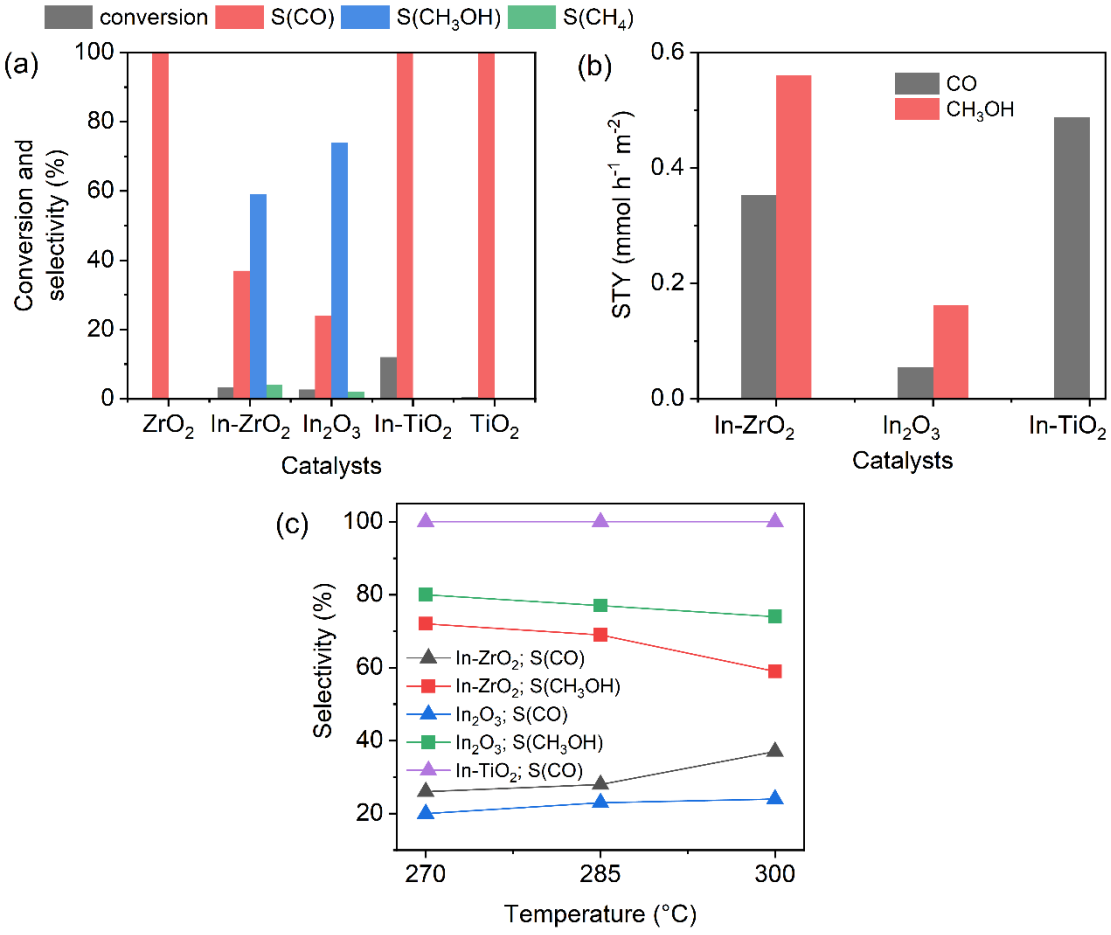

Figure 4.1: (a) Conversion of CO_2 and selectivity of products during CO_2 hydrogenation. (b) STY of products over In-M_xO_y (M_xO_y = ZrO_2 and TiO_2) and their pure oxides. Reaction condition: 300 °C, 5 MPa and 25,000 mL h^{-1} g_{cat}^{-1} SV, H_2:CO_2 = 4:1. (c) Selectivity of products at different temperatures. Reaction condition: 5 MPa and 25,000 mL h^{-1} g_{cat}^{-1} SV, H_2:CO_2 = 4:1.

4.3.2 Catalyst structure

Figure 4.2a shows the XRD pattern of In-ZrO_2 catalyst. Pure ZrO_2 showed the presence of both monoclinic and tetragonal phase. After indium doping, only tetragonal phase was present because dopants stabilize tetragonal phase of ZrO_2 as observed in Chapter 3. The peak position of tetragonal ZrO_2 in In-ZrO_2 catalysts were shifted towards higher 2θ value because of incorporation of smaller In^{3+} (0.80 Å) ion in place of Zr^{4+} (0.84 Å) ion.[20–22] Upon doping with a smaller ion, the interplanar distance (d spacing) decreases and 2θ value increases. In case of In-TiO_2 catalyst, the predominant phase was anatase TiO_2 (Figure 4.2b). After doping of In, the peak position for 101 plane of anatase TiO_2 shifted to lower value owing to incorporation of larger In^{3+} (0.80 Å) ions in the crystal of TiO_2 (Ti^{4+} = 0.60 Å).[22] These shifting in the peak position indicated that in both In-ZrO_2 and In-TiO_2 catalysts, indium species are highly dispersed throughout the crystal system. Furthermore, in the TEM images only the tetragonal ZrO_2 and anatase TiO_2 crystals were observed and crystal phase for pure In_2O_3 was not detected (Figure 4.2c and 4.2d).

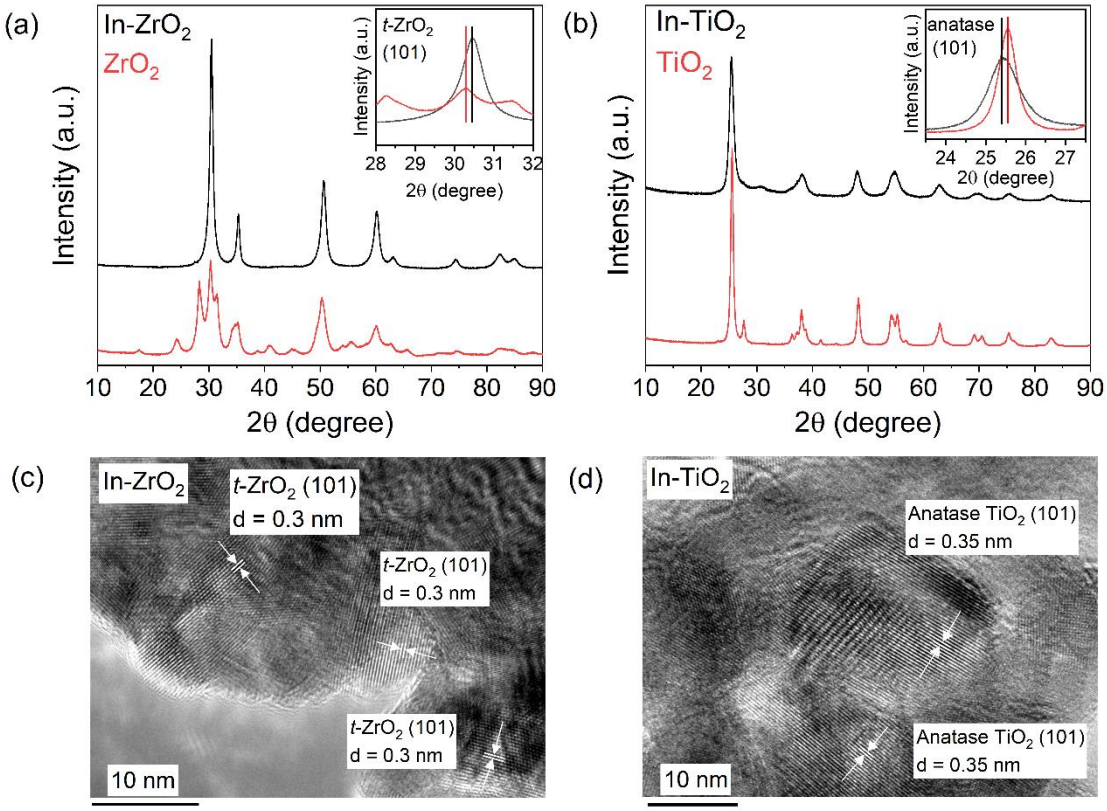

Figure 4.2: XRD patterns of (a) In-ZrO_2 and (b) In-TiO_2 catalysts. TEM images showing the d spacing (c) In-ZrO_2 and (d) In-TiO_2.

4.3.3 Surface properties

The reducibility of In-M_xO_y catalysts were examined by H_2 TPR (Figure 4.3). Pure ZrO_2 did not show any reduction feature because of its irreducible nature, whereas In-ZrO_2 showed one prominent peak around 700 °C (Figure 4.3a). This peak appeared because of the complete reduction of indium species.[14] However, consumption of hydrogen started from 300 °C, which was interpreted as formation of surface oxygen defects adjacent to In atoms without total reduction of In. Similarly, surface of pure TiO_2 partially reduced at around 600 °C (Figure 4.3b).[23,24] Whereas, reduction features were observed at a much lower temperature for In-TiO_2, indicating high reducibility of the catalyst. Therefore, indium species in In-TiO_2 catalysts were more reducible under reaction condition than in In-ZrO_2 catalyst.

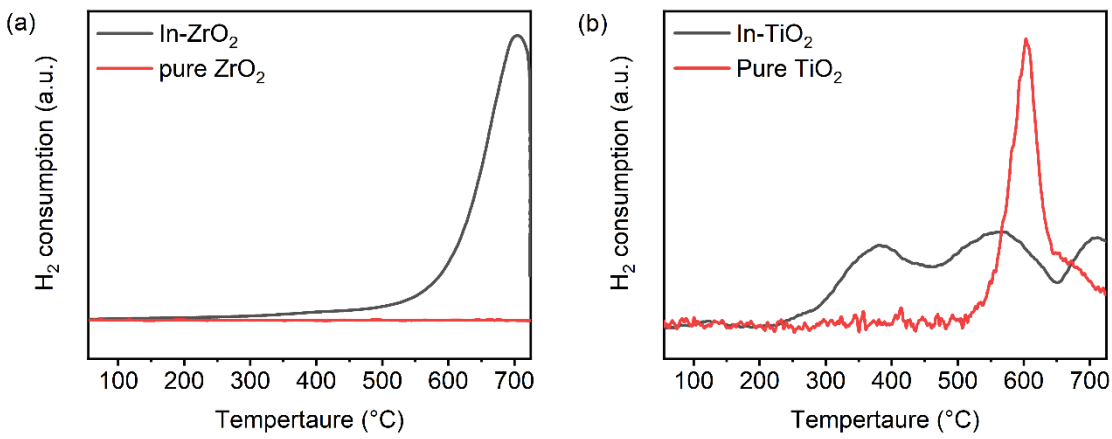

Figure 4.3: H_2 TPR analysis for (a) In-ZrO_2 and (b) In_2-TiO_2 catalyst.

The chemical environment on the surface of the two catalyst was probed by XPS. The O 1s XPS spectra for In-ZrO_2 are shown in Figure 4.4a. The peak at 529.7 eV indicates the presence of crystal oxygen and the shoulder peak at 531.9 eV is termed as defective oxygen, which is assigned to surface -OH species and O atoms near vacancies. In used In-ZrO_2 catalyst, the amount of oxygen defects increased. This was primarily attributed to formation of -OH species because the elemental state of In and Zr species did not change after the reaction (Figure 4.4b, c). For In-TiO_2 catalyst, the oxygen defect sites increased slightly after the reaction (Figure 4.4d). The In 3d XPS spectra for fresh and used In-TiO_2 catalysts showed the formation of reduced In species at 443.9 eV, which is in between the expected peak position for In^{3+} and In^0 (Figure 4.4e).[25] Similarly, in the Ti 2p XPS spectra, presence of Ti^{3+} at 458 eV in used catalyst was observed (Figure 4.4f).[26,27] This suggests that under the reaction condition, both In^{3+} and Ti^{4+} were reduced, which corroborates with the H_2 TPR analysis.

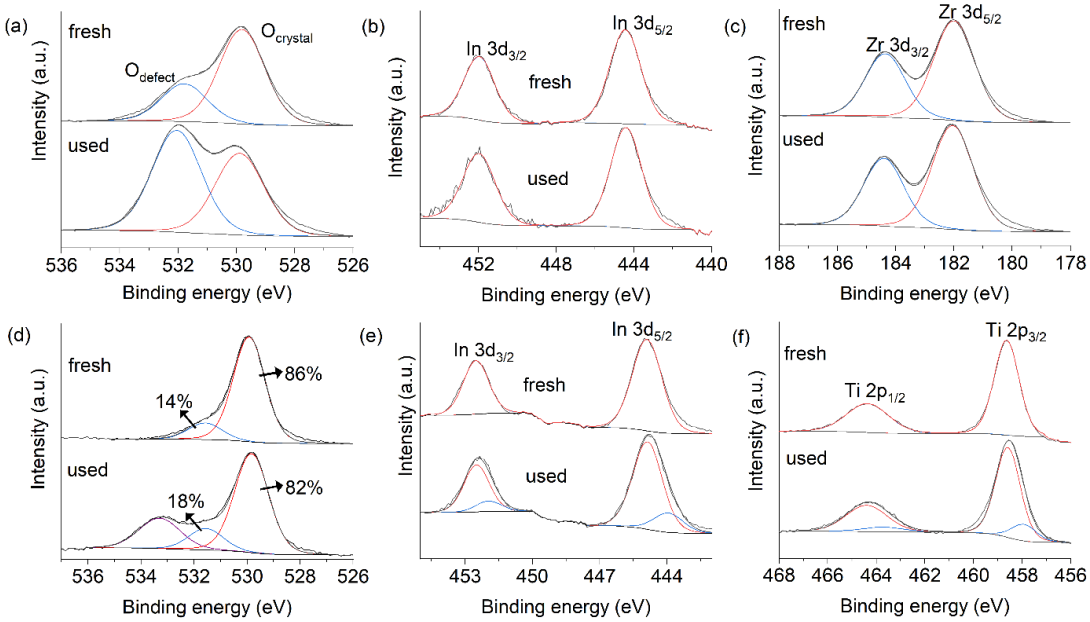

Figure 4.4: XPS analysis of In-ZrO_2 (a-c) and In-TiO_2 (d-f) catalysts.

CO_2 TPD analysis was carried out to understand the CO_2 adsorption behavior on the surface of catalysts. Two desorption features were observed for In-ZrO_2 (Figure 4.5a). DRIFTS during TPD analysis of pre-adsorbed CO_2 showed that most of bicarbonate and carbonate species desorbed between 100-300 °C (Figure 4.5b).[28] On the other hand, all species desorbed before 250 °C over In-TiO_2 catalyst (Figure 4.5a, b) suggesting that adsorbed CO_2 was not stable at reaction temperature. In addition, the amount of CO_2 adsorbed on In-TiO_2 was lower even though the CO_2 conversion was much higher over In-TiO_2 as compared to In-ZrO_2. This indicates that, for CO_2 conversion over the surface of In-TiO_2, CO_2 adsorption ability was not a vital factor.

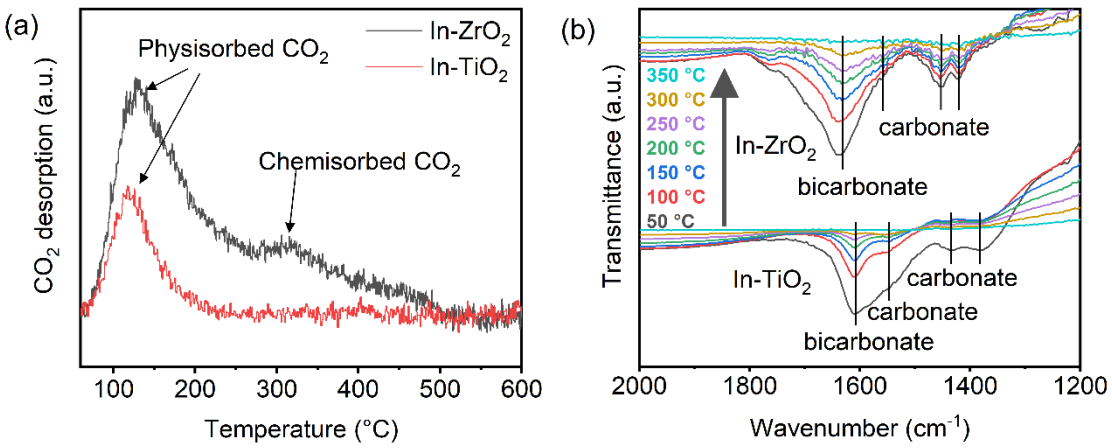

Figure 4.5: (a) Evolution of CO_2 (m/z = 44) during CO_2 TPD experiment. (b) DRIFTS analysis during temperature program desorption after in situ CO_2 adsorption over the surface of In-ZrO_2 and In-TiO_2.

4.3.4 Mechanistic details

The evolution of reaction intermediates was observed by monitoring the DRIFTS spectra under reaction condition at different time intervals over In-ZrO_2 catalyst (Figure 4.6a). Peaks at 2972, 2882, 2740, 1585, 1384 cm^{-1} were assigned to bidentate formate species.[29–31] Bicarbonate and carbonate species were also detected under the reaction condition.[31,32,33] Peaks at 2822, 2928 and 1144 cm^{-1} were assigned to methoxy species.[34,35] Formate was the dominant species on the surface and the peak intensity for both the formate and methoxy increased with time (Figure 4.6a). A comparison of formate and methoxy peak intensities showed that methoxy formation closely followed the evolution of formate (Figure 4.6b). It suggests that formate is the intermediate for methanol formation. When comparing the in-situ DRIFT spectra for In-ZrO_2 and pure ZrO_2, the formate peak position shifted towards higher wavenumber over In-ZrO_2 (Figure 4.7). This was interpreted as stabilization of formate species over the interface of In-V_o-Zr (V_o = oxygen vacancy), establishing its presence at the active site.[18]

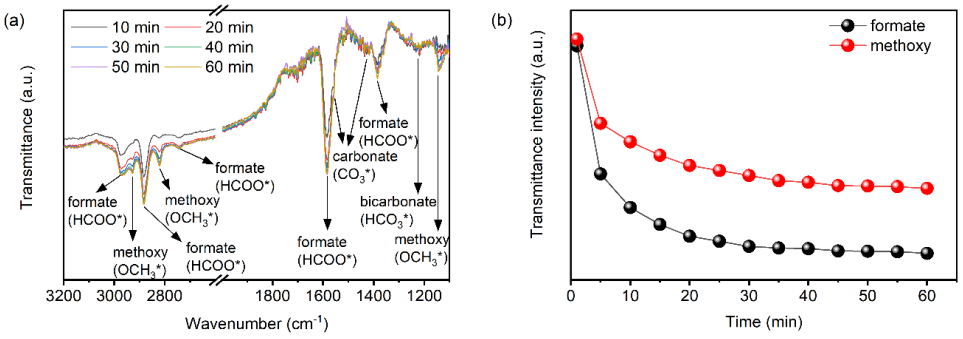

Figure 4.6: (a) In situ DRIFTS analysis at different times and (b) formation pattern of formate and methoxy over In-ZrO_2 catalyst. Reaction condition: 300 °C, 0.1 MPa and 25,000 mL h^{-1} g_{cat}^{-1} SV, H_2:CO_2 = 4:1.

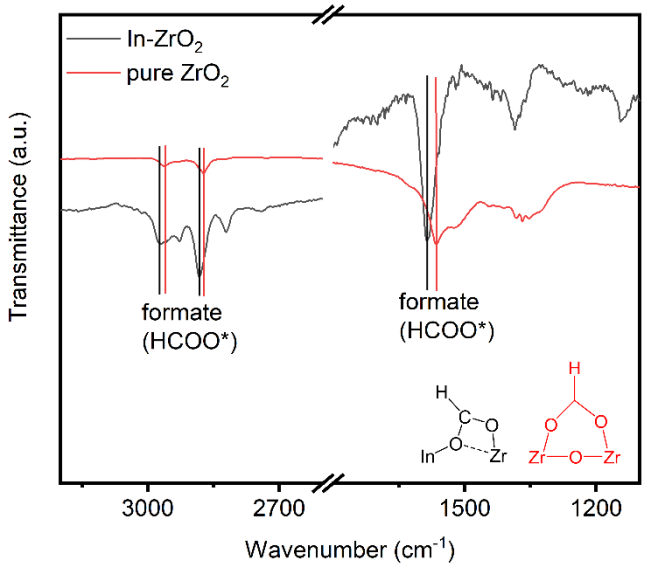

Figure 4.7: Comparison of *in situ* DRIFTS spectra of In-ZrO_2 and pure ZrO_2. Reaction condition: 300 °C, 0.1 MPa, H_2:CO_2 = 4:1. For pure ZrO_2 temperature was 340 °C to increase the formate intensity.

To understand the role of interfacial site in stabilization of formate, formic acid TPD was carried out on ZrO_2 and fresh In-ZrO_2 catalyst. Figure 4.8a shows the evolution of CO_2 and CO gas during formic acid decomposition. Pure ZrO_2 only produced CO. This indicates that Zr-O-Zr site is only active for formate decomposition to CO (Figure 4.8b). During formic acid decomposition over the In-ZrO_2 surface, the temperature range for CO evolution was similar to that of pure ZrO_2. This indicates that CO was mainly produced over Zr-O-Zr site on the surface of In-ZrO_2 (Figure 4.8b). CO_2 was only produced by In-ZrO_2 catalyst (Figure 4.8a), indicating the formate stabilization over In-O-Zr sites (Figure 4.8b). This experiment suggests that the formate stabilized over the interfacial site of In and Zr cannot be decomposed to CO and as a result, chance of further hydrogenation to form methanol increased under H_2 rich atmosphere.

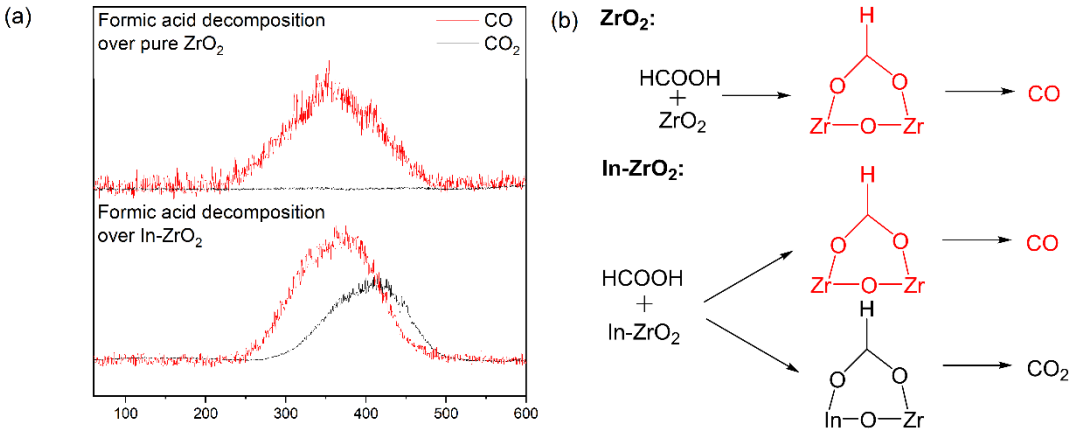

Figure 4.8: (a) Evolution of CO and CO_2 during formic acid decomposition over ZrO_2 and In-ZrO_2. (b) Schematic representation of formate decomposition over the surface of ZrO_2 and In-ZrO_2.

In-situ DRIFTS analysis of In-TiO_2 showed no identifiable intermediate species and only peaks for gaseous CO were observed at 2172 and 2109 cm^{-1} (Figure 4.9).[36] The formation of CO without the presence of any intermediate indicated that CO might be produced via redox mechanism where H_2 reduced the active site and CO_2 oxidized it back producing CO.

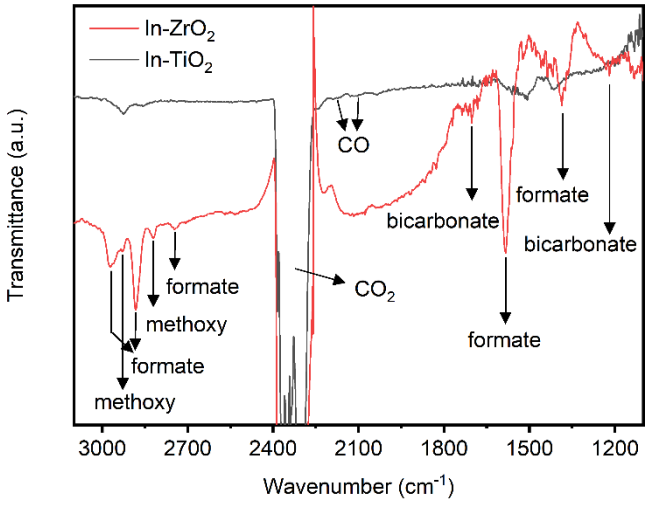

Figure 4.9: In situ DRIFTS spectra over In-TiO_2 (black line) compared with In-ZrO_2 (red line).

The following experiment was carried out to confirm the mechanism of CO formation over In-TiO_2. First, the catalyst was reduced at 300 °C for 30 min under H_2

atmosphere to generate oxygen vacant sites followed by Ar purge for 15 min to remove the residual H_2 gas. Then mixture of Ar and CO_2 was flown and the evolution of CO was recorded using a GC (Figure 4.10a). CO evolution peaked in first 5 min and then decreased slowly showing that CO_2 conversion continues for long time even in the absence of H_2 gas. To further confirm the redox mechanism, the oxidation state of Ti in In-TiO_2 was analyzed using ultraviolet-visible (UV-VIS) spectroscopy after each reaction step in the redox cycle (Figure 4.10b). Fresh catalyst showed one peak at 340 nm corresponding to the electronic transition from valence band to conductance band in TiO_2 (Figure 4.10b, black line).[37] After H_2 treatment, a shoulder peak appeared in the range of 400-700 nm indicating the formation of Ti^{3+} (Figure 4.10b, red line).[37,38] After treating this reduced catalyst under CO_2, the intensity of the shoulder peak reduced (Figure 4.10b, blue line) due to reoxidation of Ti^{3+} to Ti^{4+}. H_2 treatment of this oxidized sample again created Ti^{3+} species and the shoulder peak regained its shape (Figure 4.10b, green line). This experiment proves that Ti changes its oxidation state at each step of the oxidation and reduction which is consistent with the redox mechanism.

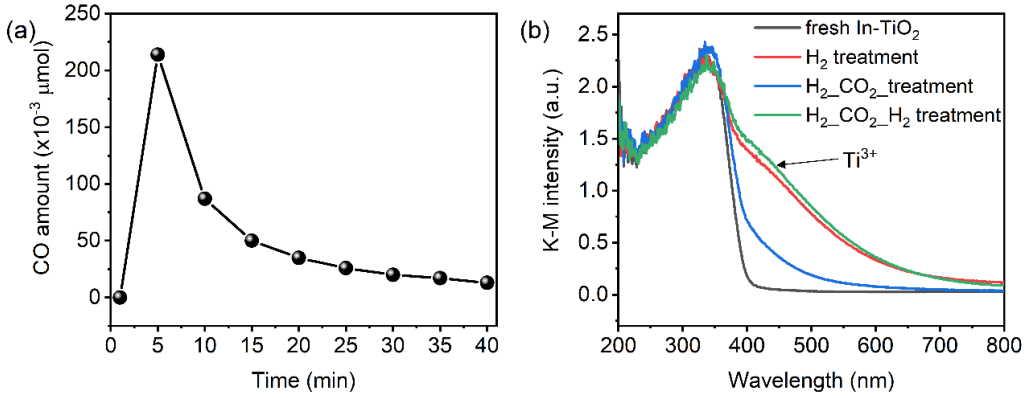

Figure 4.10: (a) Evolution of CO over In-TiO_2 during CO_2 flow after H_2 and Ar flow respectively. (b) UV-VIS analysis of In-TiO_2 after treatment under different atmosphere.

4.3.5 Discussion

Figure 4.11 shows the mechanism for CO_2 hydrogenation over the surface of two In doped catalysts. For In-TiO_2 catalyst, both In and Ti are easily reducible in their oxide form resulting in a partially reduced surface with oxygen vacancies. These In-V_o-Ti sites would exhibit reduced indium and titanium species (see XPS analysis, Figure 4.4). It has been previously reported that In catalysts with highly reduced surface are not active for CO_2 hydrogenation to methanol.[14] Song et al. showed that hexagonal In_2O_3 can undergo complete reduction to In^0, which then reoxidized to cubic In_2O_3 by CO_2. However, the reduction and oxidation of In_2O_3 changes is structure and the initial state of In_2O_3 cannot be recovered.[39] In contrast, the In-V_o-Ti interface, while being highly reduced, can carry out the reduction/oxidation cycle without changing the initial structure. This redox mechanism becomes feasible because of the presence of Ti^{3+} which is stable even under reducing condition and is easily oxidized by CO_2.[37,40]

On the other hand, for In-ZrO_2 catalyst, due to strong interaction of indium species with non-reducible ZrO_2, the reducibility of indium species was low. At the In-V_o-Zr interface site, strong CO_2 adsorption occurs. Hydrogen is dissociated over indium sites and transfer of hydrogen from indium to C of CO_2 would produce formate species (Figure 4.11b). Majority of formate would form methanol via successive hydrogenation. Therefore, the nature of active site at the interface is controlled by the reducible nature of the support.

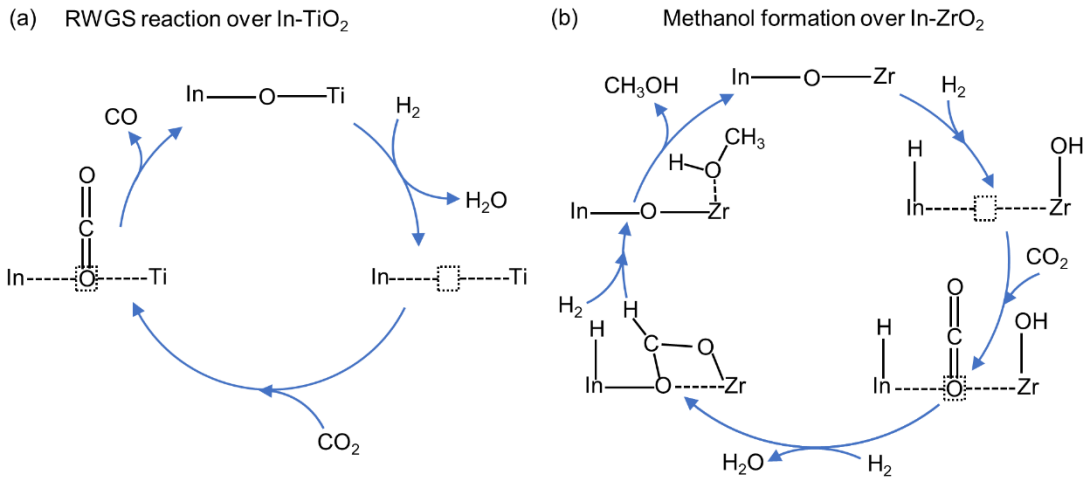

Figure 4.11: (a) Mechanism of CO formation over In-TiO_2 and (b) mechanism of methanol formation over In-ZrO_2.

4.3.6 Significance of interface in impregnated catalysts

Although interfacial sites are the only catalytically active site in doped catalyst their role in impregnated catalyst is not always clear. The parent In_2O_3 shows different product selectivity in comparison to interface of In with support, especially in the case of In-TiO_2. Therefore, the influence of interface in impregnated In_2O_3/TiO_2 and In_2O_3/ZrO_2 catalyst for CO_2 hydrogenation was investigated. The impregnated In_2O_3/TiO_2 exhibited CO selectivity of 95% as opposed to 100% CO selectivity for doped catalyst (Figure 4.12). Methanol selectivity was 5%, which originated from reaction over In_2O_3 particles. The impregnated In_2O_3/ZrO_2 catalysts showed a methanol selectivity (65%), which was in between the selectivity obtained over doped In-ZrO_2 and pure In_2O_3 catalysts. By comparing, the selectivity of products over impregnated catalysts with that over sol-gel doped catalysts, it is clear that even for the impregnated catalysts, the interfacial In-V_o-M (M = Ti/Zr) site showed similar activity as for sol-gel doped catalysts and for In catalyst the interface with oxide support is the dominant active site.

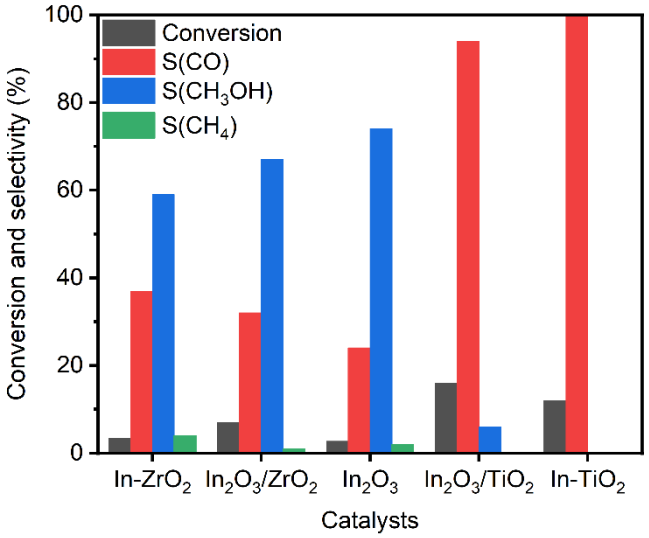

Figure 4.12: Comparison of product selectivity of impregnated catalysts with sol-gel and pure In_2O_3.

4.4 Conclusion

This chapter shows how the support metal atom can tune the activity, selectivity and CO_2 hydrogenation pathway in indium doped oxides. The reducibility of the support controls the CO_2 hydrogenation pathway at the interfacial site with doped indium metal. When indium was doped in ZrO_2, The non-reducible nature of ZrO_2 did not cause excessive reduction of indium species and retained the CO_2 hydrogenation ability. As a result, formate species were formed and further hydrogenation led to methanol formation. On the other hand, TiO_2 being highly reducible caused reduction of indium species and the highly reduced indium could not adsorb CO_2 at In-V_o-Ti site. Instead, both In and Ti at the interfacial site were re-oxidized by CO_2 to produce CO with high selectivity. Therefore, in doped oxide catalysts, while CO_2 hydrogenation ability is generated due to the dopants, the role of the support metal atom at the interfacial site with the dopant becomes important. As found in chapter 2 and 3, this chapter confirms that, presence of support metal atom at M-O-S (M = dopant, S = support metal atom) like active site controls the CO_2 hydrogenation pathway and thus, controls the CO_2 hydrogenation selectivity.

References

1. S. Kattel, P. Liu and J. G. Chen, *J. Am. Chem. Soc*, 2017, **139**, 9739–9754.
2. Y. X. Pan, C. J. Liu, D. Mei and Q. Ge, *Langmuir*, 2010, **26**, 5551–5558.
3. S. Huygh, A. Bogaerts and E. C. Neyts, *J. Phys. Chem. C*, 2016, **120**, 21659–21669.
4. J. Ye, C. Liu, D. Mei and Q. Ge, *ACS Catal.*, 2013, **3**, 1296–1306.
5. S. Kattel, B. Yan, J. G. Chen and P. Liu, *J. Catal.*, 2016, **343**, 115–126.
6. S. Li, Y. Xu, Y. Chen, W. Li, L. Lin, M. Li, Y. Deng, X. Wang, B. Ge, C. Yang, S. Yao, J. Xie, Y. Li, X. Liu and D. Ma, *Angew. Chemie Int. Ed.*, 2017, **56**, 10761–10765.
7. X. Li, J. Lin, L. Li, Y. Huang, X. Pan, S. E. Collins, Y. Ren, Y. Su, L. Kang, X. Liu, Y. Zhou, H. Wang, A. Wang, B. Qiao, X. Wang and T. Zhang, *Angew. Chemie Int. Ed.*, 2020, **59**, 19983–19989.
8. Y. Zhang, Z. Zhang, X. Yang, R. Wang, H. Duan, Z. Shen, L. Li, Y. Su, R. Yang, Y. Zhang, X. Su, Y. Huang and T. Zhang, *Green Chem.*, 2020, **22**, 6855–6861.
9. S. Kattel, W. Yu, X. Yang, B. Yan, Y. Huang, W. Wan, P. Liu and J. G. Chen, *Angew. Chemie Int. Ed.*, 2016, **55**, 7968–7973.
10. S. Kattel, P. J. Ramírez, J. G. Chen, J. A. Rodriguez and P. Liu, *Science*, 2017, **355**, 1296–1299.
11. M. Behrens, F. Studt, I. Kasatkin, S. Kühl, M. Hävecker, F. Abild-Pedersen, S. Zander, F. Girgsdies, P. Kurr, B. L. Kniep, M. Tovar, R. W. Fischer, J. K. Nørskov and R. Schlögl, *Science*, 2012, **336**, 893–897.
12. J. Graciani, K. Mudiyanselage, F. Xu, A. E. Baber, J. Evans, S. D. Senanayake, D. J. Stacchiola, P. Liu, J. Hrbek, J. Fernández Sanz and J. A. Rodriguez, *Science*, 2014, **345**, 546–550.
13. S. Kattel, B. Yan, Y. Yang, J. G. Chen and P. Liu, *J. Am. Chem. Soc.*, 2016, **138**, 12440–12450.
14. O. Martin, A. J. Martín, C. Mondelli, S. Mitchell, T. F. Segawa, R. Hauert, C. Drouilly, D. Curulla-Ferré and J. Pérez-Ramírez, *Angew. Chemie Int. Ed.*, 2016, **55**, 6261–6265.
15. M. S. Frei, C. Mondelli, A. Cesarini, F. Krumeich, R. Hauert, J. A. Stewart, D. Curulla Ferré and J. Pérez-Ramírez, *ACS Catal.*, 2020, **10**, 1133–1145.
16. C. Yang, C. Pei, R. Luo, S. Liu, Y. Wang, Z. Wang, Z. J. Zhao and J. Gong, *J. Am. Chem. Soc.*, 2020, **142**, 19523–19531.
17. A. Tsoukalou, P. M. Abdala, A. Armutlulu, E. Willinger, A. Fedorov and C. R. Müller, *ACS Catal.*, 2020, **10**, 10060–10067.
18. T. Y. Chen, C. Cao, T. B. Chen, X. Ding, H. Huang, L. Shen, X. Cao, M. Zhu, J. Xu, J. Gao and Y. F. Han, *ACS Catal.*, 2019, **9**, 8785–8797.
19. S. Brunauer, P. H. Emmett and E. Teller, *J. Am. Chem. Soc*, 1938, **60**, 309–319.

20. J. Wang, G. Li, Z. Li, C. Tang, Z. Feng, H. An, H. Liu, T. Liu and C. Li, *Sci. Adv.*, 2017, **3**, e1701290.
21. J. Wang, C. Tang, G. Li, Z. Han, Z. Li, H. Liu, F. Cheng and C. Li, *ACS Catal.*, 2019, **9**, 10253–10259.
22. R. D. Shannon, *ActaCrystal. A*, 1976, **32**, 751–767.
23. V. Bratan, C. Munteanu, C. Hornoiu, A. Vasile, F. Papa, R. State, S. Preda, D. Culita and N. I. Ionescu, *Appl. Catal. B Environ.*, 2017, **207**, 166–173.
24. H. Zhu, Z. Qin, W. Shan, W. Shen and J. Wang, *J. Catal.*, 2004, **225**, 267–277.
25. M. M. Li, H. Zou, J. Zheng, T. Wu, T. Chan, Y. Soo, X. Wu, X. Gong, T. Chen, K. Roy, G. Held and S. C. E. Tsang, *Angew. Chemie Int. Ed.*, 2020, **132**, 16173–16180.
26. G. Liu, H. G. Yang, X. Wang, L. Cheng, H. Lu, L. Wang, G. Q. Lu and H. M. Cheng, *J. Phys. Chem. C*, 2009, **113**, 21784–21788.
27. X. Chen, L. Liu, P. Y. Yu and S. S. Mao, *Science*, 2011, **331**, 746–750.
28. K. Pokrovski, K. T. Jung and A. T. Bell, *Langmuir*, 2001, **17**, 4297–4303.
29. C. Schild, A. Wokaun and A. Baiker, *J. Mol. Catal.*, 1990, **63**, 243–254.
30. I. A. Fisher and A. T. Bell, *J. Catal.*, 1997, **172**, 222–237.
31. K. Pokrovski, K. T. Jung and A. T. Bell, *Langmuir*, 2001, **17**, 4297–4303.
32. E. M. Köck, M. Kogler, T. Bielz, B. Klötzer and S. Penner, *J. Phys. Chem. C*, 2013, **117**, 17666–17673.
33. K. D. Dobson and A. J. McQuillan, *Langmuir*, 1997, **13**, 3392–3396.
34. S. Kattel, B. Yan, Y. Yang, J. G. Chen and P. Liu, *J. Am. Chem. Soc*, 2016, **138**, 12440–12450.
35. C. Wu, L. Lin, J. Liu, J. Zhang, F. Zhang, T. Zhou, N. Rui, S. Yao, Y. Deng, F. Yang, W. Xu, J. Luo, Y. Zhao, B. Yan, X. D. Wen, J. A. Rodriguez and D. Ma, *Nat. Commun.*, 2020, **11**, 1–10.
36. D. Song, J. Li and Q. Cai, *J. Phys. Chem. C*, 2007, **111**, 18970–18979.
37. L. F. Bobadilla, J. L. Santos, S. Ivanova, J. A. Odriozola and A. Urakawa, *ACS Catal.*, 2018, **8**, 7455–7467.
38. H. Liu, H. T. Ma, X. Z. Li, W. Z. Li, M. Wu and X. H. Bao, *Chemosphere*, 2003, **50**, 39–46.
39. A. Tsoukalou, P. M. Abdala, D. Stoian, X. Huang, M. G. Willinger, A. Fedorov and C. R. Müller, *J. Am. Chem. Soc*, 2019, **141**, 13497–13505.
40. S. S. Kim, H. H. Lee and S. C. Hong, *Appl. Catal. A Gen.*, 2012, **423**–**424**, 100–107.

Chapter 5

Conclusion

Use of fossil fuels has dramatically increased the amount of CO_2, a major greenhouse gas, in the atmosphere. The accumulation of CO_2 has already started to show its adverse effect on the nature. Therefore, it is high time to take necessary action to reduce the CO_2 emission in the atmosphere. One effective way is to convert CO_2 to useful fuels and chemicals. In this way, CO_2 can be treated as important C1 feedstock instead of waste and production of fuels and chemicals from CO_2 will also reduce the consumption of fossil fuels. In this regard, production of methanol and CO from CO_2 is important because they are precursors for synthesis of many industrially important bulk chemicals and hydrocarbon fuels. The major challenge in CO_2 hydrogenation to methanol or CO is to achieve high selectivity of a single product. Therefore, the objective of this thesis is to develop highly active and selective catalytic systems for methanol and CO formation along with the study of parameters that control product selectivity. Over conventional support metal catalyst, it has been found that metal oxide can help to activate CO_2 while metal nanoparticles are used for H_2 dissociation. However, this system tends to further hydrogenate methanol and CO. This study is focused on metal oxide catalysts having atomically dispersed metal dopants for CO_2 hydrogenation. Atomic dispersion of metal dopants will have enhanced interaction with support metal oxide, which is expected to increase the stability and create specific active site to carry out selective catalytic hydrogenation of CO_2.

In **Chapter 2**, CO_2 hydrogenation to methanol was studied using doped In_2O_3 catalysts. In_2O_3 was reported to be a selective catalyst for this reaction. However, the methanol productivity was low due to poor CO_2 conversion over pure In_2O_3. In this chapter, transition metal doped In_2O_3 catalysts were synthesized. Among several transition metal used, atomically dispersed Rh dopants in In_2O_3 showed the highest promotional effect. A methanol productivity of 1.0 g_{MeOH} h^{-1} g_{cat}^{-1}, one of the highest till date, was achieved without reduction in methanol selectivity. Characterization suggested that atomically dispersed Rh atoms created oxygen vacancy around itself under hydrogenation condition and as a result, neighboring In atoms became partially reduced. The resulting Rh-V_o-In (V_o = oxygen vacancy) promoted CO_2 adsorption and formation of formate, which is the intermediate for methanol formation. Further H_2 dissociation over Rh atoms led to the hydrogenation of formate species and produced methanol. This chapter showed that metal atoms doped in metal oxides could improve CO_2 hydrogenation activity.

In **Chapter 3**, the concept of atomically dispersed metal atoms with oxygen vacancy was applied in RWGS reaction and high CO selectivity was achieved. Co doped ZrO_2 catalysts were prepared and CO selectivity over 95% was achieved. Oxygen vacancies were generated near CO atoms due to the charge imbalance between Co^{2+} and Zr^{4+}. These oxygen vacancies promoted strong CO_2 chemisorption as carbonate species. Co atoms helped in H_2 dissociation and formate species formed at the interfacial site between Co and Zr (Co-O-Zr). The formate species decomposed selectively to CO instead of producing methanol via further hydrogenation of formate. Methane production via CO hydrogenation was suppressed because of the easy desorption of CO from the active site. As a result, a high CO selectivity was achieved.

Along with the isolation of the metal sites, the role of support oxide or the host oxide should be important. **Chapter 2** and **Chapter 3** showed that the interfacial site between doped metal atom and the metal atom of the support was the active site. Therefore, to understand the role of support at the interfacial site, indium doped catalysts with different supports were synthesized and analyzed for CO_2 hydrogenation in **Chapter 4**. Indium doped TiO_2 and ZrO_2 (In-TiO_2 and In-ZrO_2) were prepared. TiO_2 and ZrO_2 were used in this study because they are widely used in CO_2 hydrogenation and are distinct in their reducible property. In-TiO_2 produced CO and In-ZrO_2 produced methanol as the major product. It was found that the reducibility of the support is the key factor in controlling CO_2 hydrogenation mechanism and selectivity. Because TiO_2 is easily reducible, indium atoms neighboring to Ti atoms were highly reduced. The resulting In-V_o-Ti site could not carry out CO_2 hydrogenation to methanol. Instead, the active site was oxidized back by CO_2 producing CO selectively. On the other hand, in case of In-ZrO_2, indium species were not reduced due to strong interaction with non-reducible ZrO_2. As a result, formate was formed over the interfacial site, which further hydrogenated to methanol.

This work explores the synthesis of oxide-based catalysts having atomically dispersed metal dopants for selective synthesis of methanol and CO via CO_2 hydrogenation and focuses on the nature of support material that can control CO_2 hydrogenation selectivity. The future work in this field should focus on the development of inexpensive and selective materials applicable for industrial purpose. In methanol formation reaction, current industry uses Cu-ZnO/Al_2O_3 catalyst, which has demerits regarding activity and stability. Although transition metals, especially noble metals can promote the activity of In_2O_3, indium itself is expensive and promotion with noble metals makes the catalyst even more expensive. Hence, synthesis of

inexpensive and selective methanol synthesis catalyst needs to be focused. For RWGS reaction, the main focus should be achieving high CO selectivity under milder reaction condition with high CO_2 conversion. If that is achieved, then the products derivable from CO can also be derived directly from CO_2 by combining RWGS reaction and downstream reactions from CO. In addition, mechanistic study should be focused to understand the parameters helping in the reaction and to develop new catalysts based on the mechanism.

Synopsis

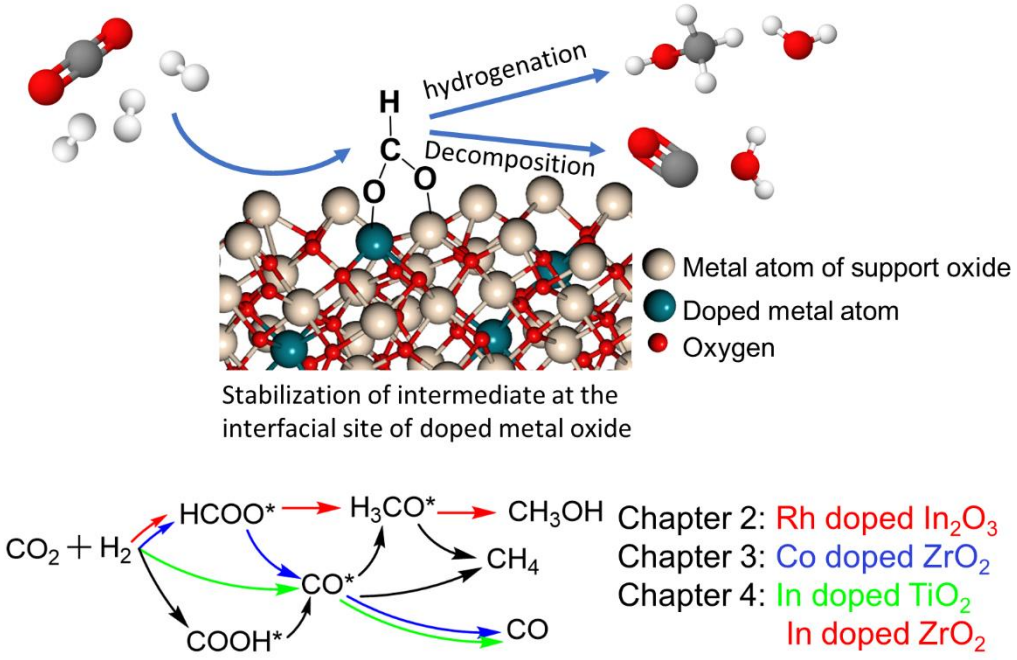

List of Publications

Journal publications

Nazmul Hasan MD Dostagir, Coogan Thompson, Hirokazu Kobayashi, Ayman M. Karim, Atsushi Fukuoka and Abhijit Shrotri, Rh promoted In_2O_3 as a highly active catalyst for CO_2 hydrogenation to methanol. *Catalysis Science & Technology*, **2020**, 10, 8196-8202.

Nazmul Hasan MD Dostagir, Rattanawalee Rattanawan, Min Gao, Jun-ya Hasegawa, Kiyotaka Asakura, Atsushi Fukuoka and Abhijit Shrotri, Co single atoms in ZrO_2 with inherent oxygen vacancies for selective hydrogenation of CO_2 to CO. *ACS Catalysis*, **2021**, 11 (15), 9450-9461.

Nazmul Hasan MD Dostagir, Atsushi Fukuoka and Abhijit Shrotri, Role of support in controlling CO_2 hydrogenation pathway. (In preparation)

Journal publications (not related to this thesis)

Lingcong Li, Nazmul Hasan MD Dostagir, Abhijit Shrotri, Atsushi Fukuoka and Hirokazu Kobayashi, Partial oxidation of methane to syngas via formate intermediate found for a ruthenium-rhenium bimetallic catalyst, *ACS catalysis*, **2021**, 11 (7), 3782-3789.

Nazmul Hasan MD Dostagir, Mahendra Kumar Awasthi, Ankit Kumar, Kavita Gupta, Silke Behrens, Abhijit Shrotri and Sanjay Kumar Singh, Selective catalysis for room-temperature hydrogenation of biomass-derived compounds over supported NiPd catalysts in water. *ACS Sustainable Chemistry & Engineering*, **2019**, 7 (10), 9352-9359.

Conference contributions

Nazmul Hasan MD Dostagir, Coogan Thompson, Hirokazu Kobayashi, Ayman M. Karim, Atsushi Fukuoka and Abhijit Shrotri, Promotion of In_2O_3 with Rh for superior methanol yield during CO_2 hydrogenation. *ACS Spring 2021*, Online, April 6, **2021** (Oral)

Nazmul Hasan MD Dostagir, Abhijit Shrotri and Atsushi Fukuoka, CO_2 hydrogenation to methanol over highly active Rh-In_2O_3 catalysts. *The 126th annual meeting of Catalysis Society of Japan*, Online, September 17, **2020** (Oral)

Nazmul Hasan MD Dostagir, Coogan Thompson, Hirokazu Kobayashi, Ayman M. Karim, Atsushi Fukuoka and Abhijit Shrotri, Doping of Rh in In_2O_3 promotes methanol formation during CO_2 hydrogenation. *IRCCS the 4th Joint International Symposium*, Online, March 15, **2021** (Poster)

Nazmul Hasan MD Dostagir, Abhijit Shrotri and Atsushi Fukuoka, Single atom Rh promoted In_2O_3 for CO_2 hydrogenation to methanol. *IRCCS the 3rd Joint International Symposium*, Nagoya, Japan, January 31, **2020** (Poster)

Acknowledgement

The journey of my PhD (2018-2021) is coming to an end. On this occasion, I would like to express my immense sense of gratitude to those who helped me during this period not only in academics but also helped me to evolve myself as a human being.

First of all, I would like to thank my supervisor, Professor Atsushi Fukuoka, for providing me the opportunity to carry out my research in his team. Your vast knowledge and experience helped me throughout my PhD work. Your ideas helped me to gather knowledge about catalysis. I appreciate that you took time out of your busy schedule to check my papers, presentations and thesis. Furthermore, I thank you for encouraging me on the day of my PhD defense. I am thankful to you for allowing me to attend conferences and symposiums, which provided me the platform to meet the bigger community of science. The environment of this lab that you created and maintained brought me joy during my work. Your thought – "Students should come up with their own ideas" really encouraged me to dive in the ocean of science. Thank you very much.

I would like to thank Dr. Kiyotaka Nakajima, my sub-supervisor. Your valuable comments and suggestions always helped me. I appreciate that you always cared about my research progress and gave me important suggestions. Moreover, I am thankful to you for checking my thesis and giving me valuable comments during my preparation of defense. Your eagerness to know the science behind reactions inspired me to carry out in depth study.

I am highly grateful to my daily supervisor, Dr. Abhijit Shrotri. You were there by my side and encouraging me in every moments. My PhD journey would not have been smooth without your help. Since the very beginning, you helped me a lot not only in research but also in the life outside the lab. You introduced me to the lab and helped me to learn instruments, to set up my reaction system and to design my research

projects. You gave me a lot of freedom in my research, which helped me to think independently. Thank you for listening to me with great patience during those endless discussions. Your positive attitude taught me to be optimistic even in hard times. Thank you for spending your time for correcting my papers, thesis, presentations. I sincerely appreciate your effort for those moments when you worked beyond office hours for me. I really enjoy working with you.

I would like to thank Dr. Hirokazu Kobayashi. Every discussion with you helped me to learn new things. Your suggestions in group meetings always helped me to understand the science in detail. Your comments and questions during my practice for PhD defense helped to a lot. I appreciate all your effort and encouragement that helped me to finish my PhD and inspires me to carry out finding new things in research.

I would also like to thank the committee members, Prof. Kei Murakoshi, Prof. Shin Mukai and Prof. Jun-ya Hasegawa for reviewing my work and attending my defense. I am grateful to AGS office for providing me the financial support for studying in Japan.

Special thanks to former and present members of my laboratory. They always extended their helping hands whenever I needed. Because of them, I never felt that I am in foreign and away from my home. To start with, our laboratory secretary, Hiromi Matsushima san, thank you very much for helping me with all the procedures and documents in Japanese. Dr. Jun Hirayama and Dr. Takuya Sagawa, thank you very much for being friendly. Your dedication towards research always inspired me. Special thanks to Dr. Shazia Sharmin Satter (aapa) who was like my elder sister. Communicating with you in Bengali language gave me the pleasure of using my mother tongue in foreign. A big thanks to Dr. Pengru Chen who always helped me in every aspect like a true senior. Understanding the documents and procedures became easy

because of you. Dr. Eunhyeok Yang, Dr. Kota Techikawara, Dr. Etty, Dr. Daniele, Dr. Li and Dr. Jan, spending time with you were memorable.

Special thanks to Yayati. Occasional parties in your room and those delicious dishes that you made were awesome. I also learned many things from you. I can recall the moments of having dinner with you and Dr Jan at every Friday night. Chen Yang, you helped me a lot since the moment you received me at the airport. Thank you very much for your help. I would also like to say thanks to Tat, Kato, Endo, Suzuki, Osanai, Fukuma san, Yakuwa, Shibayama san and Asakawa san. You always have been very friendly and helped me with Japanese language whenever needed. I wish you success in your career.

Lastly, I would like to acknowledge my family and friends in India. Without their continuous support, it was not possible for me to come along this much. I express my gratitude to all my teachers during my school days, bachelors' and masters' degree. I specially thank Dr. Sanjay Kumar Singh, my MS supervisor. Your continuous support and encouragement always helped me. I finish this by dedicating this thesis to my parents, SK Golam Morselim and SK Rehana Begum, who are much happier than me on my achievements.